

DISS. ETH NO. 28253

A Novel Stretchable Sensor System to Wirelessly Measure Musculoskeletal Soft Tissue Strains

A thesis submitted to attain the degree of
DOCTOR OF SCIENCES of ETH ZURICH

(Dr. sc. ETH Zurich)

presented by

Qiang Zhang

MSc. Sports Science, Shanghai University of Sports, China

born on 01.07.1988

citizen of

People's Republic of China

accepted on the recommendation of

Prof. Dr. William R. Taylor, examiner

Dr. Colin R. Smith, co-examiner

Prof. Dr. Jaehong Lee, co-examiner

2022

Statement of originality

I hereby confirm that I am the sole author of this PhD thesis enclosed and that I have compiled it in my own words. Corrections of form and contents were performed with support of my supervisors.

Qiang Zhang

Acknowledgements

As a Chinese student, I believe my PhD study in ETH Zürich is not only a journey from a far-east country of ancient civilization to a modern western democratic country, but also a great event that has significantly changed my life. There are so many people, who provided me enormous support and help, that I sincerely appreciate.

My primary gratitude should be definitely expressed to my PhD supervisor, Prof. William R. Taylor, who spared no effort to supervise my PhD project and help me in funding application. I learned so, so, so much from him, from correct English pronunciations to optimal scientific writing, from time regulation to critical academic thinking. I admire him, not only because of his exceptional knowledge and abilities, more importantly, because he cares about the students, which makes him so much different from many others.

I couldn't make my PhD project without the support of the sensor project team, specifically Dr. Colin R. Smith and Naomi Adam. The many interesting chats with Colin provided me invaluable ideas on my research and career development. Naomi and I worked extremely closely together to conduct the core validation testing on the sensor. Without her support, much of this work would not have been possible. Naomi, you are an extremely entertaining person with many interesting opinions, and I am deeply grateful for your continued support throughout this journey. Colin and Naomi, many thanks to both of you. Finally, I also acknowledge the insightful comments and suggestions on my thesis provided by Prof. Jaehong Lee.

I sincerely appreciate Prof. Dr. Janos Vörös for allowing me to use the experimental facilities in his lab. The original technologies of the sensor are from his group. He allowed us to access to the technologies without conditions. Specially thanks to Dr. Flurin Stauffer, he taught me a great deal about stretchable electronics. In addition, Dr. Byron Llerena's efforts on material preparations was important to the sensor fabrications, and thus is appreciated. Finally, it has been an exceptionally rewarding experience to work with Prof. Dr. Walter Herzog's group on the in-vivo sensor measurement. Special thanks must go to Dr. Fransiska Bossuyt for sharing the in-vivo measurement data, which greatly increased the quality of my publications. Finally, thanks to the several students I have supervised or worked with, Sarah Abramovic, Vullnet Useini, Christian Huber, and Polina Rusina, for their help during their master theses or internships.

I'm honestly grateful to my colleagues in the Laboratory for Movement Biomechanics. Here, special thanks go to my friends, Longfeng Rao, Dr. Hosseini Nasab Seyyed Hamed, Dr. Deepak Kumar, and Dr. Navrag Singh, who created a friendly and fun atmosphere throughout the past 5 years. Partying with them was a valuable source of support to me in Zürich.

I acknowledge that my PhD project was financially supported by the Chinese Scholarship Council, the Robert Mathys Foundation, and the Swiss National Science Foundation. Many thanks for their support – it is important to realise that without their financial support, projects like this would not be possible.

Finally, I would like to thank my family for their love, patience, and support. To my parents, thank you for not only giving me the life I have led, but also standing firmly behind me during the past 33 years. To my wife, Zhenzhen, I owe you so much, for your kind love and understanding during the lonely years. I would never have been able to achieve this PhD without you. Thank you.

Abstract

Musculoskeletal soft tissues (MSTs) play important roles in generating movement, absorbing external impacts, and stabilizing joints, and thus have a high incidence of injury. A comprehensive understanding of the functional demands of MSTs is critical to the successful treatment of soft tissue injuries. The quantification of *in-vivo* MST strains is therefore critical for both facilitating scientific discoveries on tissue function such as revealing the complex interactions within muscle-tendonous units, but also driving innovative clinical treatments and supporting the optimization of rehabilitation protocols. The critical need for *in-vivo* quantification of MST strains has historically inspired the development of different measurement techniques, including implantable strain sensors and ultrasound. Until now, implantable strain sensors have relied on rigid structures and wired transmission of sensor signals. As a result, these measurements have mostly been performed during controlled movements and in sterile surgical environments. Similarly, ultrasound measurements remain limited by out-of-plane artefact, and result in unknown measurement errors. A novel strain sensor technology that can mitigate these limitations and enable wireless MST strain measurements during dynamic activities is thus imperative.

The aims of this PhD thesis were to develop and provide a proof-of-concept wireless, biocompatible, stretchable strain sensor system for the *in-vivo* measurement of MST strain. These aims were achieved by firstly reviewing all techniques that have been applied for *in-vivo* MST strain measurement, and subsequently performing a series of investigations to optimize and fabricate a novel stretchable strain sensor technology and wireless readout system. Finally, the validation of the stretchable strain sensor system was performed through testing its wireless sensing performance and implanting it into a sheep model to measure the tendon strains during dynamic movement *in vivo*.

The narrative review of the literature provided a clear overview of different measurement techniques to date, including their key findings, clinical implications, and limitations. In addition to understanding critical limitations of existing sensor techniques, a review of the literature has revealed the magnitudes of MST strains that can be expected *in vivo*. As a result, a clear vision has been achieved regarding how current strain sensors should be revolutionized towards minimally disruptive, wireless data transmission, and long-term biocompatibility, in order to withstand the demands of known *in-vivo* MST strain measurements during dynamic activities.

With a clear view of the musculoskeletal measurement requirements, the experimental work of this thesis firstly developed the prototype of a stretchable capacitor consisting of gold-coated titanium dioxide nanowires embedded in soft silicone elastomers. The stretchable capacitor was bonded to a coil to form a chipless wireless strain sensor for inductive readout of its resonant frequency. Based on the sensor prototype, an advanced stretchable strain sensor was developed through optimizing the coil structure, PDMS casting, and sensor fixation. In addition, a custom-designed readout box was

collaboratively developed to measure the resonant frequency of the sensor at a high sampling rates (1 kHz). The sensor can be sutured onto the surface of the MST, allowing it to be stretched in line with musculoskeletal deformations, hence providing an indirect method to assess the MST strain patterns. A linear signal variation between 0 and 25% strain was demonstrated, and the strain sensor was electronically stable in a simulated *in-vivo* environment for one week and over 100'000 cycles of fatigue loading. Outstanding resolution (0.1% strain, $\approx 9 \mu\text{m}$) was found during wireless strain measurements. *Ex-vivo* tensile tendon testing demonstrated that the sensor provided accurate measurements of sheep plantaris tendon strains. Finally, the strain sensor was implanted on the medial gastrocnemius tendon of a sheep, and strain measurement was performed during sheep trotting. The experiments indicated that the sensor was able to record the repetitive strain patterns in the tendon of the sheep.

The findings of this PhD thesis revealed that the strain sensor could successfully measure tendon strains in the living body, indicating its applicability for addressing important biomechanical questions regarding MST functionality, injury, pathology, and rehabilitation mechanisms. Moreover, direct measurement of MST strains using this strain sensor system could be used to validate the results of modelling simulations and to optimize current musculoskeletal models. Further research is needed to improve the strain sensor for its *in-vivo* robustness and functional integrity in order to withstand long-term *in-vivo* implantation and measurement during dynamic movements. Finally, a bioabsorbable version of the strain sensor may be needed for clinical translation.

Zusammenfassung

Das Muskuloskeletale Weichgewebe (MW) spielt eine wichtige Rolle bei der Absorption äusserer Stösse und der Stabilisierung von Gelenken während dynamischen Körperbewegungen und weisen daher eine hohe Verletzungshäufigkeit auf. Ein umfassendes Verständnis der funktionellen Anforderungen von MW ist entscheidend für die erfolgreiche Behandlung von MW-Verletzungen. Die Quantifizierung der MW-Belastungen in-vivo ist daher von entscheidender Bedeutung, um sowohl wissenschaftliche Erkenntnisse über die Gewebefunktion zu gewinnen, wie z.B. die komplexen Interaktionen innerhalb von Muskel-Sehnen-Einheiten, als auch um innovative klinische Behandlungen voranzutreiben und die Optimierung von Rehabilitationsprotokollen zu unterstützen. Die Notwendigkeit einer In-vivo-Quantifizierung von MW hat die Entwicklung/Anwendung von drei Hauptmesstechniken inspiriert: 1) implantierbare Dehnungssensoren, 2) virtuelle Faserdehnung und 3) Ultraschall. Implantierbare Dehnungssensoren sind als direkter Messansatz weit verbreitet, um in-vivo-Dehnungen in MW wie dem vorderen Kreuzband und der Achillessehne zu messen. Aufgrund mehrerer Einschränkungen dieser Sensoren wurden diese Messungen jedoch hauptsächlich während kontrollierter Bewegungen und in sterilen chirurgischen Umgebungen durchgeführt. Eine neuartige Dehnungssensortechnologie, die diese Einschränkungen abschwächt und MW-Dehnungsmessungen bei dynamischen Bewegungen ermöglicht, ist daher dringend erforderlich.

Die Ziele dieser Doktorarbeit waren die Entwicklung und Validierung eines drahtlosen, biokompatiblen, dehnbaren Dehnungssensorsystems für In-vivo-MW-Belastungsmessungen. Diese Ziele wurden durch eine Überprüfung aller Techniken erreicht, die für In-vivo-MW-Dehnungsmessungen angewendet wurden, sowie durch eine Reihe von Untersuchungen zur Optimierung einer dehnbaren Elektroniktechnologie, um einen neuartigen dehnbaren Dehnungssensor und ein drahtloses Auslesesystem zu entwerfen und herzustellen. Schliesslich wurde die Validierung des dehnbaren Dehnungssensorsystems durch die Prüfung der drahtlosen Messleistung und die Implantation des Sensors in ein Schaf zur Messung der Sehnendehnung während Fortbewegungen in vivo durchgeführt.

Die Literaturübersicht gab einen Überblick über die verschiedenen Messverfahren, ihre wichtigsten Erkenntnisse, klinischen Implikationen und Grenzen. Insbesondere für implantierbare Dehnungssensoren haben verschiedene Sensoren, wie z. B. der Hall-Effekt-Dehnungswandler, ermöglicht, in-vivo-Dehnungen bei Menschen mit hoher Genauigkeit und Abtastrate zu messen. Einschränkungen früherer Sensortechnologien, einschließlich der starren Bauweise dieser Sensoren, führten jedoch zu einer Beeinflussung des Sensors durch das benachbarte Muskuloskeletale Gewebe. Noch wichtiger ist, dass diese Sensoren ein Kabel benötigen, um das Messsignal überzutragen, was sowohl die Anwendbarkeit bei In-vivo-Experimente und dynamische Messungen einschränkt, als auch Artefakte im Sensorsignal hervorrufen könnte durch das Biegen des Kabels. Daher sollten die derzeit

verwendeten Dehnungssensoren im Hinblick auf eine möglichst störungsfreie, drahtlose Datenübertragung und langfristiger Biokompatibilität revolutioniert werden, um den Anforderungen von In-vivo-MW-Dehnungsmessungen bei dynamischen Aktivitäten standhalten zu können.

In den experimentellen Arbeiten dieser Doktorarbeit wurde zuerst ein Prototyp eines dehnbaren Kondensators entwickelt, der aus goldbeschichteten Titandioxid-Nanodrähten besteht, die in weiche Silikonelastomere eingebettet sind. Der dehnbare Kondensator wurde mit einer Spule verbunden, um einen spanlosen drahtlosen Dehnungssensor für die induktive Auslesung seiner Resonanzfrequenz zu bilden. Auf der Grundlage des Sensorprototyps wurde ein fortschrittlicher dehnbare Dehnungssensor entwickelt, indem die Spulenstruktur, der PDMS-Guss und die Sensorbefestigungsmethode optimiert wurden. Darüber hinaus wurde in Zusammenarbeit eine speziell angefertigte Auslesebox entwickelt, um die Resonanzfrequenz des Sensors mit einer hohen Abtastrate (1 kHz) zu messen. Der Sensor kann auf die Oberfläche des MW genäht werden, sodass er entsprechend den Verformungen des Muskelskeletts gedehnt werden kann und eine indirekte Methode zur Beurteilung des MW-Dehnungsbildes bietet. Es wurde ein lineares Signal zwischen 0 und 25 % Dehnung nachgewiesen, und der Dehnungssensor in einer simulierten In-vivo-Umgebung und über 100'000 Ermüdungszyklen hinweg elektronisch stabil. Bei den drahtlosen Dehnungsmessungen zeigte der Dehnungssensor eine hervorragende Auflösung auf (0,1 % Dehnung, $\approx 9 \mu\text{m}$). Ex-vivo-Zugsehnenentests zeigten, dass der Sensor genaue Messungen der Belastung der Plantaris-Sehne von Schafen lieferte. Schliesslich wurde der Dehnungssensor im Schaf auf die mediale Gastrocnemius-Sehne implantiert und die Belastungsmessung während des Trottens der Schafe durchgeführt. Die Experimente zeigten, dass der Sensor in der Lage war, die sich wiederholenden Dehnungsmuster in der Sehne des Schafs aufzuzeichnen. Abschliessend wurde die Biokompatibilität des Sensors durch eine histologische Untersuchung nach einer 2-monatigen In-vivo-Implantation im Körper eines Schafs nachgewiesen.

Die Ergebnisse dieser Doktorarbeit zeigten, dass der Dehnungssensor die Sehnendehnung im lebendigen Körper erfolgreich messen konnte, was auf seine Anwendbarkeit für die Beantwortung wichtiger biomechanischer Fragen in Bezug auf die Funktionalitäten und pathologischen Mechanismen von MW hinweist. Darüber hinaus könnte die direkte Messung von MW-Dehnungen mit diesem Dehnungssensorsystem verwendet werden, um die Ergebnisse von Modellierungssimulationen zu validieren und aktuelle Muskuloskelettale Modelle zu optimieren. Letztendlich könnte sich dieses Dehnungssensorsystem zu einem Standardverfahren entwickeln, um die Genauigkeit von indirekten bildgebenden Messtechniken zu überprüfen, die oft unterschiedliche Dehnungsergebnisse liefern. Weitere Nachforschungen sind erforderlich, um den Dehnungssensor hinsichtlich seiner In-vivo-Robustheit und funktionelle Integrität zu verbessern, um eine langfristige In-vivo-Implantation und Messung während dynamischen Körperbewegungen zu gewährleisten.

Table of Contents

Statement of originality	2
Acknowledgements	3
Abstract	5
Zusammenfassung	7
Table of Contents	9
Chapter 1: Introduction and Background	11
1.1. The scientific and clinical significance of studying soft tissue strains	12
1.2. Musculoskeletal soft tissue strains	14
1.3. Sensors for measurement of MST strain: applications and limitations.....	15
1.4. Stretchable electronics and wireless signal transmission.....	18
1.5. Vision of the PhD thesis.....	20
1.6. References	21
Chapter 2: Techniques for <i>In-vivo</i> Measurement of Ligament and Tendon Strain: A Review	27
Abstract	28
2.1. Introduction	30
2.2. Materials and Methods	33
2.3. Implantable Strain Sensors.....	34
2.4. Virtual Fibre Elongation.....	39
2.5. Ultrasound	46
2.6. Summary and Perspectives.....	52
2.7. References	55
Chapter 3: Soft Electronic Strain Sensor with Chipless Wireless Readout: Toward Real-Time Monitoring of Bladder Volume.....	64
Abstract	66
3.1. Introduction	67
3.2. Results and Discussions	69
3.3. Conclusions	76
3.4. Experimental Section	77
3.5. References	79
Chapter 4: A Stretchable Strain Sensor System for Wireless Measurement of Musculoskeletal Soft Tissue Strains.....	81
Abstract	82

4.1. Introduction	83
4.2. Results and Discussion.....	86
4.3. Conclusions	95
4.4. Methods and Materials	96
4.5. References	100
Chapter 5: Stretchable Sensor Fabrication Protocol	106
5.1. Dispersion of TiO ₂ nanowire.....	107
5.2. Synthesis of Au-TiO ₂ nanowire	109
5.3. Membrane preparation and nanowire filtration.....	112
5.4. Fabrication of stretchable capacitor	114
5.5. Fabrication of LCR circuit	117
5.6. Fabrication of suture pads and PDMS embedding.....	120
Chapter 6: Discussion & conclusions.....	122
6.1. The optimized fabrication protocol stabilized the quality of the strain sensor	123
6.2. The function of the sensor fulfilled the prerequisites of MST strain measurement....	125
6.3. <i>In-vitro/in-vivo</i> sensor implantations and measurements.....	127
6.4. Limitations of the strain sensor system and outlook.....	128
6.5. Conclusion.....	129
6.6. Reference.....	130
Appendix	132
1. Supplementary of chapter 3.....	133
2. Supplementary of chapter 4.....	136
3. LCR strain sensor reader	138
4. Sync Box	142
Curriculum Vitae.....	145

Chapter 1: Introduction and Background

Musculoskeletal soft tissues (MSTs), such as tendons and ligaments, play principal roles in absorbing external impacts [1], stabilizing joints [2], and providing joint proprioception [3]. Injuries to critical MSTs, such as anterior cruciate ligament (ACL) or Achilles' tendon ruptures, can cause severe pain, limit musculoskeletal function, initiate degenerative pathways in neighbouring tissues such as tendinopathy and/or osteoarthritis, and permanently impact the quality of life [4-6]. Successful treatment of MST injuries requires a comprehensive understanding of the functional demands of MSTs during dynamic activities, the healing and pathologic adaptive response of a MST to loading, and the ability of surgical and rehabilitative treatments to restore native MST function.

1.1. The scientific and clinical significance of studying soft tissue strains

The importance of studying strain as a metric of MST biomechanical function, adaptation, and damage has been well established. Quantification of *in-vivo* MST strains during movement have revealed the complex interactions within muscle-tendon units that conserve energy during muscle contraction, amplify power output, and absorb shocks during impact [7, 8]. This knowledge is essential for musculoskeletal model validation [9], musculotendinous disorder diagnosis [10], and defining physiological loading conditions for *in-vitro* experiments [11] and tissue engineering [12]. Quantifying patellar tendon and ACL strains during jump landing [13] revealed concurrent increases in ACL and patellar tendon strains, indicating that quadriceps contraction was an important factor tensioning the ACL near full knee extension. Similar studies of ligament strains under loading have provided critical knowledge on their biomechanical contributions to joint stability [14, 15].

Investigating MST strains enables orthopaedic surgeries to be optimized [16, 17] and facilitates the development of safe and effective rehabilitation regimens. Surgical reconstructions of MST injuries generally aim to restore native strain patterns, in order to replicate the physiological function. Therefore, once the native strain patterns of MSTs are established, novel methods to intraoperatively quantify MST strains could additionally guide surgical decision making to allow optimal restoration of normative patterns during passive joint flexion. For example, the high recurrent patellar dislocation rate (15-40%) [18-20] and long-term patellofemoral symptoms [21-24] associated with medial patellofemoral ligament (MPFL) reconstruction are predominately caused by suboptimal surgical decisions (i.e. femoral attachment site, graft pre-tension) that induce non-optimal graft strains, resulting in compromised function. However, if the strain patterns of MPFL graft could be intraoperatively assessed during knee flexion-extension cycles, surgical decisions could be evaluated and corrected towards optimal outcomes. As *in-vivo* MST strains directly influence the collagen production rates of the MST fibroblasts [25], *in-vivo* quantification of MST strains during functional movements are critical for optimizing rehabilitation protocols that can stimulate ligament healing and avoid damage by progressively increasing graft loading [26, 27]. For example, squatting was found to cause higher ACL strains than many other

movements [27], and was thus suggested to be cautiously used as an exercise to prevent damaging loads to the healing tissue during the early stages of ACL rehabilitation.

In-vivo measurement of MST strain generally leverages three techniques, including implantable strain sensors, modelling combined with imaging, and ultrasound. Implantable strain sensors enable direct measurements of MST strains with high accuracy and minimal artefact, but are generally highly invasive, and current designs are not clinically viable. Modelling combined with imaging tracks the relative displacement of tissue-bone attachment sites to estimate the strain occurring in the tissue. However, the imaging techniques often require exposure to radiation, limit the activities that can be performed, and are only able to quantify bone-to-bone tissue strains (mainly ligaments). Ultrasound methods enable safe and non-invasive imaging of soft tissue deformation. However, ultrasound can only image superficial tissues, and measurements are confounded by errors associated with out-of-plane tissue motion. A comprehensive review of current techniques for *in-vivo* measurement of MST strain was performed within the framework of this thesis and is presented in Chapter 2.

1.2. Musculoskeletal soft tissue strains

One of the key prerequisites for the development of strain sensors to quantify the strains that occur in musculoskeletal tissues is an underlying understanding of magnitudes of strain and strain rates that the sensor will need to endure. While this is not the key focus of this thesis, an up-to-date review of the current knowledge on MST strains is indeed critical, and therefore is presented in summary format (Table 1).

Table 1. Summary of musculoskeletal soft tissue strains reported in the literature

Tissue	Activity	Maximum strain magnitude [%]
Achilles' tendon	Single leg hopping	8.3 ± 2.1 [28]
		8.0 ± 2.0 [29]
	Double-legged hopping	14.8 [30]
	Single leg Landing	6.0 [31]
	Walking	4.2 to 4.3 [32]
		4.6 [33]
		4.0 [34]
4.0 ± 1.2 [35]		
Running	7.4 ± 4.2 [36]	
	4.9 ± 1.2 [35]	
ACL*	Stair climbing	2.7 to 2.8 [37]
	Squatting with sport cord	Up to 4.0 [27]
	Rapid deceleration	Up to 5.5 [38]
	Gait	Up to 13.0 [39]
	Jump landing	Up to 12.0 [40]
Superficial medial collateral ligament	Lunge from full extension to maximal flexion gait	7.5 to 21.0 [41]
		Up to 4.7 [42]
Deep medial collateral ligament	Lunge from full extension to maximal flexion gait	17.0 to 20.0 [41]
		Up to 9.0 [42]
Lateral collateral ligament	Lunge from full extension to maximal flexion	-16.0 to 7.0 [41]

* The measurement was performed on the anteromedial bundle of the ACL

From these studies, it seems that any sensor aiming to assess MST strains *in vivo* should be capable of achieving strains of up to about 20%. However, caution should be taken, as studies investigating the failure strain of tendons suggest that collagenous structures begin to fail at around 6-9% strain [43]. As a result, it seems that the higher MST strains reported in some studies are somewhat dependent on the reference pose or reference length of the tissue assumed for the strain calculations [44].

1.3. Sensors for measurement of MST strain: applications and limitations

Implantable strain sensors can directly measure changes in the length of MSTs *in vivo*. After surgical implantation [45-47], such sensors convert tissue elongation into electrical signal perturbations [46], and transmit these signals to a measurement device for reverse calculation of the MST strains. Such “transducer” devices therefore convert a measured signal into an output that can be read and interpreted.

Over the past decades, multiple strain sensor designs were used to measure human MST strains. The magnetic field sensor was one of the first types of sensors used to measure MST strains *in vitro* [48]. The magnetic field sensor measures strain through tracking the variation in the magnetic field caused by displacing a metal rod within a wire coil. The liquid metal strain gauge (LMSG) is another type of sensor that has been used for *in-vitro* MST strain measurement [49]. The LMSG consists of compliant capillaries filled with mercury or a mixture of gallium and indium that deform when strain is applied, providing reliable measurements based on the quantification of strain-induced resistance changes in the capillaries. To date, LMSGs have only been implanted into animals [49, 50], but not humans. The first *in-vivo* implantable sensor measurement in humans was rather performed using an advanced magnetic field sensor — a Hall effect strain transducer (HEST), where Howe and co-workers arthroscopically implanted a HEST onto the anterior medial bundles of a subject’s ACL and found that the *in-vivo* strains increased during the Lachman test and isometric quadriceps contractions [51]. The differential variable reluctance transducer (DVRT) is another type of magnetic field sensor with improved (linear) sensing range, higher sensitivity, and larger signal to noise ratio compared to the HEST sensor [44, 52]. The DVRT was implanted in a human ACL to measure strains throughout a variety of movements, including lunge, step up/down, squatting, and bicycling [27, 53, 54]. Further measurements were performed by Cerulli and co-workers, who measured ACL strains during rapid deceleration movements and found peak strains of up to approximately 5.5 % occurred in the ACL, which temporally coincided with the peak ground reaction force. Similarly, fibre optic sensors have been applied to measure the forces occurring in human Achilles’ and patellar tendons during walking and jumping [55, 56]. These sensors assessed the modulation of intensity, phase, or wavelength of the light flow within the sensor [45] that occurs due to an applied load or deformation. Although it is suggested that the fibre optic sensor can be used for strain measurements in MSTs [46], no *in-vivo* human strain measurements have yet been performed. Similarly, implantable force transducers have been used to measure forces of human ACLs [57] and present an interesting technology for strain measurement *in vivo* [46, 58, 59].

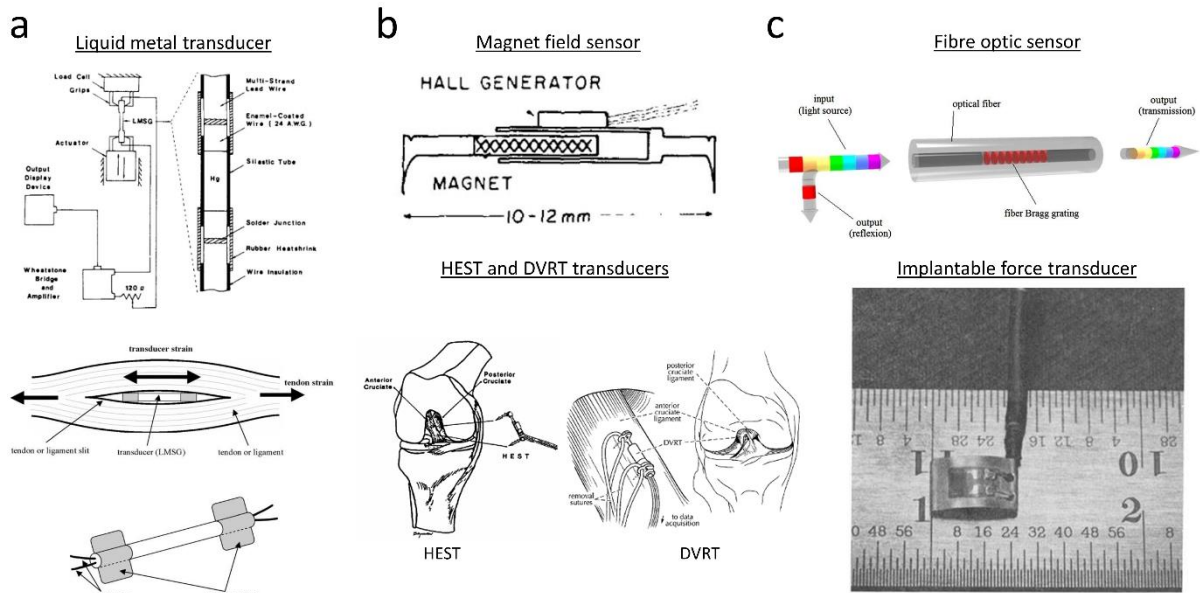


Figure 1. Conventional strain sensors that can be used to measure MST strains in humans. a) Liquid metal transducer [46, 49]. b) Magnet field sensor [48] and its improved version—Hall effect strain transducer (HEST) and differential variable reluctance transducer (DVRT) [60]. c) Fibre optic sensor [45] and implantable force transducer [58].

Although different strain sensor technologies have been developed and used for biomechanical measurements of MSTs, only a handful of sensors have been used for *in-vivo* measurements in humans, indicating that these conventional sensors present several major defects that limit their *in-vivo* applicability and hinder their translation into clinical settings. These limitations mainly originate from their structural design, signal transmission, and/or fixation methodologies. First, an excessively rigid construction leads to sensor impingement with neighbouring musculoskeletal tissues during functional movements, which limits the tissues and postures that can be measured [47]. For example, for implantation on the ACL, the HEST and DVRT sensors can only be implanted on the anteromedial bundle. Second, the aforementioned strain sensors use a cable crossing the skin to transmit the measurement signal to an external readout system [54, 61, 62]. The cable may cause discomfort that prevents natural execution of dynamic movements. Also, cable bending during body movement may perturb sensor signal and affect measurement accuracy [63]. In addition, the transcutaneous cable limits widespread clinical application of the strain sensor due to possible infection [64]. For sensor fixation to a MST, HESTs and DVRTs are attached by pressing barbs into the tissue. Barb fixation enables fast sensor attachment and easy removal so that it may be ideal for intraoperative implementation to measure MST strains during passive or static movements. However, barb fixation may lead to loosening or detachment from the soft tissue during dynamic body movement and damage during removal. It has been suggested that sensor measurement could be conducted two weeks after the implantation, as the local inflammation and fibrous encapsulation will facilitate sensor fixation to the soft tissue [65]. This may minimize sensor detachment from the tissue but significantly increase the risk of infection, as the skin incision cannot fully heal due to the sensor cable and duration of discomfort for the subject. Also, the sensor integrity and reliability are challenged with a significant time period between the sensor

implantation and signal recording [66]. Furthermore, traditional sensors made of metallic components are often non-biocompatible. Therefore, their long-term implantation and clinical utility are compromised [45]. Finally, sensor measurement could have significant errors when *in-vivo* strain occurs in a direction different from sensor implantation alignment [67]. However, sensors are generally visually aligned to the fibre direction in the MST during implantation, in an attempt to minimize any the associated errors.

To enable the dynamic *in-vivo* measurements needed for widespread clinical and research utility, implantable strain sensors should wirelessly transmit the signal to mitigate the many limitations due to wire crossing the skin. Contemporary technologies allow implantable sensors to wirelessly transmit signals to an external receiving device [68, 69]. Accordingly, wireless sensors have gained a great deal of interest in monitoring human physical and biological status in recent years and have been used in medical implantable sensors such as the Verasense orthopaedic sensor system, pacemakers, and bladder pressure sensors [70-72]. Wireless implantable sensors can be classified into active and passive designs. Active sensors, or the so-called self-powered sensors, use on-board batteries [73, 74] to transmit data across the skin, generally using Bluetooth [75]. For several active designs, their internal batteries can be recharged by an external device through inductive coupling [76], which greatly extends the life of the sensors. However, active sensors carry potential health hazards, and therefore require the electronics to be hermetically sealed [73, 74, 77]. Also, due to the inclusion of a battery, miniaturizing active sensors remains difficult. In contrast to active sensors, passive sensors are wirelessly excited and measured by an external system, often using piezoelectric materials or antenna coils [78-80]. Without the on-board battery, the design of passive sensors can be simplified, and the size can be greatly reduced. However, it should be noted that wireless signal transmission technologies such as electromagnetic energy or RFID technologies are easily affected by metallic materials nearby, possibly making them susceptible to e.g., metallic implants.

In conclusion, traditional strain sensors have enabled *in-vivo* measurements of human MST strains during functional movements, which has provided us great insights into the biomechanical functionality of MSTs. However, in order to fulfil the prerequisite for *in-vivo* MST strain measurements during dynamic activities, next-generation strain sensors should incorporate four essential features: a flexible design to minimize tissue impingement, wireless data transmission, a fast and robust fixation method, and biocompatibility for long term sensor implantation.

1.4. Stretchable electronics and wireless signal transmission

Recent advances in stretchable electronics have facilitated the development of membrane-like stretchable strain sensors. These sensors show great potential for clinical application through their unique soft constitutions, which can easily conform to the surface morphology of the target tissues and thus minimize sensor impingement. Stretchable strain sensors are typically fabricated by embedding conductive materials in stretchable elastomers. Stretchable strain sensors have been demonstrated outstanding conductivity, stretchability, and durability under idealized laboratory conditions [81-83].

State-of-the-art stretchable strain sensors are commonly categorized as capacitive-type and resistive-type sensors. In general, resistive-type sensors consist of a single conductive layer [84, 85]. Stretching the sensor changes the geometry of the conductive network as well as the intrinsic resistive response of conductive materials [86, 87], and thus increases the electrical resistance of the sensor [88]. Resistive-type sensors have gained a great deal of attention because they are highly stretchable but also provide outstanding electrical sensitivity [86, 88], while being easy to fabricate and operate [85]. Nevertheless, resistive-type sensors still require development to overcome the hysteresis and non-linearity common in their electromechanical responses [86, 89]. The counterparts, capacitive-type sensors, consist of two conductive layers separated by a dielectric layer [90-92]. Stretching the sensor thins the dielectric layer and deforms the overlapping area of the parallel plate capacitor [87, 89], and thus increases the capacitance of the sensor. While the electromechanical performance and biocompatibility of these novel flexible sensors require further advancement, the minimally disruptive technology is a clear innovation in implantable strain sensors that potentially provides improved characteristics for MST strain measurement.

Wireless stretchable strain sensors have recently made possible by leveraging wireless signal transmission technologies, now making clinical viability more plausible. Examples of this include a recent stretchable piezoelectric strain sensor system that used Near Field Communication technology to achieve battery-free sensing functionality and wireless data transmission (up to centimetres) in *ex-vivo* cardiac monitoring [93]. Similarly, a wireless stretchable inductor has been developed that integrated a strain sensing element, which also served as a receiver to concurrently transmit the signal [89]. However, despite the high stretchability and low hysteresis features exhibited by this strain sensor, the transmitted signals demonstrated lag even at low strain rates [89]. Capacitive-type stretchable sensors have been used for wireless signal transmission by simply adding a coil to the capacitor to create an inductor-capacitor-resistor (LCR) circuit [90]. Upon exciting the sensor via an external system, stretching the capacitor changes the resonant frequency (RF) of the oscillating current in the LCR sensor. A readout system (which can be integrated into the same external system) then records the RF signal of the sensor to inversely assess the strain applied.

The improved characteristics of stretchable strain sensors have drawn great attention in various applications in such as tracking human body movements [85, 92, 94-96], measuring human bladder volume, or cardiac monitoring [90, 93, 97]. However, very few stretchable strain sensors have been employed to quantify MST strains [98, 99] in either *in-vitro* or *in-vivo* environments. Zens and co-workers designed a capacitive-type sensor and used it to measure *in-vitro* anterolateral ligament strains on a knee specimen [99]. Boutry and co-workers developed an advanced biodegradable strain and pressure sensor, enabling the monitoring of long-term MST strains without the need of a second surgery for the sensor removal [98]. However, both of the sensors failed to incorporate wireless data transmission. Moreover, the sensors were glued onto the target tissue, which may be an inferior method for sensor fixation because it might lead to tissue damage and biocompatibility issues. Lee and co-workers developed a novel fibre strain sensor that can be sutured onto the MST for strain measurement [100], but wireless signal transmission was only achieved using a bulky stationary readout system.

Previously, a stretchable sensor fabrication technology has been developed by the Laboratory for Biosensors and Bioelectronics, ETH Zurich [101]. Specially, gold-coated titanium dioxide nanowires were filtered onto membranes using a nanowire filtration method. The nanowires were then transferred onto soft elastomers that enable fabrication of a stretchable conductor. The stretchable conductor showed outstanding stretchability and linearity during *ex-vivo* tensile testing and has been proved to be potentially suitable for measuring soft tissue deformations. This sensor fabrication technology thus has laid the excellent foundation for the development of wireless stretchable strain sensors for the *in-vivo* measurement of MST strains.

Despite of the potential of stretchable sensors for strain measurements of MSTs, a full validation of new sensor technologies is critical before translation into clinical application can be achieved. First, the ability of such soft sensors to endure long-term and high-rate fatigue loading has yet to be demonstrated. Resistance to fatigue loading is a fundamental prerequisite of *in-vivo* MST strain measurement since MSTs experience repeated and rapid (e.g., strain rates up to 50%/s in Achilles' tendon [102]) deformation in the human body. In addition, the *in-vivo* environment may affect the sensor properties and thus introduce drift in the original signal of the sensor. It is thus important to understand the effect of environmental changes on the measurement characteristics of the sensors. Here, new sensor technologies should be validated based on cadaveric implantations and measurements, as well as *in-vivo* animal testing and biocompatibility examination.

1.5. Vision of the PhD thesis

The overall vision of this PhD was to develop a wireless, biocompatible, stretchable strain sensor for utilization in assessing MST strains *in vivo*. This project also aimed to fully validate the strain sensor system for MST strain measurements through testing its wireless sensing performance and implanting it into a sheep to measure the tendon strains during dynamic movements *in vivo*. Three aims were established to realize three sections:

Aim 1: Review the current available technologies for *in-vivo* MST strain measurements

Different technologies, including image-based and sensor-based methods, have been used for *in-vivo* MST strain measurements. This section of the thesis aims to review these technologies, including the operating principles, key findings, limitations, and an outlook for their further development. To achieve this aim, a comparison of different technologies for strain measurement was performed (Chapter 2).

Aim 2: Optimize the sensor fabrication technologies in terms of sensor signal quality and physical robustness, and develop the prototype of the LCR stretchable strain sensor

Previously synthesized biocompatible nanowires and the techniques for their manufacture are available as a baseline for this development [103]. Building on this existing technology, the aim is to further develop, fabricate and test a stretchable conductor in order to determine the optimal nanowire filtration and transfer protocols. For a preliminary demonstration, the LCR strain sensor was sutured on the skin of a swine bladder *ex vivo*, and the inflation of the bladder was measured by the sensor (Chapter 3).

Aim 3: Develop and validate a wireless strain sensor system for *in-vivo* MST strain measurement

Based upon the prototype of the LCR strain sensor in aim 2, this study aimed to develop an implantable strain sensor by optimizing the structure, size, and elastomer sealing of the sensor. These developments targeted an improvement of the electrical performance, stability, and physical robustness of the sensor (Chapter 4). Furthermore, a new readout system was developed to wirelessly measure the sensor signal with a high sampling rate (Appendix, fast readout system). In addition, the sensitivity and resolution of the sensor system were characterized. The effect of fatigue loading, environmental changes on the sensor robustness and signal stability of the sensor system were validated (Chapter 4). An *Ex-vivo* tensile tendon test was performed using the sensor system to demonstrate the capacity of the sensor for MST strain measurements. Finally, for a proof-of-concept experiment, the sensor was implanted on the Achilles' tendon of a sheep and tendon strains were measured during trotting.

1.6. References

1. Devita, P. and W.A. Skelly, *Effect of landing stiffness on joint kinetics and energetics in the lower extremity*. Med Sci Sports Exerc, 1992. **24**(1): p. 108-15.
2. Amis, A.A. and G.P. Dawkins, *Functional anatomy of the anterior cruciate ligament. Fibre bundle actions related to ligament replacements and injuries*. J Bone Joint Surg Br, 1991. **73**(2): p. 260-7.
3. Frank, C.B., *Ligament structure, physiology and function*. J Musculoskelet Neuronal Interact, 2004. **4**(2): p. 199-201.
4. Gardinier, E.S., et al., *Altered loading in the injured knee after ACL rupture*. J Orthop Res, 2013. **31**(3): p. 458-64.
5. Kessler, M.A., et al., *Function, osteoarthritis and activity after ACL-rupture: 11 years follow-up results of conservative versus reconstructive treatment*. Knee Surg Sports Traumatol Arthrosc, 2008. **16**(5): p. 442-8.
6. Ahmad, C.S., et al., *Evaluation and management of hamstring injuries*. Am J Sports Med, 2013. **41**(12): p. 2933-47.
7. Cronin, N.J. and G. Lichtwark, *The use of ultrasound to study muscle-tendon function in human posture and locomotion*. Gait Posture, 2013. **37**(3): p. 305-12.
8. Mian, O.S., et al., *Gastrocnemius muscle-tendon behaviour during walking in young and older adults*. Acta Physiol (Oxf), 2007. **189**(1): p. 57-65.
9. Fernandez, J.W. and M.G. Pandy, *Integrating modelling and experiments to assess dynamic musculoskeletal function in humans*. Exp Physiol, 2006. **91**(2): p. 371-82.
10. Yoshida, K., et al., *Application of shear wave elastography for the gastrocnemius medial head to tennis leg*. Clin Anat, 2017. **30**(1): p. 114-119.
11. Draganich, L.F. and J.W. Vahey, *An in vitro study of anterior cruciate ligament strain induced by quadriceps and hamstrings forces*. J Orthop Res, 1990. **8**(1): p. 57-63.
12. An, K.N., *In vivo force and strain of tendon, ligament, and capsule*. Functional Tissue Engineering, 2003: p. 96-105.
13. Englander, Z.A., et al., *Patellar Tendon Orientation and Strain Are Predictors of ACL Strain In Vivo During a Single-Leg Jump*. Orthopaedic Journal of Sports Medicine, 2021. **9**(3).
14. Amis, A.A., et al., *Anatomy and biomechanics of the medial patellofemoral ligament*. Knee, 2003. **10**(3): p. 215-20.
15. Li, G., et al., *The importance of quadriceps and hamstring muscle loading on knee kinematics and in-situ forces in the ACL*. J Biomech, 1999. **32**(4): p. 395-400.
16. Hosseini Nasab, S.H., et al., *Length-Change Patterns of the Collateral Ligaments During Functional Activities After Total Knee Arthroplasty*. Ann Biomed Eng, 2020. **48**(4): p. 1396-1406.
17. Tsai, T.Y., et al., *In-vivo elongation of anterior and posterior cruciate ligament in bi-cruciate retaining total knee arthroplasty*. J Orthop Res, 2018. **36**(12): p. 3239-3246.
18. Macnab, I., *Recurrent dislocation of the patella*. J Bone Joint Surg Am, 1952. **34 A**(4): p. 957-67; passim.

19. Lewallen, L.W., A.L. McIntosh, and D.L. Dahm, *Predictors of recurrent instability after acute patellofemoral dislocation in pediatric and adolescent patients*. Am J Sports Med, 2013. **41**(3): p. 575-81.
20. Maenpaa, H. and M.U. Lehto, *Patellar dislocation. The long-term results of nonoperative management in 100 patients*. Am J Sports Med, 1997. **25**(2): p. 213-7.
21. Cofield, R.H. and R.S. Bryan, *Acute dislocation of the patella: results of conservative treatment*. J Trauma, 1977. **17**(7): p. 526-31.
22. Zhang, G.Y., et al., *Incidence of second-time lateral patellar dislocation is associated with anatomic factors, age and injury patterns of medial patellofemoral ligament in first-time lateral patellar dislocation: a prospective magnetic resonance imaging study with 5-year follow-up*. Knee Surg Sports Traumatol Arthrosc, 2019. **27**(1): p. 197-205.
23. Askenberger, M., et al., *Medial Patellofemoral Ligament Injuries in Children With First-Time Lateral Patellar Dislocations: A Magnetic Resonance Imaging and Arthroscopic Study*. Am J Sports Med, 2016. **44**(1): p. 152-8.
24. Balcarek, P., et al., *Patellar dislocations in children, adolescents and adults: a comparative MRI study of medial patellofemoral ligament injury patterns and trochlear groove anatomy*. Eur J Radiol, 2011. **79**(3): p. 415-20.
25. Hsieh, A.H., et al., *Time-dependent increases in type-III collagen gene expression in medial collateral ligament fibroblasts under cyclic strains*. J Orthop Res, 2000. **18**(2): p. 220-7.
26. Beynnon, B.D., et al., *Anterior cruciate ligament strain behavior during rehabilitation exercises in vivo*. Am J Sports Med, 1995. **23**(1): p. 24-34.
27. Beynnon, B.D., et al., *The strain behavior of the anterior cruciate ligament during squatting and active flexion-extension. A comparison of an open and a closed kinetic chain exercise*. Am J Sports Med, 1997. **25**(6): p. 823-9.
28. Lichtwark, G.A. and A.M. Wilson, *In vivo mechanical properties of the human Achilles tendon during one-legged hopping*. J Exp Biol, 2005. **208**(Pt 24): p. 4715-25.
29. Farris, D.J., G. Trewartha, and M.P. McGuigan, *Could intra-tendinous hyperthermia during running explain chronic injury of the human Achilles tendon?* Journal of Biomechanics, 2011. **44**(5): p. 822-826.
30. Stosic, J. and T. Finni, *Gastrocnemius tendon length and strain are different when assessed using straight or curved tendon model*. European Journal of Applied Physiology, 2011. **111**(12): p. 3151-3154.
31. Werkhausen, A., et al., *Modulation of muscle-tendon interaction in the human triceps surae during an energy dissipation task*. Journal of Experimental Biology, 2017. **220**(22): p. 4141-4149.
32. Ishikawa, M., et al., *Muscle-tendon interaction and elastic energy usage in human walking*. J Appl Physiol (1985), 2005. **99**(2): p. 603-8.
33. Lichtwark, G.A. and A.M. Wilson, *Interactions between the human gastrocnemius muscle and the Achilles tendon during incline, level and decline locomotion*. Journal of Experimental Biology, 2006. **209**(21): p. 4379-4388.
34. Delabastita, T., et al., *Distal-to-proximal joint mechanics redistribution is a main contributor to reduced walking economy in older adults*. Scandinavian Journal of Medicine & Science in Sports, 2021. **31**(5): p. 1036-1047.

35. Kharazi, M., et al., *Quantifying mechanical loading and elastic strain energy of the human Achilles tendon during walking and running*. Sci Rep, 2021. **11**(1): p. 5830.
36. Farris, D.J., et al., *The Effects of Orthotic Heel Lifts on Achilles Tendon Force and Strain During Running*. Journal of Applied Biomechanics, 2012. **28**(5): p. 511-519.
37. Fleming, B.C., et al., *The strain behavior of the anterior cruciate ligament during stair climbing: an in vivo study*. Arthroscopy, 1999. **15**(2): p. 185-91.
38. Cerulli, G., et al., *In vivo anterior cruciate ligament strain behaviour during a rapid deceleration movement: case report*. Knee Surg Sports Traumatol Arthrosc, 2003. **11**(5): p. 307-11.
39. Wu, J.L., et al., *Kinematics of the anterior cruciate ligament during gait*. Am J Sports Med, 2010. **38**(7): p. 1475-82.
40. Taylor, K.A., et al., *Measurement of in vivo anterior cruciate ligament strain during dynamic jump landing*. J Biomech, 2011. **44**(3): p. 365-71.
41. Hosseini, A., et al., *In vivo length change patterns of the medial and lateral collateral ligaments along the flexion path of the knee*. Knee Surgery Sports Traumatology Arthroscopy, 2015. **23**(10): p. 3055-3061.
42. Liu, F., et al., *In vivo length patterns of the medial collateral ligament during the stance phase of gait*. Knee Surg Sports Traumatol Arthrosc, 2011. **19**(5): p. 719-27.
43. Liao, H. and S.M. Belkoff, *A failure model for ligaments*. J Biomech, 1999. **32**(2): p. 183-8.
44. Beynnon, B.D. and B.C. Fleming, *Anterior cruciate ligament strain in-vivo: a review of previous work*. J Biomech, 1998. **31**(6): p. 519-25.
45. Roriz, P., et al., *From conventional sensors to fibre optic sensors for strain and force measurements in biomechanics applications: a review*. J Biomech, 2014. **47**(6): p. 1251-61.
46. Ravary, B., et al., *Strain and force transducers used in human and veterinary tendon and ligament biomechanical studies*. Clin Biomech (Bristol, Avon), 2004. **19**(5): p. 433-47.
47. Fleming, B.C. and B.D. Beynnon, *In vivo measurement of ligament/tendon strains and forces: a review*. Ann Biomed Eng, 2004. **32**(3): p. 318-28.
48. Arms, S., et al., *Strain measurement in the medial collateral ligament of the human knee: an autopsy study*. J Biomech, 1983. **16**(7): p. 491-6.
49. Brown, T.D., et al., *Dynamic performance characteristics of the liquid metal strain gage*. J Biomech, 1986. **19**(2): p. 165-73.
50. Jansen, M.O., et al., *Mechanical properties of the tendinous equine interosseus muscle are affected by in vivo transducer implantation*. J Biomech, 1998. **31**(5): p. 485-90.
51. Howe, J.G., et al., *Arthroscopic strain gauge measurement of the normal anterior cruciate ligament*. Arthroscopy, 1990. **6**(3): p. 198-204.
52. Beynnon, B.D., et al., *The effect of functional knee bracing on the anterior cruciate ligament in the weightbearing and nonweightbearing knee*. Am J Sports Med, 1997. **25**(3): p. 353-9.
53. Heijne, A., et al., *Strain on the anterior cruciate ligament during closed kinetic chain exercises*. Med Sci Sports Exerc, 2004. **36**(6): p. 935-41.
54. Fleming, B.C., et al., *The strain behavior of the anterior cruciate ligament during bicycling. An in vivo study*. Am J Sports Med, 1998. **26**(1): p. 109-18.
55. Finni, T., P.V. Komi, and J. Lukkariniemi, *Achilles tendon loading during walking: application of a novel optic fiber technique*. Eur J Appl Physiol Occup Physiol, 1998. **77**(3): p. 289-91.

56. Finni, T., P.V. Komi, and V. Lepola, *In vivo human triceps surae and quadriceps femoris muscle function in a squat jump and counter movement jump*. Eur J Appl Physiol, 2000. **83**(4 -5): p. 416-26.
57. Roberts, C.S., *In vivo measurement of human anterior cruciate ligament forces during knee extension exercises*. Trans ORS, 1994. **15**: p. 84.
58. Glos, D.L., et al., *In vitro evaluation of an implantable force transducer (IFT) in a patellar tendon model*. J Biomech Eng, 1993. **115**(4A): p. 335-43.
59. Markolf, K.L., et al., *In situ calibration of miniature sensors implanted into the anterior cruciate ligament part I: Strain measurements*. Journal of Orthopaedic Research, 1998. **16**(4): p. 455-463.
60. Zhang, Q., et al., *Techniques for In Vivo Measurement of Ligament and Tendon Strain: A Review*. Ann Biomed Eng, 2021. **49**(1): p. 7-28.
61. Fukashiro, S., et al., *Comparison between the directly measured achilles tendon force and the tendon force calculated from the ankle joint moment during vertical jumps*. Clin Biomech (Bristol, Avon), 1993. **8**(1): p. 25-30.
62. Edsfieldt, S., et al., *In vivo flexor tendon forces generated during different rehabilitation exercises*. J Hand Surg Eur Vol, 2015. **40**(7): p. 705-10.
63. Erdemir, A., et al., *Fiberoptic measurement of tendon forces is influenced by skin movement artifact*. J Biomech, 2003. **36**(3): p. 449-55.
64. D'Lima, D.D., et al., *In vivo knee moments and shear after total knee arthroplasty*. J Biomech, 2007. **40 Suppl 1**: p. S11-7.
65. Herzog, W., E.M. Hasler, and T.R. Leonard, *In-situ calibration of the implantable force transducer*. J Biomech, 1996. **29**(12): p. 1649-52.
66. Korvick, D.L., et al., *The use of an implantable force transducer to measure patellar tendon forces in goats*. Journal of Biomechanics, 1996. **29**(4): p. 557-561.
67. Rupert, M., et al., *Influence of sensor size on the accuracy of in-vivo ligament and tendon force measurements*. J Biomech Eng, 1998. **120**(6): p. 764-9.
68. Denning, T., et al., *Patients, Pacemakers, and Implantable Defibrillators: Human Values and Security for Wireless Implantable Medical Devices*. Chi2010: Proceedings of the 28th Annual Chi Conference on Human Factors in Computing Systems, Vols 1-4, 2010: p. 917-+.
69. Ankarali, Z.E., et al., *A Comparative Review on the Wireless Implantable Medical Devices Privacy and Security*. 2014 Eai 4th International Conference on Wireless Mobile Communication and Healthcare (Mobihealth), 2014: p. 246-249.
70. Campi, T., et al., *Wireless Power Transfer Charging System for AIMDs and Pacemakers*. Ieee Transactions on Microwave Theory and Techniques, 2016. **64**(2): p. 633-642.
71. Majerus, S.J.A., et al., *Wireless, Ultra-Low-Power Implantable Sensor for Chronic Bladder Pressure Monitoring*. Acm Journal on Emerging Technologies in Computing Systems, 2012. **8**(2).
72. Cho, K.J., et al., *Objective quantification of ligament balancing using VERASENSE in measured resection and modified gap balance lota knee arthroplasty*. BMC Musculoskeletal Disorders, 2018. **19**.
73. Klosterhoff, B.S., et al., *Wireless Implantable Sensor for Noninvasive, Longitudinal Quantification of Axial Strain Across Rodent Long Bone Defects*. J Biomech Eng, 2017. **139**(11).

74. Weydts, T.B., L.; Soebadi, M. A.; De Ridder, D.; Puers, R., *A novel method to investigate bladder wall behavior by acceleration and pressure sensing*. *Sensors and Actuators A*, 2018. **280**: p. 376-382.
75. Omre, A.H., *Bluetooth low energy: wireless connectivity for medical monitoring*. *J Diabetes Sci Technol*, 2010. **4**(2): p. 457-63.
76. Hausleitner, C., et al., *New concepts of wireless interrogable passive sensors using nonlinear components*. *Proceedings of the 2001 12th IEEE International Symposium on Applications of Ferroelectrics, Vols I and II*, 2001: p. 851-854.
77. Jiang, H.C., N. M.; Zareei, A.; Nejati, S.; Waimin, J. F.; Chittiboyina, S.; Niedert, E. E.; Soleimani, T.; Lelièvre, S. A.; Georgen, C. J.; Rahimi, R., *A Wireless Implantable Strain Sensing Scheme Using Ultrasound Imaging of Highly Stretchable Zinc Oxide/Poly Dimethylacrylamide Nanocomposite Hydrogel*. *ACS Applied Bio Materials*, 2020. **3**: p. 4012-4024.
78. Lee, K.J.C., N.; Kim, S., *Batteryless, wireless strain sensor using resonant frequency modulation*. *Sensors*, 2018. **18**(3955).
79. Baldi, A., W. Choi, and B. Ziaie, *A self-resonant frequency-modulated micromachined passive pressure transducer*. *IEEE Sensors Journal*, 2003. **3**(6): p. 728-733.
80. Fang, Q., et al., *Developing a Wireless Implantable Body Sensor Network in MICS Band*. *IEEE Transactions on Information Technology in Biomedicine*, 2011. **15**(4): p. 567-576.
81. Cai, L., et al., *Super-stretchable, transparent carbon nanotube-based capacitive strain sensors for human motion detection*. *Sci Rep*, 2013. **3**: p. 3048.
82. Hu, W.L., et al., *Elastomeric transparent capacitive sensors based on an interpenetrating composite of silver nanowires and polyurethane*. *Applied Physics Letters*, 2013. **102**(8).
83. Cohen, D.J., et al., *A Highly Elastic, Capacitive Strain Gauge Based on Percolating Nanotube Networks*. *Nano Letters*, 2012. **12**(4): p. 1821-1825.
84. Sang, S.B., et al., *Highly sensitive wearable strain sensor based on silver nanowires and nanoparticles*. *Nanotechnology*, 2018. **29**(25).
85. Cai, Y.Q., J.; Li, W.; Tyagi, A.; Liu, Z.; Hossain, D.; Chen, H.; Kim, J.-K.; Liu, H.; Zhuan, M.; You, J.; Xu, F.; Lu, X.; Sun, D.; Luo, Z., *A stretchable, conformable, and biocompatible graphene strain sensor based on a structured hydrogel for clinical application*. *Journal of Materials Chemistry A*, 2019. **7**: p. 27099-27109.
86. Souri, H.B., H.; Jusufi, A.; Radacsi, N.; Stokes, A. A.; Park, I.; Sitti, M.; Amjadi, M., *Wearable and Stretchable Strain Sensors: Materials, Sensing Mechanisms, and Applications*. *Advanced Intelligent Systems*, 2020. **2**(2000039).
87. Seyedin, S.Z., P.; Naebe, M.; Yin, S.; Chen, J.; Wang, X.; Razal, J. M., *Textile strain sensors: a review of the fabrication technologies, performance evaluation and applications*. *Materials Horizons*, 2019. **6**: p. 219-249.
88. Wang, Z., Y. Cong, and J. Fu, *Stretchable and tough conductive hydrogels for flexible pressure and strain sensors*. *J Mater Chem B*, 2020. **8**(16): p. 3437-3459.
89. Chen, H.-Y.C., A. T., *A Stretchable Inductor With Integrated Strain Sensing and Wireless Signal Transfer*. *IEEE Sensors Journal*, 2020. **20**(13): p. 7384-7391.
90. Stauffer, F., et al., *Soft Electronic Strain Sensor with Chipless Wireless Readout: Toward Real-Time Monitoring of Bladder Volume*. *Advanced Materials Technologies*, 2018. **3**(6).
91. Cui, Z., et al., *Design and operation of silver nanowire based flexible and stretchable touch sensors*. *Journal of Materials Research*, 2015. **30**(1): p. 79-85.

92. Hou, C.X., W.; Wu, R.; Wang, Y.; Xu, Q.; Liu, X. Y.; Guo, W., *A Biodegradable and Stretchable Protein-Based Sensor as Artificial Electronic Skin for Human Motion Detection*. *Small*, 2019. **15**(1805084): p. 1-8.
93. Sun, R.C., Sara Correia; Chen, Yan; Xiang, Chaoqun; Xu, Lulu; Zhan, Bing; Chen, Mudan; Farrow, Ian; Scarpa, Fabrizio; Rossiter, Jonathan, *Stretchable Piezoelectric Sensing Systems for Self-Powered and Wireless Health Monitoring*. *Advanced Materials Technologies*, 2019. **4**(1900100).
94. Valentine, A.D., et al., *Hybrid 3D Printing of Soft Electronics*. *Adv Mater*, 2017. **29**(40).
95. Pang, C., C. Lee, and K.Y. Suh, *Recent advances in flexible sensors for wearable and implantable devices*. *Journal of Applied Polymer Science*, 2013. **130**(3): p. 1429-1441.
96. Kim, D., S.K. Ahn, and J. Yoon, *Highly Stretchable Strain Sensors Comprising Double Network Hydrogels Fabricated by Microfluidic Devices*. *Advanced Materials Technologies*, 2019. **4**(7).
97. Dakurah, M.N., et al., *Implantable Bladder Sensors: A Methodological Review*. *International Neurourology Journal*, 2015. **19**(3): p. 133-141.
98. Boutry, C.M., et al., *A stretchable and biodegradable strain and pressure sensor for orthopaedic application*. *Nature Electronics*, 2018. **1**(5): p. 314-321.
99. Zens, M., et al., *A New Approach to Determine Ligament Strain Using Polydimethylsiloxane Strain Gauges: Exemplary Measurements of the Anterolateral Ligament*. *Journal of Biomechanical Engineering-Transactions of the Asme*, 2014. **136**(12).
100. Lee, J., et al., *Stretchable and suturable fibre sensors for wireless monitoring of connective tissue strain*. *Nature Electronics*, 2021. **4**(4): p. 291-301.
101. Tybrandt, K., F. Stauffer, and J. Voros, *Multilayer Patterning of High Resolution Intrinsically Stretchable Electronics*. *Sci Rep*, 2016. **6**: p. 25641.
102. Wren, T.A., et al., *Mechanical properties of the human achilles tendon*. *Clin Biomech (Bristol, Avon)*, 2001. **16**(3): p. 245-51.
103. Tybrandt, K., et al., *High-Density Stretchable Electrode Grids for Chronic Neural Recording*. *Adv Mater*, 2018.

Chapter 2: Techniques for *In-vivo* Measurement of Ligament and Tendon Strain: A Review

Qiang Zhang, Naomi C. Adam, S. H. Hosseini Nasab, William R. Taylor, and Colin R. Smith

Institute for Biomechanics, ETH Zurich, Leopold-Ruzicka-Weg 4, 8093 Zurich, Switzerland

Published as:

Zhang, Q., N. C. Adam, S. H. Hosseini Nasab, W. R. Taylor and C. R. Smith (2021). "Techniques for *In-Vivo* Measurement of Ligament and Tendon Strain: A Review." *Ann Biomed Eng* 49(1): 7-28.

Abstract

The critical clinical and scientific insights achieved through knowledge of *in-vivo* musculoskeletal soft tissue strains has motivated the development of relevant measurement techniques. This review provides a comprehensive summary of the key findings, limitations, and clinical impacts of these techniques to quantify musculoskeletal soft tissue strains during dynamic movements. Current technologies generally leverage three techniques to quantify *in-vivo* strain patterns, including implantable strain sensors, virtual fibre elongation, and ultrasound. (1) Implantable strain sensors enable direct measurements of tissue strains with high accuracy and minimal artefact, but are highly invasive and current designs are not clinically viable. (2) The virtual fibre elongation method tracks the relative displacement of tissue attachments to measure strains in both deep and superficial tissues. However, the associated imaging techniques often require exposure to radiation, limit the activities that can be performed, and only quantify bone-to-bone tissue strains. (3) Ultrasound methods enable safe and non-invasive imaging of soft tissue deformation. However, ultrasound can only image superficial tissues, and measurements are confounded by out-of- plane tissue motion. Finally, all *in-vivo* strain measurement methods are limited in their ability to establish the slack length of musculoskeletal soft tissue structures. Despite the many challenges and limitations of these measurement techniques, knowledge of *in-vivo* soft tissue strain has led to improved clinical treatments for many musculoskeletal pathologies including anterior cruciate ligament reconstruction, Achilles' tendon repair, and total knee replacement. This review provides a comprehensive understanding of these measurement techniques and identifies the key features of *in-vivo* strain measurement that can facilitate innovative personalized sports medicine treatment.

Keywords: Ligament strains, Tendon strains, Biosensors, Loading conditions, Soft tissue function, *In-vivo* measurement, Dynamic imaging, Stretchable sensors.

Abbreviations:

ACL	Anterior cruciate ligament
AT	Achilles' tendon
MRI	Magnetic resonance imaging
CT	Computed tomography
HEST	Hall Effect Strain Transducer
DVRT	Differential Variable Reluctance Transducer
FOV	Field of view
sMCL	Superficial medial collateral ligament

MPFL	Medial patellofemoral ligament
TKA	Total knee arthroplasty
RSA	Roentgen stereophotogrammetric analysis
MJ	Myotendinous junction
sATMJ	Soleus-AT myotendinous junction
RF	Radiofrequency
ROI	Region of interest
MG	Medial gastrocnemius
ICC	Intra-class correlation coefficient

2.1. Introduction

In addition to considerable pain and loss of function experienced by patients [1], musculoskeletal soft tissue injuries present a considerable financial burden to health care systems worldwide. Some 200'000 anterior cruciate ligament (ACL) injuries [2, 3] occur annually in the Unites States alone, and nearly half of them require reconstructive surgery [4]. The socioeconomic costs of the resulting medical treatment have been estimated to be over one billion dollars annually [5, 6]. In Sweden, the average cost of surgical management of acute Achilles' tendon (AT) ruptures in 2009-2010 was around \$10'000 [7]. Moreover, revision rates following initial treatment for AT rupture (2%-8%) [8, 9] and ACL revisions (3-16%) [10, 11] suggest that more effective treatment offer considerable potential exists for not only reducing costs, but also improving patients' functional outcome.

Transforming sports medicine therapies to address current treatment shortcomings requires a comprehensive understanding regarding the functional demands withstood by musculoskeletal soft tissues during activities of daily living in healthy, injury, and pathologic conditions. A detailed understanding of *in-vivo* ligament and tendon strains is not only important for identifying injury mechanisms, informing surgical reconstructions and optimizing rehabilitation protocols, but also essential for defining physiologic loading conditions for *in-vitro* experiments and tissue engineered constructs. Therefore, the measurement of *in-vivo* musculoskeletal soft tissue strain patterns during functional movements is critical for both facilitating scientific discoveries and driving innovative clinical treatments.

The importance of soft tissue strain to biomechanical tissue function and adaptation has been well established. In 1847, Wertheim demonstrated that the stress-strain relationship in animal tissue does not follow the linear relationship dictated by Hooke's law [12]. In the 1960s, the introduction of Fung's Law provided the contemporary understanding of soft tissue viscoelasticity, building a more complete concept of the tissue deformation response to loading [13]. Shortly afterwards, it was discovered that both soft tissue strain magnitude and rate had a direct influence on the failure properties of ligaments [14] and tendons [15]. In 1992, it was discovered that the strain magnitude, not stress, experienced by muscle fibres was directly related to damage severity [16]. However, despite the importance of soft tissue strain being recognized for decades, clinical translation of this knowledge has been hindered by the limited *in-vivo* measurements of tissue strain magnitudes and rates during dynamic movements.

In clinical settings, improved knowledge of *in-vivo* ligament strains [17] has facilitated key innovations in reconstruction techniques and rehabilitation for ligament injuries [18]. For example, in the 1990s, it was thought that the bone tunnel during ACL reconstruction surgeries should be positioned to achieve graft isometry throughout flexion [19, 20]. However, research into the role of loading on graft tissue health [21, 22] and the contribution of ACL strain to knee stability [23] led to an evolution of the

surgical technique such that current approaches aim to position the tunnels in the centre of the native ACL attachment footprints to better replicate the strain patterns experienced by the native tissue [24]. With respect to rehabilitation, sensor measurements of *in-vivo* ACL strain showed a significant increase when the knee moved to extended postures [25, 26], which has informed activity selection for post-operative rehabilitation. However, innovation of clinical therapies for many other pathologies is hindered by the limited *in-vivo* strain data available for many other ligaments and tendons, especially during functional and rehabilitative activities.

In-vivo strain measurements also provide critical insights into muscle-tendon function by enabling the elongation of the muscle fibres, tendon, and aponeurosis to be independently quantified [27]. Measurements of muscle fibre lengths and velocities during movement enable investigation into how individuals leverage optimal force-length and force-velocity muscle contraction conditions. Ultrasound studies indicate that the tendon can act as a buffer to overall muscle-tendon unit stretch, resulting in strains within the individual tissues that do not reflect the overall length change of the muscle-tendon unit [27]. For example, during early stance in walking, the overall length of the triceps surae muscle-tendon unit increases substantially, but the lateral gastrocnemius fibres lengthen only to a small degree [28], while the medial gastrocnemius and soleus fibres even remain isometric [29]. At push-off, all of the triceps surae muscles shorten, but at a much slower rate than the tendon and muscle-tendon unit as a whole. This demonstrates the importance of *in-vivo* strain measurements to reveal the complex interactions within muscle-tendon units to conserve energy during muscle contraction, amplify power output, and absorb shocks during impact [30].

An improved understanding of *in-vivo* soft tissue strains will also provide important insights into how humans modulate their neuromuscular coordination to generate movement. When coupled with traditional motion analysis techniques, *in-vivo* strain measurements could enable an improved understanding of how the body leverages elastic energy storage in tendons [31]. Furthermore, dynamic strain measurements of all the soft tissues crossing a joint may provide key insights towards resolving muscle redundancy [32]. This problem seeks to determine how the externally measurable joint torques during movement are distributed to the redundant musculoskeletal system, resulting in one of the most famous unsolved problems in biomechanics [33].

The critical need for *in-vivo* quantification of musculoskeletal tissue strain for both clinical and basic science applications has inspired the development of three main measurement techniques: 1) implantable strain sensors, 2) virtual fibre elongation, and 3) ultrasound. Implantable strain sensors have largely been applied to measure *in-vivo* ACL strains [34-36], but such technologies have mostly been implemented during controlled movements and in sterile surgical environments. The virtual fibre elongation method uses bone position from image-based methods including fluoroscopy [37-39], ultrasound [40], open magnetic resonance imaging (open-MRI) [41, 42], or computed tomography (CT) [43, 44] to derive *in-vivo* ligament and tendon strains. Ultrasound technique enables dynamic non-

invasive planar imaging of soft tissue structures, and has mostly been applied to measure muscle [27, 45] and tendon [46, 47] deformation. Each technique presents different advantages and limitations regarding accuracy, invasiveness, safety, and activities that can be measured. In addition, previous studies have chosen different approaches to define the fibre reference length [48-51]. As a result, the reported strain data may not represent the real soft tissue strain, and thus understanding the true loading condition within the tissue remains challenging. Therefore, the abilities of these measurement techniques to determine the slack length of soft tissue should be fully reviewed and discussed. The technologies involved in *in-vivo* strain measurement have been previously reviewed [35, 36, 52, 53], however there has not yet been a comprehensive summary of the key findings and clinical impacts of each methodology. The purpose of this study is therefore to provide an overview of *in-vivo* tendon and ligament strain measurement methodologies and their key findings, clinical implications, and limitations, as well as to identify technological developments that may lead to clinical and basic science advances in sports medicine.

2.2. Materials and Methods

2.2.1. Literature search and selection

Articles were searched using the keywords “sensor*”, “gauge*”, and “transduc*”, “imag*”, “ultrasound*”, “fluoroscop*” as well as “tendon*”, “ligament*”, “muscle*”, “length change*”, “strain*” and “elongat*” in the Pubmed and EMBASE databases. A total of 9842 articles were found. The titles and abstracts of all articles were firstly screened by one author to exclude clearly irrelevant articles. Two authors then reviewed the full texts of the remaining articles to identify articles discussed in this review. As this is a narrative review, the two authors also searched the reference lists of these articles to identify any other relevant articles that had not been found through the above search. One experienced author discussed these candidate articles with the two authors to make a final decision on their inclusion. Finally, 151 articles were included for reviewing.

2.2.2. Strain calculation

Strain (ε) is traditionally defined using Equation 1 in the biomechanics literature:

$$\varepsilon = \frac{l - l_0}{l_0} \quad (1)$$

Where l is the tissue length and l_0 is the slack length or reference length. Slack length is the length at which a tissue begins exhibiting force when it is stretched. The ability of each measurement technique to quantify tissue slack length is detailed in the following sections. In many studies, the true slack length was not measured and instead a reference length, the length of the tissue in a defined body posture is used to calculate strain [49, 54]. Thus, comparing strains between studies requires careful consideration of the l_0 definition.

2.3. Implantable Strain Sensors

Implantable sensors have been employed to directly measure *in-vivo* ligament strain patterns in humans. Similar sensors have been applied to measure human tendon forces. Typically, these sensors leverage similar working principles, where mechanical loading or deformation of the tissue induces changes in their electric signals (voltage, resistance, or capacitance). Buckle transducers, liquid metal strain gauges, fibre optic transducers, and sonomicrometry crystals have all been used for *in-vivo* force and strain measurements in animal studies to assess muscle, tendon, and ligament function during dynamic activities [35, 53]. For example, liquid metal strain gauges have been applied to measure *strain* patterns in rabbit ATs and in horse suspensory ligaments [55, 56]. In addition, buckle transducers and fibre optic transducers have been applied to measure AT *force* in humans during walking and jumping [57, 58].

While many aforementioned sensor designs have been demonstrated for force measurements in humans and strain measurements in animals, only Hall Effect Strain Transducers (HESTs) and Differential Variable Reluctance Transducers (DVRTs) have been used to directly measure *in-vivo* strains in human musculoskeletal tissue [35]. Therefore, the following discussion focuses on the properties, applications, and limitations of these sensors.

2.3.1. Measurement technology and experimental methods

To detect displacement, HEST sensors measure the change in voltage resulting from relative movement between a magnet and a Hall-effect magnetic sensor, whereas DVRTs measure the movement of a magnetic core within two coil windings by measuring the resulting change in magnetic reluctance [34]. The parameters of these two sensors are displayed in Fig. 1a [34, 35]. Beynnon and co-workers arthroscopically implanted a HEST sensor onto the ACL of subjects under local anaesthesia [59], mounting the sensor by pressing on two fixation barbs (Fig. 1b). ACL strains were then quantified during limited functional movements before removal of the sensor. The measurement procedures of DVRT sensors are similar to the HEST sensors (Fig. 1c) [60].

2.3.2. Slack length

Implantable Strain Sensor

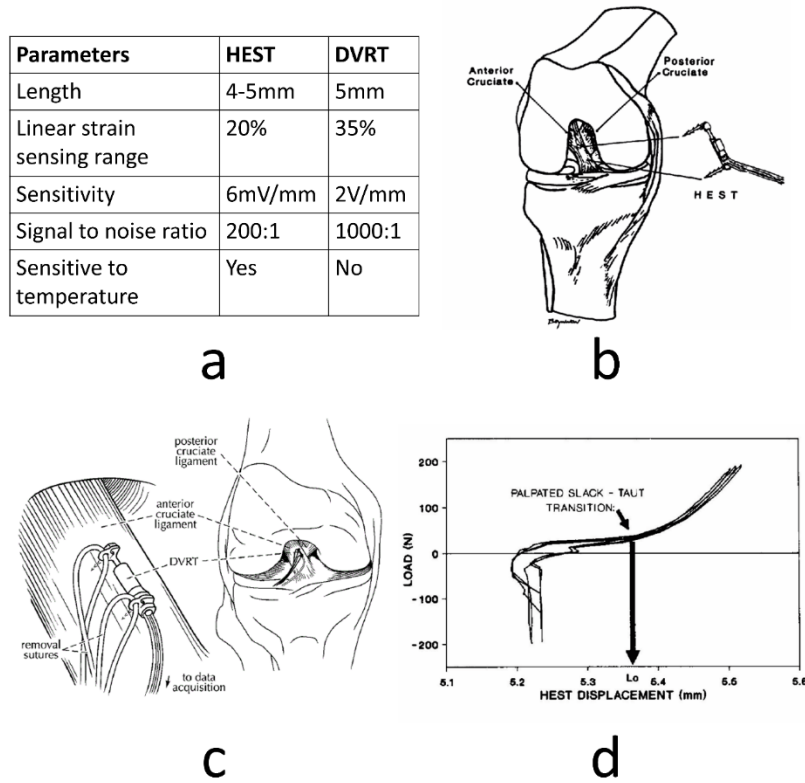


Fig. 1. HEST implantation and reference length identification. (a) Parameters of HEST and DVRT sensors. (b) Scheme showing a HEST sensor mounted onto the anteromedial bundle of the ACL with two fixation barb. (c) Scheme of DVRT sensor fixation. (d) Plot of tibia shear loads against HEST displacement, ACL reference length is defined as the HEST length at the slack-taut transition point. (Included figures are adapted from [59-61])

To assess *in-vivo* ACL slack length, Beynnon and co-workers recorded the displacement of a HEST sensor fixed on the ACL while applying antero-posterior shear loads to the tibia [48, 61]. They found an “inflection point” on the plot of the sensor length against shear load (Fig. 1d), corresponding to the length where the ACL engages. The corresponding sensor length at this point was considered to be the reference length used to calculate strain. Hence, any subsequent relative change of the sensor displacement from this length was considered to directly reflect loading within the ACL [48, 62]. This method was later validated by Fleming and co-workers through concurrently implementing a force probe to measure ACL load on cadaveric knees [63].

2.3.3. Key findings

In-vivo strain sensor measurements have provided critical insights into rehabilitation protocols for ACL reconstruction by providing direct evidence for activity selection that ensure tissue strains are under damaging magnitudes [26], but high enough to facilitate healing [64]. Specifically, squatting was long thought to be a safe activity for early rehabilitation of ACL reconstruction. However, *in-vivo* ACL strain

measurements using DVRT sensors have revealed that peak strains induced by squatting (3.6%) [25] are higher than lunges (1.8-2.0%), sit-to-stand (2.8%), step-up/down (2.5-2.6%) [26], and cycling activities (1.7%) [60]. These findings indicate that squatting exposes the ACL to greater loads than open-chain movements [34] and should therefore be used cautiously during rehabilitation. *In-vivo* sensor measurements have also revealed key insights into the role of muscle activation in both loading and protecting the ACL. The measurements indicate that isometric quadriceps contractions increase ACL strain at flexion angles of less than 50° [48, 62, 65], isometric gastrocnemius contractions increase ACL strain over all tested flexion angles, and that hamstrings contraction reduce ACL strain at flexion angles greater than 5° [34, 66]. These measurements have provided fundamental knowledge that can inform targeted muscle strengthening and neuromuscular coordination training to protect the ACL.

2.3.4. Advantages and limitations

There are several unique advantages to the HEST and DVRT implantable sensor approaches for strain measurement. Firstly, it provides a direct strain measurement and thus the data is highly representative of the local tissue strain environments. Secondly, both HESTs and DVRTs are highly sensitive and able to detect minute strains in the musculoskeletal tissues [34]. Finally, sensors provide high sampling frequencies for strain and strain rate measurements during dynamic activities.

Despite the insightful findings, however, the HEST and DVRT sensors have several major limitations:

- 1) Invasive nature: Sensor implantation is a highly invasive procedure, resulting in ethical difficulties to justify their use in healthy subjects. For ACL strain measurements, implantations have therefore typically been undertaken together with a pre-planned arthroscopic surgery to perform minor repairs of neighbouring tissues [48]. Consequently, such patients may have deformities or injuries that may alter the tibiofemoral contact mechanics [67] and potentially alter the measured soft tissue strain patterns [68, 69].
- 2) Tissue impingement: Current sensors can only be implanted in locations where there is sufficient room for the sensor and straight-forward surgical access to the tissue. For example, the strain sensors have always been attached to the anteromedial bundle of the ACL because it is more accessible from the anterolateral surgical portal than the posterolateral bundle of the ACL. While HEST and DVRT sensors are small in size, their solid constitution can result in impingement with surrounding musculoskeletal tissues, and therefore impede certain postures during testing. Importantly, sensor disturbance with the femoral notch is unavoidable at full extension of the knee during ACL strain measurements [35], which hinders the assessment of ACL strain patterns throughout activities involving full extension or even hyperextension of the knee [35].

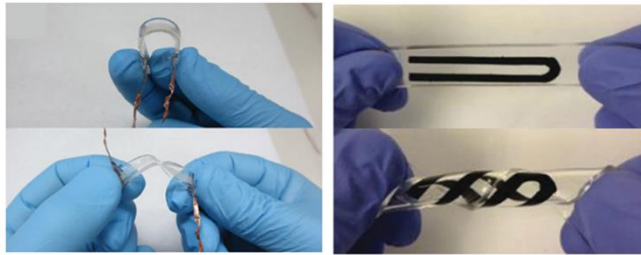
- 3) Limited implantation duration: Previous experiments have been limited to a few hours because both HEST and DVRT sensors require a cable that crosses the skin to transmit the measurement signal, and are therefore not long-term biocompatible. These limitations have prevented subjects from performing many functional activities of daily living.
- 4) Sensor-body interference: Sensor cable migration induced by subject body movement can cause significant artefacts in the sensor signal. Sensor cables should be stabilized and well protected during experiments.
- 5) Sensor implantation alignment: Measurements are sensitive to implantation orientation of the sensor relative to the tissue. To assess tensile ligament strains, the measurement axis of the sensor must be aligned with the ligament fibres during implantation in order to record uniaxial strain.

2.3.5. Future work

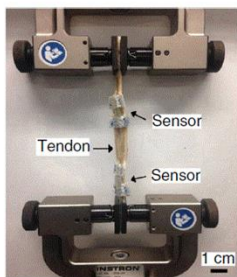
Recent advances in stretchable electronics may enable clinical translation of strain sensors towards intraoperative guidance and long-term assessment of healing. To facilitate these clinical applications and minimize risk to research subjects, these next generation strain sensors should incorporate three critical features: flexibility, wireless data transmission, and long-term biocompatibility. Thin and soft membrane-like strain sensors can be fabricated by embedding conductive materials in stretchable materials to reduce the risk of tissue impingement [70]. Initial measurements include skin surface assessments of joint rotation [71] and muscle movement of the trachea [72], as well as *ex-vivo* strains in the anterolateral ligament of a cadaveric knee (Fig. 2) [73]. Flexible electronic sensors can be fabricated using biocompatible materials (PDMS, gold, titanium, etc.), and several have demonstrated good biocompatibility through histologic examination [74, 75]. Wireless signal transmission with a passive sensor (i.e. no battery or chips) can be achieved using radio-frequency identification technology [76], enabling a resonant strain sensor containing a stretchable capacitor and a coil inductor whose resonance frequency can be wirelessly measured by a readout system to be developed (Fig. 2) [77]. However, improvement of sensor fixation [48, 78], as well as long-term stability and quality of flexible sensor signals are still necessary for clinical application. The development of biodegradable strain sensors that are resorbed after a given duration is critical to avoid a second surgery for sensor removal [79]. Such sensors would be ideal for clinical translation into soft tissue repair surgeries, especially for long-term assessment of tissue healing and data driven physical therapy.

Implantable Strain Sensor

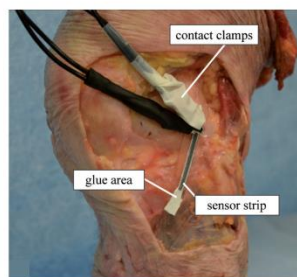
(a) Stretchable Strain Sensors



(b) Validation



(c) In Vitro Test



(d) In Vivo Application

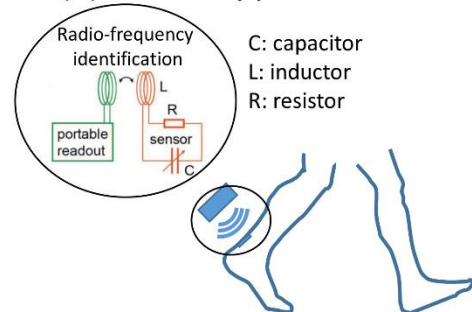


Fig. 2. Innovative stretchable strain sensors show great potential for quantifying in-vivo musculoskeletal soft tissue strains. (a) Stretchable strain sensors based on soft elastomers and nanomaterials could minimize the risk of interfering with neighbouring tissues. (b) Stretchable sensors have demonstrated high accuracy in measuring tendon strains during uniaxial tensile loading. (c) Stretchable strain sensors have been attached to the anterolateral ligaments using glue to measure ligament strains during knee joint manipulation. (d) In-vivo wireless measurements using stretchable sensors are possible using radio-frequency identification technology. Here, the passive sensor works as a LCR circuit whose resonance frequency varies with strain and can be readout using inductive coupling. (Included figures are adapted from [70, 73, 79])

2.4. Virtual Fibre Elongation

Initial imaging assessments of ligament strain were achieved using open-MRI [41, 80] and CT scans [81-84] to measure ligament length on the 2D slice images that best displayed the structure. However, substantial inaccuracies were clearly present in such 2D measurements due to out-of-plane errors. The virtual fibre elongation method overcomes this limitation by leveraging imaging data to reconstruct the relative 3D poses of the bones to determine the relative displacements of soft tissue attachment sites to non-invasively quantify tendon and ligament length change patterns [85-87]. For investigating dynamic activities, fluoroscopy is the state-of-art imaging modality, as CT and MRI are limited by their long-capture times and small field of view (FOV). Thus, the following discussion will primarily review fluoroscopic imaging studies [17].

2.4.1. Measurement technology and experimental methods

Typically, the joint of interest is statically imaged using MR [88] or CT [43], then segmentation is performed to construct 3D surface models of the bones. The attachment footprints of the ligament bundles are identified on the bone models from the images (MR) or relative to landmarks (CT). Subsequently, the subject performs a functional movement while the joint is imaged using single or dual-plane fluoroscopes [43, 89] to acquire a time series of radiographic images of the bones. The 3D bone poses are calculated to match to the images using a manual or (semi-)automated 2D-3D registration software [90-92]. This process is repeated for each radiographic image to quantify the joint kinematics throughout the movement (Fig. 3).

Virtual Fibre Elongation

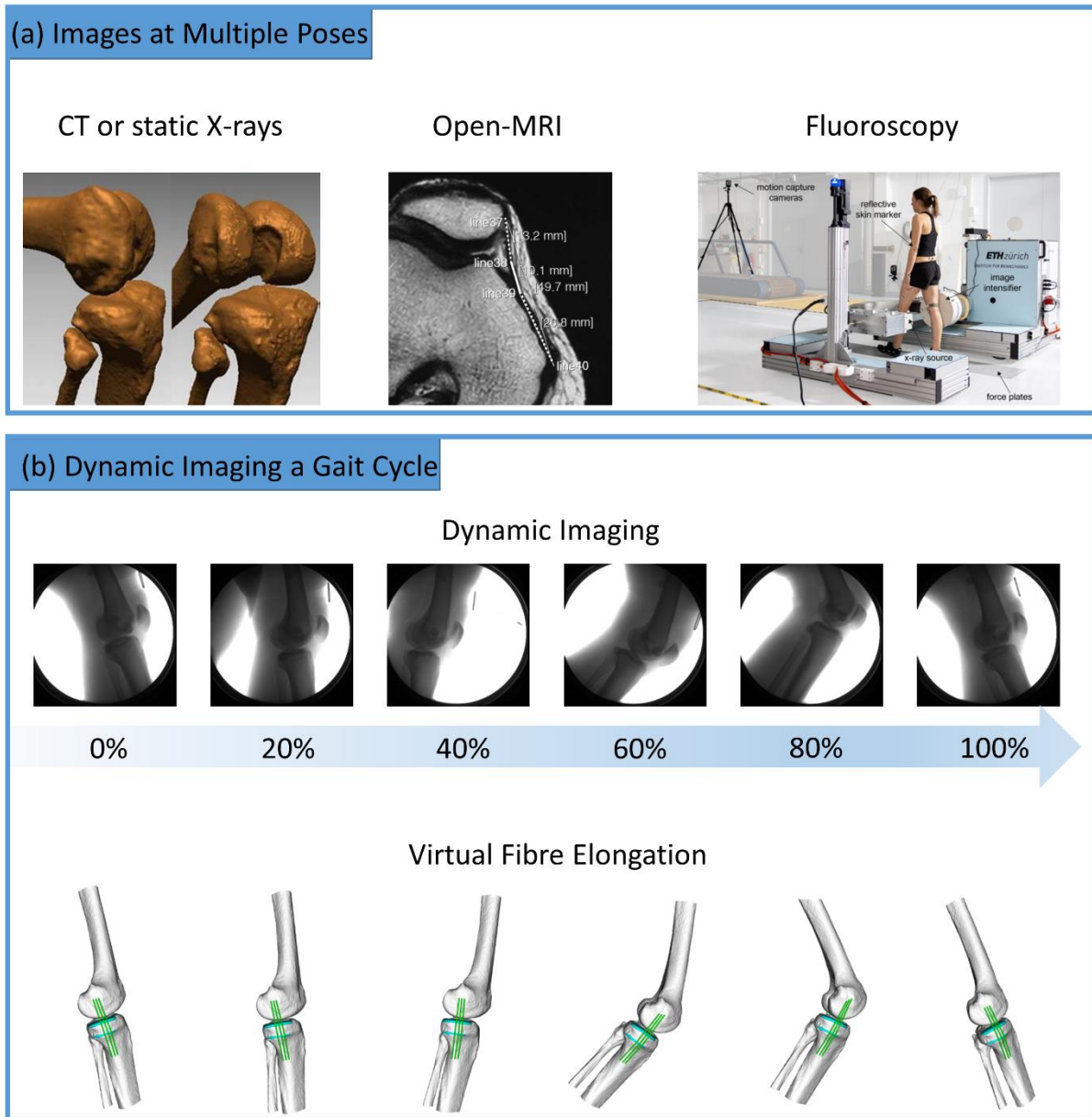


Fig. 3. Different virtual fibre elongation methods to quantify in-vivo soft tissue strains. (a) Static imaging at multiple poses or dynamic imaging throughout a movement. (b) In this example, dynamic video fluoroscopy is used to measure superficial medial collateral ligament (sMCL) strains during walking. The fluoroscope can move vertically, and the whole system is fixed on a frame that can slide along the rail. A time series of radiographic images of the knee joint are taken. The bone models are matched to the joint postures in each image to quantify the joint kinematics during the gait cycle. sMCL virtual fibres that connect the femoral and tibial attachment sites and wrap the bone surfaces are created. The lengths of the fibres are measured to characterize the long change patterns of the sMCL. (Included figures are adapted from [41, 83])

The length change of a ligament during a movement is assessed by tracking the relative displacements of the attachment points. For ligaments with small attachment footprints, a virtual fibre connecting the centroids of ligament insertion sites is defined as the ligament “longitudinal axis” [93].

For larger attachments, multiple virtual fibres can be defined [94, 95]. The fibre path can either be defined as the straight line connection between attachment points [94], or wrapping surfaces can be defined to represent the real curvilinear path of the ligament and prevent penetration of the bone geometries [49]. The length of the virtual fibre at each joint pose is compared to quantify the relative length change throughout the activity. As the virtual fibre is a geometric path, the orientation of the ligament force can also be quantified as the angle between the projection of the virtual fibre in each plane and the relevant axes in the predefined coordinate system of the joint [38, 96]. This enables insights into ligament function such as the restraint it can provide against external loads and graft bending in ligament reconstruction [97, 98].

2.4.2. Slack length

The virtual fibre elongation method does not provide any inherent means to determine the slack length of a tissue. Accordingly, most studies using this method define the reference length as the length of a tissue in a reference joint posture, to normalize length change measurements and provide an estimate of the elongation patterns. For the knee ligaments, the length at full knee extension [39, 49] or heel strike of walking [54] is commonly used as the reference length.

2.4.3. Key findings

The primary advantage of the virtual fibre elongation method is that it enables the non-invasive assessment of multiple ligaments in a joint during dynamic movements. The resulting comprehensive understanding of ligament contributions to functional joint mechanics has informed many surgical and rehabilitative sports medicine procedures. Using the virtual fibre elongation method, ACL length was shown to decrease by 28% from full knee extension to 135° of knee flexion during single leg lunge [37], while PCL length increases by 35% [94]. Ankle plantarflexion and supination were found to increase the length of the anterior talofibular ligament but decrease the length of the calcaneofibular ligament [99]. Studying different ligaments in the same joint can also reveal how the ligaments interact during an activity. A comparison of intact and ACL-deficient knees confirmed the importance of the ACL to knee stability by showing that ACL injury caused significant MCL extension and LCL shortening during lunges [100].

The virtual fibre elongation method also provides insights into the strain distribution within tissues by using multiple fibres. This technique has revealed that the anterior, middle, and posterior bundles of the superficial MCL exhibit different length change patterns (19%, 0%, and -16%) from full knee extension to 145° knee flexion during lunges [49]. Similarly, the length of the anterior and posterior bundles of the LCL exhibited a 6-7% increase and a 10-16% decrease, respectively [49, 101]. Running induced significantly greater elongation of the ACL anteromedial bundle compared to the posterolateral bundle [102], whereas walking showed more uniform elongation within the ACL [38]. This approach also revealed that reconstructing the medial patellofemoral ligament (MPFL) to a location posterior and

proximal to its anatomic femoral attachment results in the most isometric graft behaviour during lunging [103]. Similarly, at the shoulder, virtual fibre elongation techniques have allowed an insight into otherwise difficult to access dynamic musculoskeletal interactions. Maximal external rotation at 90° abduction significantly elongates the anterior bundle of the inferior glenohumeral ligaments while only slightly elongating the posterior bundle. Conversely, maximum internal shoulder rotation at 90° abduction significantly elongates the posterior bundle while only slightly elongating the anterior bundle [104]. Thus, the virtual fibre elongation method can reveal different function within regions of a single ligament, and consequently inform surgical reconstruction techniques and selective ligament release in joint revision surgery.

Virtual Fibre Elongation

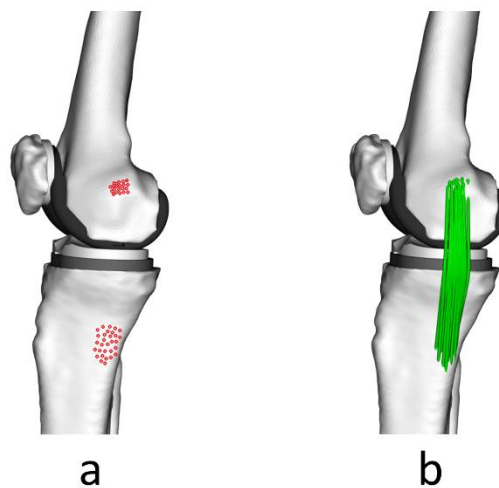


Fig. 4. Strain measurements of the virtual fibres throughout dynamic activities enables the identification of sMCL isometric locations in the femoral and tibial attachment areas. a) 32 femoral and tibial attachments on knee model of a TKA patient. b) sMCL virtual fibres from different combinations of femoral and tibial attachments.

The virtual fibre elongation method can also evaluate the outcomes of surgical procedures via the length change patterns of ligaments or grafts during functional movements. A possible mechanism for poor outcomes in PCL-retaining total knee arthroplasty (TKA) patients was identified because PCL elongation showed a significant increase compared to healthy knees at flexion angles of over 75° during lunges [105]. Cruciate-retaining TKA was also found to have a significant effect (mostly increasing) on the elongation patterns of the knee collateral ligaments during lunging by comparing the results of cruciate sacrificing TKA and healthy knees [49, 106]. A new study investigated the effect of knee TKA with ultra-congruent implants on the length change patterns of MCL and LCL during a variety of daily functional movements such as walking and squatting [107]. In the TKA knees, while the LCL consistently slackened with increased knee flexion in all movements, the MCL showed regional variation in the length changes. The anterior, middle, posterior MCL fibres lengthened, remained isometric, and shortened during knee flexions, respectively. This confirmed the previous observed

distinct regional behaviour of the MCL [49, 54] and indicated that the location of partial MCL releases performed intraoperatively to balance the knee will have important consequences on post-operative stability. For ACL reconstruction, anatomic ACL graft placement better restores the length and length change patterns of the native ACL compared to an anteroproximal graft placement [108]. A similar study found that compared to non-anatomic ACL reconstructions, anatomic ACL reconstruction results in PCL length change patterns (both bundles) that are closer to native patterns [43]. Therefore, the virtual elongation method provides a unique opportunity to non-invasively evaluate native and graft soft tissue strains, hence enabling quantitative evaluation of surgical techniques.

2.4.4. Advantages and limitations

The virtual fibre elongation method leverages state-of-the-art dynamic imaging technologies to non-invasively evaluate soft tissue strains throughout functional activities at high frequencies (> 200 Hz). It can quantify regional tissue strains by using multiple fibres to represent the same ligament (Fig. 4). Furthermore, as the fibre attachment locations are manually selected, uncertainty quantification and sensitivity studies can be readily performed [107]. Additionally, the measurement accuracy is not affected by whether the tissue is deep or superficial. Finally, the non-invasive nature of the method allows comparisons of injured or reconstructed tissue function against the healthy contralateral limb.

Despite the many advantages of the virtual elongation method, there are also several limitations:

- 1) Accuracy: Representing complex 3D tissue geometries with virtual fibre paths introduces several sources of error. Significant uncertainty in reported ligament lengths originates from both the identification of the tissue attachment footprints and virtual fibre insertion sites within the footprint [103]. The determination of ligament insertion sites on MR images can show large variations especially in some ligaments like the sMCL, which has large attachment areas (nearly 400 mm² on its tibial proximal attachment) [109]. However, for other ligaments such as the ACL, footprints can be accurately identified from MRI images [110]. The simplification of ligament pathways to straight virtual fibre paths also affects the accuracy, as it neglects any variations in pathway length due to wrapping around skeletal structures. Furthermore, virtual fibre ligament elongations are also sensitive to the measurement accuracy of the bone kinematics. With longer fluoroscope shuttering times (fluoroscopic exposure time per frame), the X-ray image becomes blurred, leading to errors in the accuracy of the 2D-3D registration. As an example, Ellingson and co-workers reported that the errors in knee joint kinematics could be as large as 2.0° and 1.6mm with an exposure time of 16ms [111], which would propagate into errors in the assessment of virtual fibre elongation patterns. Finally, virtual fibres only provide bone-to-bone elongation measurements, which makes them well suited for ligaments, but they cannot assess muscle fibre lengths and tendon lengths independently.

- 2) Difficult to determine slack length: The resting length of ligaments cannot be measured using fluoroscopy. Therefore, while relative elongation patterns can be reported, true tissue strain patterns or loading conditions cannot be quantified. To circumvent this issue, many researchers define the reference length of a structure to be its length at e.g., full knee extension [93], or at an instant of the gait cycle e.g. heel strike [112]. However, the lack of a consistent choice of reference length limits inter-study comparisons, and an appropriate solution should be agreed across the field.
- 3) Measurement frequency and radiation exposure: Fluoroscopes can generate either continuous [90] or pulsed [113] X-ray imaging. Continuous radiation modes enable higher measurement frequencies (speeds are then limited by the camera and fluoroscopic imaging formation), but also leads to greater radiation exposure to the subject, which constrains the measurement time and consequently the number of repetitions. Pulsed X-ray reduces the radiation dosage and therefore extends the measurement time. However, fluoroscopes with pulsed X-ray have limited measurement frequencies (often 25-30 Hz), which is insufficient to track highly dynamic movements such as impact situations.
- 4) Limited FOV: Traditional fluoroscopy systems are stationary with fields of view of 20-30 cm diameter. Thus, for many joints it is impossible to image complete activity cycles such as walking, running, or stair ascent/descent. Therefore, movements such as single legged lunge are often studied as the knee remains within the FOV [95, 103]. To track walking or running gait activities, the subject has to walk on a treadmill with only portions of the gait cycle such as stance phase being imaged [38, 54].

2.4.5. Future work

The virtual fibre elongation method has demonstrated great potential for assessing the function of ligaments in healthy [38, 39, 114] and surgically reconstructed states [43, 106, 115] in dynamic activities such as running [43] and landing [116]. However, the space constraints and stationary field of view of the imaging systems limit the movements that can be studied. Recently, mobile fluoroscopy systems have been developed to track the horizontal and vertical displacements of the joint during full body locomotion. Two of these systems have been developed to image lower limb joints throughout complete activity cycles [113, 117]. However, such systems may affect the subject's gait performance and introduce additional errors due to vibrations [118].

Currently, the virtual fibre elongation method is too time consuming for clinical translation due to the segmentation of the joint anatomy, definition of ligament attachment points, and 2D/3D images registration steps. Introducing artificial intelligence techniques to automate these processes could eliminate the time-consuming nature of this method, and therefore make it clinically viable. For example, a segmentation method combining image registration and machine learning has been developed to automatically segment the region of interest on ultrasound [119] and MRI images [120]. It could be

envisaged that such technology will help improve the automation of the virtual fibre elongation method. Moreover, instead of using virtual fibres to model the ligament, future study could develop the finite element model of the ligament and apply the joint kinematic data as boundary conditions to simulate the 3D strain-stress environment within the ligament [121]. Finally, roentgen stereophotogrammetric analysis (RSA) can extend the virtual fibre elongation method to enable tendon strain measurement, especially to evaluate the recovery of the mechanical properties and function of reconstructed tissues [122-125]. RSA requires that titanium beads are implanted in bones or soft tissues through open surgery [126] or injection [127], and then uses dynamic imaging to capture the distance between beads throughout an activity to quantify tissue length changes. Tashman and co-workers have developed a dynamic RSA system by combining X-ray radiographs and high-speed digital imaging to achieve high measurement frequency (250Hz) and accuracy ($\pm 0.1\text{mm}$) [128], which could be used in measuring dynamic activities. However, the invasive nature of bead implantation limits its application on human subjects.

2.5. Ultrasound

Ultrasound is a non-invasive, radiation-free, and cost-effective technique to visualise the internal architecture of musculoskeletal soft tissues. Clinically, ultrasound is commonly used to identify pathological tendon abnormalities [129]. In research settings, ultrasound has been leveraged to quantify muscle, tendon, and ligament deformation during dynamic activities. Numerous ultrasound studies quantified strains of large flat tendons such as the AT during walking [130, 131] and running [132, 133], however, very few ultrasound studies focused on ligaments [134]. Ultrasound also enables muscle fibre lengths and pennation angle to be dynamically assessed [27, 135].

Typical ultrasound systems consist of a hand-held transducer connected by flexible wire to a cart that houses the electronics for signal generation and processing, as well as a screen for visualization. The working principle behind ultrasound imaging relies on propagating ultrasonic waves (sound waves with frequencies $> 20'000$ Hz) into the tissue of interest and recording their reflection [136, 137]. The ultrasonic waves reflect off the tissue according to the local properties, and the echoes are recorded and used to generate an image. Traditional ultrasound systems generate planar 2D images and can reach tissues up to 17 cm beneath the skin [138]. Two primary techniques have been developed to measure soft tissue strain during dynamic movements using ultrasound, myotendinous junction (MJ) tracking (Fig. 5) and speckle tracking (Fig. 5). Freehand 3D ultrasound has also been applied to measure Achilles' tendon strain, but only by imaging multiple static postures, and thus this review focuses on MJ and speckle tracking techniques.

2.5.1. Measurement technology and experimental methods

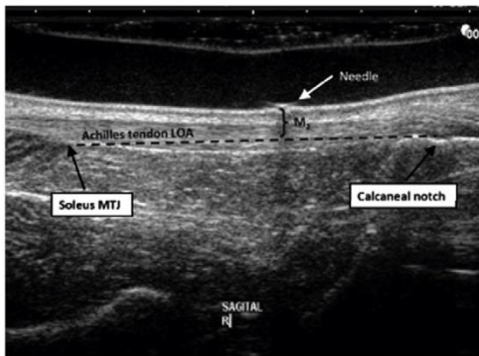
For both strain measurement techniques, the ultrasound transducers must be fixed to the body during dynamic movement to image a tissue. Typically, the ultrasound transducer is housed in a foam orthotic and strapped to the body using athletic tape [130]. In many experiments, a treadmill is used so that the ultrasound cart can remain stationary. Commonly, markers are attached to the transducer and the ultrasound system is synchronized with a motion analysis system so that the transformation between the image field of view and other anatomic landmarks can be calculated (Fig. 5).

The MJ tracking technique enables muscle and tendon lengths to be quantified by tracking anatomical landmarks in each ultrasound image of a series collected throughout an activity. For example, the elongation of the free AT can be measured by tracking the displacement between the calcaneus attachment and the soleus-AT myotendinous junction (sATMJ) [139]. An ultrasound transducer with a wide FOV (100mm) can image the entire free AT from the calcaneus to sATMJ [139] (Fig. 5). For many applications and ultrasound systems, however, the tissue length exceeds the transducer's FOV and thus only one attachment site can be tracked. Synchronizing the ultrasound system with an optic tracking system provides another means to track the length change of a long tendon during movement [140-142].

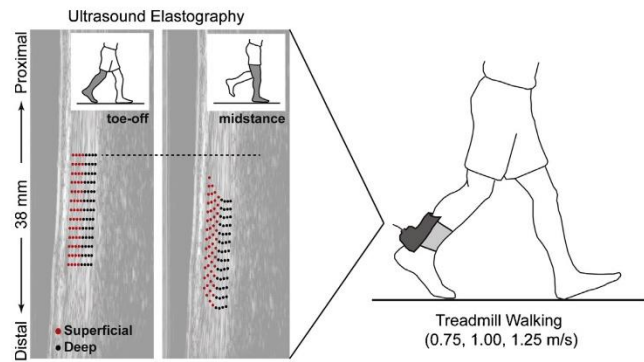
To measure the AT, a reflective marker is placed on the calcaneus attachment to track its position. An ultrasound transducer equipped with reflective markers is fixed on the shank to image the position of the sATMJ, and then transform it into the global coordinate system. The free AT length is then defined as the distance between the positions of the calcaneus and the sATMJ.

Ultrasound

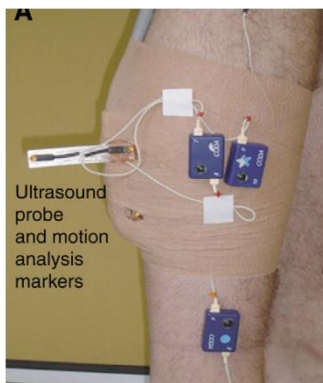
(a) Myotendinous Junction Tracking



(b) Speckle Tracking



(c) Motion Capture + Ultrasound



(d) Freehand Ultrasound Scanning

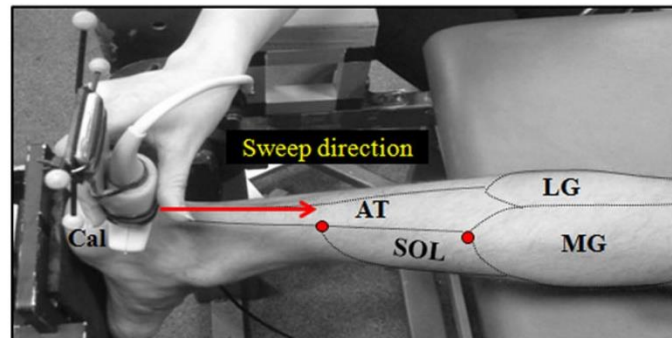


Fig. 5. A variety of ultrasound techniques to quantify muscle and tendon elongations. (a) Ultrasound transducer with a wide FOV (100 mm) can image the entire free Achilles' tendon (soleus to calcaneus). (b) The ultrasound elastography speckle tracking method enables the displacements of the superficial and deep AT tissues to be independently measured during walking. (c) By fixing motion capture markers to the ultrasound transducer, tissue displacements in the sATMJ can be tracked in the laboratory coordinate system to quantify AT length changes. (d) An ultrasound transducer with markers attached is manually swept along the AT to take a series of ultrasound images of the AT. The ultrasound images and transducer positions are merged to reconstruct 3D geometries of the AT at multiple poses. (Included figures are adapted from [45, 130, 139, 143])

Speckle tracking provides an alternative method to quantify regional tissue strain using ultrasound. A speckle is an interference pattern with bright and dark spots in B-mode or radiofrequency (RF) ultrasound images [144]. The speckle pattern remains constant when the tissue structure is static and thus is thought to be representative of the tissue structure rather than measurement noise. Therefore, when the tissue microstructure is deformed, the speckle pattern changes accordingly [145]. After the B-

mode or RF ultrasound images of the tendon are obtained throughout an activity, a region of interest (ROI) containing the tendon structure is manually selected on one image [146]. Then, automated speckle tracking algorithms are used to calculate the frame-to-frame speckle displacement within the ROI, which is then converted into tendon elongations [40, 130].

2.5.2. Slack length

Ultrasound provides two opportunities to assess the slack length of a tissue. Firstly, a tissue can be imaged at multiple joint postures until buckling can be identified in the B-mode images. This has been demonstrated on the patellar tendon [147, 148]. Secondly, a novel ultrasound imaging technique called shear wave elastography, which quantifies the speed of shear wave propagation in a tissue, has been applied to assess tissue slack length. Shear wave speed has been shown to be related to tissue stress [149, 150], and thus can be applied to establish when the tissue goes slack if a corresponding joint is manipulated through its range of motion. This technique has been applied to assess the slack length of the AT [50] and the ankle angle when the individual triceps surae muscles are slack [151].

2.5.3. Key findings

Ultrasound based strain measurements have provided many important insights into the dynamic function of the AT. For example, ultrasound was used to quantify *in-vivo* AT strains during dynamic activities such as running (3.5-5.8%), walking (4.6%), and one-legged hopping (8-8.3%) [45, 140, 141, 152]. These functional AT strain data provide some important implications for AT injury. Firstly, the *in-vivo* AT strains during one-legged hopping are surprisingly close to the AT failure strains found in *in-vitro* tendon tensile tests [141, 153]. As the AT remained healthy after hopping tests, this finding demonstrates the difficulty of comparing *in-vivo* and *in-vitro* strain measurements and perhaps inconsistency among the methods. Secondly, the *in-vivo* strain data from ultrasound measurements can serve as a variable to assess other parameters associated with AT injury, such as the mechanical “safe factor” [152] and “core temperature” [140] of the AT. Franz and co-workers measured the regional deformations of AT during walking [130], and showed that the aggregate AT exhibited nearly twice as much elongation as the free AT. Moreover, the superficial AT exhibited larger elongations than the deep AT and only the superficial AT elongation was found to increase at higher walking speeds, indicating non-uniform regional strain patterns in the AT. Cronin and co-workers compared the length changes of Achilles’ tendons during walking between healthy and diabetic subjects [154]. The length changes of Achilles’ tendons were smaller in diabetic subjects than healthy patients, but the length changes of muscle-tendon units were similar. These findings indicate that diabetes may decrease the elastic energy storage of Achilles’ tendons and increase muscle work, resulting in decreased walking efficiency. Finally, ultrasound has provided insights to AT healing and protection. For example, AT strain during running with a 18mm heel lift was significantly smaller than barefoot, suggesting that such a heel lift could help to reduce the AT strains during AT rehabilitation training [132].

Ultrasound evaluations have also contributed towards understanding the function of human triceps surae muscles during walking and running [27, 155-157]. In these studies, either a single ultrasound transducer was positioned over the medial gastrocnemius (MG) so that the soleus was also visible [156], or two transducers were placed over the MG and soleus [158]. The MG and soleus fascicle lengths and pennation angles were then measured using an automated tracking algorithm, and motion-capture derived knee and ankle joint kinematics were further used to estimate MG and soleus muscle-tendon unit lengths [156, 159, 160]. These studies found different length change patterns and magnitudes between the MG and soleus fascicles during the stance phase of gait, indicating the different functional roles of the two muscles [158]. Relevant studies have also determined the differences in triceps surae length changes and behaviour between walking and running [159, 161], between forefoot and rearfoot running [162], and at different running speeds [163]. Investigating the length change patterns in both muscle fascicle and muscle-tendon unit also showed a decreased energy storing role of the AT in race-walking compared to running [156]. The effect of age on gastrocnemius muscle-tendon behaviour during walking has also been studied by ultrasound [160], and it was found that tendon lengthening is greater and muscle fascicle lengthening is smaller in older subjects compared to young subjects. In addition, ultrasound has been used to characterize the effect body mass on gastrocnemius medialis fascicle behaviour during stair ascent [164]. By calculating the difference between the muscle tendon unit length change and the fascicle length change, it was found that additional body mass could cause substantially greater stretching on the tendon. This finding may be meaningful in evaluating effect of obesity on pathological loading in triceps surae muscle tendon unit.

The application of ultrasound to quantify ligament strain is limited to a few studies investigating superficial ligaments during static movements, such as the dorsal lisfranc ligament [165-167], pisohamate ligament and pisometacarpal ligament [168]. Using speckle-tracking, 5-7% strains were observed in the coracoacromial ligament during dynamic shoulder rotations such as forward flexion, horizontal abduction, and internal rotation at 90° abduction [40]. The strain patterns and displacements of the coracoacromial ligament indicated contact with the rotator cuff in these frequently used shoulder movements. This indicates a possible mechanism for rotator cuff pathologies, and provides guidelines for rehabilitation protocols as certain movements such as forward flexion, horizontal abduction, and internal rotation at 90° abduction were found to induce excessive tissue strains.

2.5.4. Advantages and limitations

Ultrasound provides several key advantages over other methods for assessing musculoskeletal soft tissue strain. Firstly, it is non-invasive, relatively inexpensive, and does not expose the subjects to radiation. Secondly, ultrasound can dynamically image soft tissues, which enables regional deformation within the tissue to be quantified. Finally, it enables the strains of muscle fibres and tendon to be independently measured as it can differentiate muscle-tendon interfaces.

Despite these advantages, ultrasound methods also suffer from several limitations:

- 1) **Controversial reliability:** Establishing good reliability of ultrasound tissue length measurement is fundamental to highly accurate measurements of tissue strain [129, 169]. However, the reliability of ultrasound measurement of static tissue geometry has been controversially reported [170-176], and these measurements are easier to perform than strain measurement during dynamic activities. Furthermore, transducer orientation and position have a significant effect on ultrasound measurements [177, 178], and rigid fixation of the ultrasound transducer over the tissue of interest is difficult to achieve throughout dynamic activities. Some confidence can be gained from the good intra-class correlation coefficient (ICC) of ultrasound in measuring AT strains (0.72-0.86) and coefficient of multiple correlation of measuring PT strains (0.77-0.82) [145, 174], but it should be noted that these studies only measured tendon strain during static movements.
- 2) **Challenging to measure ligament strains:** Ultrasound is mostly used clinically to diagnose ligament injuries [179-182], but rarely to measure ligament strains. This is largely due to the difficulty of obtaining clear images of complete ligament structures as they are normally small and located beneath neighbouring tissues. In addition, ligaments commonly are directly adjacent to bone and other hypoechoic tissues, which can lead to artefacts and reduced ligament visibility in ultrasound images. Furthermore, in traditional ultrasound images, the ligament appears hypoechoic at rest because of anisotropy artefacts and hyperechoic under loading due to tightening of the ligament microstructure [168, 183]. This change in appearance between loading conditions can help differentiate the ligament from other tissues but causes difficulties when trying to quantify ligament strain patterns throughout an entire movement.
- 3) **Confounded by out-of-plane motion:** The complexity of measuring the deformation of 3D soft tissues in planar 2D ultrasound images is another key limitation of ultrasound. MJ tracking and speckle tracking both require tracking landmarks or pixels in the 2D ultrasound image. Out-of-plane strains resulting from tissues bulging, rotating, or twisting may be missed or misinterpreted as in plane translation. Freehand 3D ultrasound addresses this limitation, but cannot be applied to dynamic movements because the transducer must be swept over the length of the tissue [184, 185].
- 4) **Transducer fixation over tissue:** For ultrasound measurement of dynamic activities, the transducer must be fixed over the tissue of interest as any motion of the transducer relative to the body can cause measurement error. This requires that the transducer is strapped to the body which may alter natural movement patterns. Finally, dynamic measurements are typically limited to a treadmill to avoid moving the ultrasound cart over-ground with the subject.

2.5.5. Future work

Ultrasound methods are currently the most clinically viable for assessing musculoskeletal soft tissue strains due to their non-invasive, non-radiative, and relatively low-cost nature. However, their 2D nature limits the accuracy and repeatability of this method. Freehand 3D ultrasound scanning has been developed to quantify the 3D AT deformation *in vivo* [143, 185], including changes in AT length, AT width, thickness, cross-sectional area, and volume [143, 186]. This technique relies on a conventional ultrasound machine coupled with a transducer instrumented with reflective markers and an optical tracking system. The operator performs transverse ultrasound scans from the calcaneus along the AT to the gastrocnemius muscle [184, 187], during which the spatial position and orientation of the ultrasound transducer are recorded. Then, the 2D ultrasound images (between-frame interval of 0.1-0.5 mm) are transformed into the global coordinate system to create a 3D AT reconstruction [188]. Highly precise 2D-to-3D transformation of the image (error under 1mm) can be achieved after temporal and spatial calibration of the ultrasound transducer [184, 188]. Measurements of 3D AT deformations then require a series of digital processing procedures such as segmenting and rendering AT cross-sections, reconstructing 3D AT volumes, and defining measurement sites [184]. The applicability of 3D freehand ultrasound to dynamic movements, however, remains to be established (Fig. 5).

2.6. Summary and Perspectives

In-vivo strain measurements have provided important insights into the mechanical function of musculoskeletal soft tissues, resulting in improved rehabilitative and surgical treatments in sports medicine. This review has presented three main state-of-the-art methodologies that enable quantification of soft tissue strain patterns during dynamic movements: implantable strain sensors, virtual fibre elongation, and ultrasound. Each methodology has provided key measurements that altered treatments and rehabilitation for musculoskeletal soft tissues. However, further innovations in the measurement technologies and their clinical implementation will be necessary to facilitate a data driven revolution to personalize sports medicine treatments.

Each strain measurement technique has its own virtues and limitations in terms of safety, application, and accuracy (Table 1). Implantable sensors enable strains in deep tissues to be measured with high accuracy and frequency. However, the sensor designs that have been implanted in humans are highly invasive, can impinge on neighbouring tissues, limit the movements that can be performed, and require a data transmission wire to cross the skin. The virtual fibre elongation method enables elongation measurements of multiple deep and superficial tissues during highly dynamic movements. However, it can expose the subjects to radiation depending on the imaging method, and can only quantify bone-to-bone tissue length changes and thus cannot differentiate between muscle and tendon strain. Ultrasound methods provide unique advantages because they are non-invasive, do not expose subjects to radiation, and provide direct imaging of the soft tissue structures. Ultrasound also provides the unique possibility to measure regional tissue strains compared to implantable sensors and the virtual fibre elongation methods which can only assess point-to-point strains. However, dynamic ultrasound has limited accuracy due to out-of-plane motion, and is largely only applicable to measure superficial muscles and tendons. Thus, researchers and clinicians must carefully consider the advantages and limitations of each measurement technique when planning new studies and interpreting results.

Assessment of soft tissue slack length remains significantly challenging for each strain measurement technique. The inflection point method has been well validated for determining ACL slack length with implantable strain sensors, but it is uncertain whether similar experiments can be replicated on other soft tissues. The virtual fibre method currently has no reported method for measuring slack length, but potentially could be coupled with ultrasound. Ultrasound can provide measurements of slack length through visualizing tissue buckling or using shear wave propagation [189], but these may not be applicable to all tissues. Future studies should at the very least report the method used to determine the reference length and provide quantitative values of the tissue lengths.

A key limitation of this study is that it only focused on measurement techniques that have been applied to measure *in-vivo* human musculoskeletal soft tissue strains during functional movements. However, several techniques have been used to measure *in-vivo* strains in animal tissue

(sonomicrometry [190], liquid metal strain gauges [55]), *in-vivo* strains in human bone [191], and *in-vivo* loading in human tendons (fibre optic sensors [58], buckle transducers [57], shear wave tensiometers [149]). Furthermore, novel techniques such as near infrared spectroscopy [192] show promise to quantify musculoskeletal soft tissue mechanical properties. The working principles behind any of these techniques may lead to the needed breakthrough that overcomes the limitations of current strain measurement methods.

In conclusion, we have found *in-vivo* strain measurements have improved clinical treatments for many musculoskeletal pathologies including ACL reconstruction, AT repair, and TKA. However, a new generation of clinically viable technologies are needed to facilitate a data driven progression of personalized surgical and rehabilitative sports medicine treatments.

Table 1. Functional characteristics of each strain measurement method

Measurement method	Measurement mode	Radiation	Accessibility	Measurement area	Dynamic activities measured	Clinical application
Strain sensor	Invasive	No	ACL	Anteromedial bundle Regional strain	<ul style="list-style-type: none"> • Squat • Bicycle • Step up/down* • lunge 	<ul style="list-style-type: none"> • Intraoperative function assessment of ACL graft • Long-term follow-up function change of ACL graft
Virtual fibre elongation (with fluoroscope)	Non-invasive	Yes	Knee joint: - ACL - PCL - LCL - MCL - MPFL Ankle joint: - ATFL - CFL Shoulder joint: - glenohumeral	Multiple bundles Overall strain	<ul style="list-style-type: none"> ○ Walk ○ Run ○ Hop ○ Jump land ○ Step up ○ Lunge 	<ul style="list-style-type: none"> ○ Function assessment of knee ligaments after total knee arthroplasty ○ Identification of tunnel placement effect on graft function
Ultrasound	Non-invasive	No	AT PT Limited superficial ligaments	3D Regional & overall strain	<ul style="list-style-type: none"> ▪ Walk ▪ Run ▪ Hop 	<ul style="list-style-type: none"> ▪ Investigation of tendinopathy effect on tendon mechanical properties ▪ Investigation of tendon adaptation to rehabilitation therapy

* including similar movements such as standing up from sitting posture.

2.7. References

1. Agres, A.N., et al., *Increased unilateral tendon stiffness and its effect on gait 2-6 years after Achilles tendon rupture*. Scand J Med Sci Sports, 2015. **25**(6): p. 860-7.
2. Huston, L.J., M.L. Greenfield, and E.M. Wojtys, *Anterior cruciate ligament injuries in the female athlete. Potential risk factors*. Clin Orthop Relat Res, 2000(372): p. 50-63.
3. Lyman, S., et al., *Epidemiology of anterior cruciate ligament reconstruction: trends, readmissions, and subsequent knee surgery*. J Bone Joint Surg Am, 2009. **91**(10): p. 2321-8.
4. Escamilla, R.F., et al., *Anterior cruciate ligament strain and tensile forces for weight-bearing and non-weight-bearing exercises: a guide to exercise selection*. J Orthop Sports Phys Ther, 2012. **42**(3): p. 208-20.
5. Nagda, S.H., et al., *Cost analysis of outpatient anterior cruciate ligament reconstruction: autograft versus allograft*. Clin Orthop Relat Res, 2010. **468**(5): p. 1418-22.
6. Griffin, L.Y., et al., *Noncontact anterior cruciate ligament injuries: risk factors and prevention strategies*. J Am Acad Orthop Surg, 2000. **8**(3): p. 141-50.
7. Westin, O., et al., *Cost-effectiveness analysis of surgical versus non-surgical management of acute Achilles tendon ruptures*. Knee Surg Sports Traumatol Arthrosc, 2018. **26**(10): p. 3074-3082.
8. Karnovsky, S.C. and M.C. Drakos, *Revision Achilles Reconstruction with Hamstring Autograft and FHL Tendon Transfer in an Athlete*. HSS J, 2017. **13**(3): p. 302-306.
9. Ochen, Y., et al., *Operative treatment versus nonoperative treatment of Achilles tendon ruptures: systematic review and meta-analysis*. BMJ, 2019. **364**: p. k5120.
10. Nagaraj, R. and M.N. Kumar, *Revision Anterior Cruciate Ligament Reconstruction in the Nonathlete Population*. Indian J Orthop, 2019. **53**(1): p. 154-159.
11. Webster, K.E., et al., *Revision Anterior Cruciate Ligament Reconstruction Outcomes in Younger Patients: Medial Meniscal Pathology and High Rates of Return to Sport Are Associated With Third ACL Injuries*. Am J Sports Med, 2018. **46**(5): p. 1137-1142.
12. Wertheim, M.G., *Memoire sur l'elasticité et la cohésion des principaux tissus du corps humain*. Ann Chimie Phys Paris (Ser. 3) 1847. **21**: p. 385-414.
13. Fung, Y.-c., *Biomechanics: mechanical properties of living tissues*. 2013: Springer Science & Business Media.
14. Noyes, F.R., J.L. DeLucas, and P.J. Torvik, *Biomechanics of anterior cruciate ligament failure: an analysis of strain-rate sensitivity and mechanisms of failure in primates*. J Bone Joint Surg Am, 1974. **56**(2): p. 236-53.
15. Haut, R.C., *Age-dependent influence of strain rate on the tensile failure of rat-tail tendon*. J Biomech Eng, 1983. **105**(3): p. 296-9.
16. Friden, J. and R.L. Lieber, *Structural and mechanical basis of exercise-induced muscle injury*. Med Sci Sports Exerc, 1992. **24**(5): p. 521-30.
17. Hosseini Nasab, S.H., et al., *Loading Patterns of the Posterior Cruciate Ligament in the Healthy Knee: A Systematic Review*. PLoS One, 2016. **11**(11): p. e0167106.
18. Kittl, C., et al., *The Role of the Anterolateral Structures and the ACL in Controlling Laxity of the Intact and ACL-Deficient Knee*. Am J Sports Med, 2016. **44**(2): p. 345-54.
19. Zavras, T.D., et al., *A comparative study of 'isometric' points for anterior cruciate ligament graft attachment*. Knee Surgery Sports Traumatology Arthroscopy, 2001. **9**(1): p. 28-33.
20. Amis, A.A. and T.D. Zavras, *Isometricity and graft placement during anterior cruciate ligament reconstruction*. The Knee, 1995. **2**(1): p. 5-17.
21. Camp, C.L., et al., *Timing of Postoperative Mechanical Loading Affects Healing Following Anterior Cruciate Ligament Reconstruction: Analysis in a Murine Model*. J Bone Joint Surg Am, 2017. **99**(16): p. 1382-1391.

22. Brophy, R.H., et al., *Effect of short-duration low-magnitude cyclic loading versus immobilization on tendon-bone healing after ACL reconstruction in a rat model*. J Bone Joint Surg Am, 2011. **93**(4): p. 381-93.
23. Woo, S.L., et al., *Biomechanics and anterior cruciate ligament reconstruction*. J Orthop Surg Res, 2006. **1**: p. 2.
24. Rayan, F., et al., *Review of evolution of tunnel position in anterior cruciate ligament reconstruction*. World J Orthop, 2015. **6**(2): p. 252-62.
25. Beynnon, B.D., et al., *The strain behavior of the anterior cruciate ligament during squatting and active flexion-extension. A comparison of an open and a closed kinetic chain exercise*. Am J Sports Med, 1997. **25**(6): p. 823-9.
26. Heijne, A., et al., *Strain on the anterior cruciate ligament during closed kinetic chain exercises*. Med Sci Sports Exerc, 2004. **36**(6): p. 935-41.
27. Cronin, N.J. and G. Lichtwark, *The use of ultrasound to study muscle-tendon function in human posture and locomotion*. Gait Posture, 2013. **37**(3): p. 305-12.
28. Mian, O.S., et al., *Gastrocnemius muscle-tendon behaviour during walking in young and older adults*. Acta Physiol (Oxf), 2007. **189**(1): p. 57-65.
29. af Klint, R., et al., *Afferent contribution to locomotor muscle activity during unconstrained overground human walking: an analysis of triceps surae muscle fascicles*. J Neurophysiol, 2010. **103**(3): p. 1262-74.
30. Roberts, T.J. and E. Azizi, *Flexible mechanisms: the diverse roles of biological springs in vertebrate movement*. J Exp Biol, 2011. **214**(Pt 3): p. 353-61.
31. Zelik, K.E. and J.R. Franz, *It's positive to be negative: Achilles tendon work loops during human locomotion*. PLoS One, 2017. **12**(7): p. e0179976.
32. Herzog, W., *Muscle properties and coordination during voluntary movement*. J Sports Sci, 2000. **18**(3): p. 141-52.
33. Prilutsky, B.I. and V.M. Zatsiorsky, *Optimization-based models of muscle coordination*. Exerc Sport Sci Rev, 2002. **30**(1): p. 32-8.
34. Beynnon, B.D. and B.C. Fleming, *Anterior cruciate ligament strain in-vivo: a review of previous work*. J Biomech, 1998. **31**(6): p. 519-25.
35. Fleming, B.C. and B.D. Beynnon, *In vivo measurement of ligament/tendon strains and forces: a review*. Ann Biomed Eng, 2004. **32**(3): p. 318-28.
36. Ravary, B., et al., *Strain and force transducers used in human and veterinary tendon and ligament biomechanical studies*. Clin Biomech (Bristol, Avon), 2004. **19**(5): p. 433-47.
37. Jordan, S.S., et al., *The in vivo kinematics of the anteromedial and posterolateral bundles of the anterior cruciate ligament during weightbearing knee flexion*. Am J Sports Med, 2007. **35**(4): p. 547-54.
38. Wu, J.L., et al., *Kinematics of the anterior cruciate ligament during gait*. Am J Sports Med, 2010. **38**(7): p. 1475-82.
39. Taylor, K.A., et al., *In vivo measurement of ACL length and relative strain during walking*. J Biomech, 2013. **46**(3): p. 478-83.
40. Park, I., et al., *Which shoulder motions cause subacromial impingement? Evaluating the vertical displacement and peak strain of the coracoacromial ligament by ultrasound speckle tracking imaging*. J Shoulder Elbow Surg, 2015. **24**(11): p. 1801-8.
41. Higuchi, T., et al., *An analysis of the medial patellofemoral ligament length change pattern using open-MRI*. Knee Surg Sports Traumatol Arthrosc, 2010. **18**(11): p. 1470-5.
42. King, A.J., et al., *In vivo open-bore MRI reveals region- and sub-arc-specific lengthening of the unloaded human posterior cruciate ligament*. PLoS One, 2012. **7**(11): p. e48714.
43. Tang, J., et al., *In vivo posterior cruciate ligament elongation in running activity after anatomic and non-anatomic anterior cruciate ligament reconstruction*. Knee Surg Sports Traumatol Arthrosc, 2016.

44. Halilaj, E., et al., *In vivo recruitment patterns in the anterior oblique and dorsoradial ligaments of the first carpometacarpal joint*. J Biomech, 2015. **48**(10): p. 1893-8.
45. Lichtwark, G.A. and A.M. Wilson, *Interactions between the human gastrocnemius muscle and the Achilles tendon during incline, level and decline locomotion*. J Exp Biol, 2006. **209**(Pt 21): p. 4379-88.
46. Stenroth, L., D. Thelen, and J. Franz, *Biplanar ultrasound investigation of in vivo Achilles tendon displacement non-uniformity*. Transl Sports Med, 2019. **2**(2): p. 73-81.
47. Nuri, L., et al., *The tendinopathic Achilles tendon does not remain iso-volumetric upon repeated loading: insights from 3D ultrasound*. J Exp Biol, 2017. **220**(Pt 17): p. 3053-3061.
48. Beynnon, B., et al., *The measurement of anterior cruciate ligament strain in vivo*. Int Orthop, 1992. **16**(1): p. 1-12.
49. Hosseini, A., et al., *In vivo length change patterns of the medial and lateral collateral ligaments along the flexion path of the knee*. Knee Surgery Sports Traumatology Arthroscopy, 2015. **23**(10): p. 3055-3061.
50. Hug, F., et al., *Slack length of gastrocnemius medialis and Achilles tendon occurs at different ankle angles*. Journal of Biomechanics, 2013. **46**(14): p. 2534-2538.
51. Hosseini Nasab, S.H., et al., *Elongation Patterns of the Posterior Cruciate Ligament after Total Knee Arthroplasty*. J Clin Med, 2020. **9**(7).
52. Roriz, P., et al., *From conventional sensors to fibre optic sensors for strain and force measurements in biomechanics applications: a review*. J Biomech, 2014. **47**(6): p. 1251-61.
53. Bey, M.J. and K.A. Derwin, *Measurement of in vivo tendon function*. J Shoulder Elbow Surg, 2012. **21**(2): p. 149-57.
54. Liu, F., et al., *In vivo length patterns of the medial collateral ligament during the stance phase of gait*. Knee Surg Sports Traumatol Arthrosc, 2011. **19**(5): p. 719-27.
55. Brown, T.D., et al., *Dynamic performance characteristics of the liquid metal strain gage*. J Biomech, 1986. **19**(2): p. 165-73.
56. Jansen, M.O., et al., *Mechanical properties of the tendinous equine interosseus muscle are affected by in vivo transducer implantation*. J Biomech, 1998. **31**(5): p. 485-90.
57. Fukashiro, S., et al., *In vivo Achilles tendon loading during jumping in humans*. Eur J Appl Physiol Occup Physiol, 1995. **71**(5): p. 453-8.
58. Finni, T., P.V. Komi, and J. Lukkariniemi, *Achilles tendon loading during walking: application of a novel optic fiber technique*. Eur J Appl Physiol Occup Physiol, 1998. **77**(3): p. 289-91.
59. Beynnon, B.D., et al., *The effect of functional knee-braces on strain on the anterior cruciate ligament in vivo*. J Bone Joint Surg Am, 1992. **74**(9): p. 1298-312.
60. Fleming, B.C., et al., *The strain behavior of the anterior cruciate ligament during bicycling. An in vivo study*. Am J Sports Med, 1998. **26**(1): p. 109-18.
61. Fleming, B.C., et al., *An in vivo comparison of anterior tibial translation and strain in the anteromedial band of the anterior cruciate ligament*. J Biomech, 1993. **26**(1): p. 51-8.
62. Howe, J.G., et al., *Arthroscopic strain gauge measurement of the normal anterior cruciate ligament*. Arthroscopy, 1990. **6**(3): p. 198-204.
63. Fleming, B.C., et al., *Determination of a zero strain reference for the anteromedial band of the anterior cruciate ligament*. J Orthop Res, 1994. **12**(6): p. 789-95.
64. Pizzolato, C., et al., *Finding the sweet spot via personalised Achilles tendon training: the future is within reach*. Br J Sports Med, 2019. **53**(1): p. 11-12.
65. Beynnon, B.D., et al., *Anterior cruciate ligament strain behavior during rehabilitation exercises in vivo*. Am J Sports Med, 1995. **23**(1): p. 24-34.
66. Fleming, B.C., et al., *The gastrocnemius muscle is an antagonist of the anterior cruciate ligament*. J Orthop Res, 2001. **19**(6): p. 1178-84.

67. Lee, S.J., et al., *Tibiofemoral contact mechanics after serial medial meniscectomies in the human cadaveric knee*. Am J Sports Med, 2006. **34**(8): p. 1334-44.
68. Zielinska, B. and T.L. Donahue, *3D finite element model of meniscectomy: changes in joint contact behavior*. J Biomech Eng, 2006. **128**(1): p. 115-23.
69. Burks, R.T., M.H. Metcalf, and R.W. Metcalf, *Fifteen-year follow-up of arthroscopic partial meniscectomy*. Arthroscopy, 1997. **13**(6): p. 673-9.
70. Amjadi, M., et al., *Stretchable, Skin-Mountable, and Wearable Strain Sensors and Their Potential Applications: A Review*. Advanced Functional Materials, 2016. **26**(11): p. 1678-1698.
71. Yao, S.S. and Y. Zhu, *Wearable multifunctional sensors using printed stretchable conductors made of silver nanowires*. Nanoscale, 2014. **6**(4): p. 2345-2352.
72. Hwang, B.U., et al., *Transparent Stretchable Self-Powered Patchable Sensor Platform with Ultrasensitive Recognition of Human Activities*. ACS Nano, 2015. **9**(9): p. 8801-10.
73. Zens, M., et al., *A New Approach to Determine Ligament Strain Using Polydimethylsiloxane Strain Gauges: Exemplary Measurements of the Anterolateral Ligament*. Journal of Biomechanical Engineering-Transactions of the Asme, 2014. **136**(12).
74. Lippens, E., et al., *Biocompatibility properties of surface-modified poly(dimethylsiloxane) for urinary applications*. J Biomater Appl, 2013. **27**(6): p. 651-60.
75. Verma, N.K., et al., *Autophagy induction by silver nanowires: A new aspect in the biocompatibility assessment of nanocomposite thin films*. Toxicology and Applied Pharmacology, 2012. **264**(3): p. 451-461.
76. Huang, Q.A., L. Dong, and L.F. Wang, *LC Passive Wireless Sensors Toward a Wireless Sensing Platform: Status, Prospects, and Challenges*. Journal of Microelectromechanical Systems, 2016. **25**(5): p. 822-841.
77. Stauffer, F., et al., *Soft Electronic Strain Sensor with Chipless Wireless Readout: Toward Real-Time Monitoring of Bladder Volume*. Advanced Materials Technologies, 2018. **3**(6).
78. Roberts, T.J., et al., *Muscular force in running turkeys: the economy of minimizing work*. Science, 1997. **275**(5303): p. 1113-5.
79. Boutry, C.M., et al., *A stretchable and biodegradable strain and pressure sensor for orthopaedic application*. Nature Electronics, 2018. **1**(5): p. 314-321.
80. Arai, Y., et al., *Comparative analysis of medial patellofemoral ligament length change pattern in patients with patellar dislocation using open-MRI*. Knee Surgery Sports Traumatology Arthroscopy, 2017. **25**(8): p. 2330-2336.
81. Rainbow, M.J., et al., *Elongation of the dorsal carpal ligaments: a computational study of in vivo carpal kinematics*. J Hand Surg Am, 2012. **37**(7): p. 1393-9.
82. Jeong, W.S., et al., *An analysis of the posterior cruciate ligament isometric position using an in vivo 3-dimensional computed tomography-based knee joint model*. Arthroscopy, 2010. **26**(10): p. 1333-9.
83. Yoo, Y.S., et al., *Changes in ACL length at different knee flexion angles: an in vivo biomechanical study*. Knee Surg Sports Traumatol Arthrosc, 2010. **18**(3): p. 292-7.
84. Goto, A., et al., *Three-dimensional in vivo kinematics during elbow flexion in patients with lateral humeral condyle nonunion by an image-matching technique*. J Shoulder Elbow Surg, 2014. **23**(3): p. 318-26.
85. Iwahashi, T., et al., *Assessment of the "functional length" of the three bundles of the anterior cruciate ligament*. Knee Surg Sports Traumatol Arthrosc, 2008. **16**(2): p. 167-74.
86. Izadpanah, K., et al., *In vivo analysis of coracoclavicular ligament kinematics during shoulder abduction*. Am J Sports Med, 2012. **40**(1): p. 185-92.
87. Yang, C., et al., *In vivo three-dimensional evaluation of the functional length of glenohumeral ligaments*. Clinical Biomechanics, 2010. **25**(2): p. 137-141.
88. Utturkar, G.M., et al., *The effects of a valgus collapse knee position on in vivo ACL elongation*. Ann Biomed Eng, 2013. **41**(1): p. 123-30.

89. Serpell, B.G., et al., *Vertical stiffness is not related to anterior cruciate ligament elongation in professional rugby union players*. *BMJ Open Sport Exerc Med*, 2016. **2**(1): p. e000150.
90. Gray, H.A., S. Guan, and M.G. Pandy, *Accuracy of mobile biplane X-ray imaging in measuring 6-degree -of-freedom patellofemoral kinematics during overground gait*. *Journal of Biomechanics*, 2017. **57**: p. 152-156.
91. Burckhardt, K., et al., *Submillimeter measurement of cup migration in clinical standard radiographs*. *IEEE Trans Med Imaging*, 2005. **24**(5): p. 676-88.
92. Taylor, W.R., et al., *A comprehensive assessment of the musculoskeletal system: The CAMS-Knee data set*. *J Biomech*, 2017. **65**: p. 32-39.
93. DeFrate, L.E., T.J. Gill, and G. Li, *In vivo function of the posterior cruciate ligament during weightbearing knee flexion*. *Am J Sports Med*, 2004. **32**(8): p. 1923-8.
94. Papannagari, R., et al., *Function of posterior cruciate ligament bundles during in vivo knee flexion*. *Am J Sports Med*, 2007. **35**(9): p. 1507-12.
95. Van de Velde, S.K., et al., *In vivo Length Changes of the Anterolateral Ligament and Related Extra-articular Reconstructions*. *Am J Sports Med*, 2016. **44**(10): p. 2557-2562.
96. Yasuda, K., et al., *Anatomic single- and double-bundle anterior cruciate ligament reconstruction, part 1: Basic science*. *Am J Sports Med*, 2011. **39**(8): p. 1789-99.
97. Tashiro, Y., et al., *The Graft Bending Angle Can Affect Early Graft Healing After Anterior Cruciate Ligament Reconstruction: In vivo Analysis With 2 Years' Follow-up*. *American Journal of Sports Medicine*, 2017. **45**(8): p. 1829-1836.
98. Tashiro, Y., et al., *In vivo Analysis of Dynamic Graft Bending Angle in Anterior Cruciate Ligament-Reconstructed Knees During Downward Running and Level Walking: Comparison of Flexible and Rigid Drills for Transportal Technique*. *Arthroscopy-the Journal of Arthroscopic and Related Surgery*, 2017. **33**(7): p. 1393-1402.
99. de Asla, R.J., et al., *Function of anterior talofibular and calcaneofibular ligaments during in-vivo motion of the ankle joint complex*. *J Orthop Surg Res*, 2009. **4**: p. 7.
100. Van de Velde, S.K., et al., *The effect of anterior cruciate ligament deficiency on the in vivo elongation of the medial and lateral collateral ligaments*. *Am J Sports Med*, 2007. **35**(2): p. 294-300.
101. Park, S.E., et al., *Erratum to "The change in length of the medial and lateral collateral ligaments during in vivo knee flexion"*. *Knee*, 2006. **13**(1): p. 77-82.
102. Nagai, K., et al., *The Complex Relationship Between In vivo ACL Elongation and Knee Kinematics During Walking and Running*. *Journal of Orthopaedic Research*, 2019. **37**(9): p. 1920-1928.
103. Kernkamp, W.A., et al., *The Medial Patellofemoral Ligament Is a Dynamic and Anisometric Structure: An In vivo Study on Length Changes and Isometry*. *American Journal of Sports Medicine*, 2019. **47**(7): p. 1645-1653.
104. Massimini, D.F., et al., *In-vivo glenohumeral translation and ligament elongation during abduction and abduction with internal and external rotation*. *J Orthop Surg Res*, 2012. **7**: p. 29.
105. Yue, B., et al., *In vivo function of posterior cruciate ligament before and after posterior cruciate ligament-retaining total knee arthroplasty*. *Int Orthop*, 2012. **36**(7): p. 1387-92.
106. Park, K.K., et al., *Elongation of the collateral ligaments after cruciate retaining total knee arthroplasty and the maximum flexion of the knee*. *J Biomech*, 2015. **48**(3): p. 418-24.
107. Hosseini Nasab, S.H., et al., *Length-Change Patterns of the Collateral Ligaments During Functional Activities After Total Knee Arthroplasty*. *Ann Biomed Eng*, 2020. **48**(4): p. 1396-1406.
108. Abebe, E.S., et al., *The effect of femoral tunnel placement on ACL graft orientation and length during in vivo knee flexion*. *J Biomech*, 2011. **44**(10): p. 1914-20.
109. LaPrade, R.F., et al., *The anatomy of the medial part of the knee*. *J Bone Joint Surg Am*, 2007. **89**(9): p. 2000-10.

110. Araki, D., E. Thorhauer, and S. Tashman, *Three-dimensional isotropic magnetic resonance imaging can provide a reliable estimate of the native anterior cruciate ligament insertion site anatomy*. Knee Surgery Sports Traumatology Arthroscopy, 2018. **26**(5): p. 1311-1318.
111. Ellingson, A.M., et al., *Characterizing fluoroscopy based kinematic accuracy as a function of pulse width and velocity*. Journal of Biomechanics, 2016. **49**(15): p. 3741-3745.
112. Hosseini Nasab, S.H., et al., *Elongation Patterns of the Collateral Ligaments After Total Knee Arthroplasty Are Dominated by the Knee Flexion Angle*. Front Bioeng Biotechnol, 2019. **7**: p. 323.
113. List, R., et al., *A moving fluoroscope to capture tibiofemoral kinematics during complete cycles of free level and downhill walking as well as stair descent*. Plos One, 2017. **12**(10).
114. Huber, C., et al., *Properties and Function of the Medial Patellofemoral Ligament: A Systematic Review*. Am J Sports Med, 2020. **48**(3): p. 754-766.
115. Tashman, S., et al., *Dynamic function of the ACL-reconstructed knee during running*. Clin Orthop Relat Res, 2007. **454**: p. 66-73.
116. Taylor, K.A., et al., *Measurement of in vivo anterior cruciate ligament strain during dynamic jump landing*. J Biomech, 2011. **44**(3): p. 365-71.
117. Guan, S., et al., *Mobile Biplane X-Ray Imaging System for Measuring 3D Dynamic Joint Motion During Overground Gait*. Ieee Transactions on Medical Imaging, 2016. **35**(1): p. 326-336.
118. Hitz, M., et al., *Influence of the moving fluoroscope on gait patterns*. PLoS One, 2018. **13**(7): p. e0200608.
119. Yang, X.F. and B.W. Fei, *3D Prostate Segmentation of Ultrasound Images Combining Longitudinal Image Registration and Machine Learning*. Medical Imaging 2012: Image-Guided Procedures, Robotic Interventions, and Modeling, 2012. **8316**.
120. Yang, X.F., et al., *Automated Segmentation of the Parotid Gland Based on Atlas Registration and Machine Learning: A Longitudinal MRI Study in Head-and-Neck Radiation Therapy*. International Journal of Radiation Oncology Biology Physics, 2014. **90**(5): p. 1225-1233.
121. Miller, R.M., et al., *Effects of Tendon Degeneration on Predictions of Supraspinatus Tear Propagation*. Ann Biomed Eng, 2019. **47**(1): p. 154-161.
122. Schepull, T. and P. Aspenberg, *Early controlled tension improves the material properties of healing human achilles tendons after ruptures: a randomized trial*. Am J Sports Med, 2013. **41**(11): p. 2550-7.
123. Schepull, T., et al., *Mechanical properties during healing of Achilles tendon ruptures to predict final outcome: a pilot Roentgen stereophotogrammetric analysis in 10 patients*. BMC Musculoskelet Disord, 2007. **8**: p. 116.
124. Jonsson, H., et al., *Lengthening of anterior cruciate ligament graft. Roentgen stereophotogrammetry of 32 cases 2 years after repair*. Acta Orthop Scand, 1992. **63**(6): p. 587-92.
125. Adam, F., et al., *Length of the patellar tendon after anterior cruciate ligament reconstruction with patellar tendon autograft: a prospective clinical study using Roentgen stereometric analysis*. Arthroscopy, 2002. **18**(8): p. 859-64.
126. Aspenberg, P. and T. Schepull, *Substantial creep in healing human Achilles tendons. A pilot study*. Muscles Ligaments Tendons J, 2015. **5**(3): p. 151-5.
127. Schepull, T., J. Kvist, and P. Aspenberg, *Early E-modulus of healing Achilles tendons correlates with late function: similar results with or without surgery*. Scand J Med Sci Sports, 2012. **22**(1): p. 18-23.
128. Tashman, S. and W. Anderst, *In-vivo measurement of dynamic joint motion using high speed biplane radiography and CT: Application to canine ACL deficiency*. Journal of Biomechanical Engineering-Transactions of the Asme, 2003. **125**(2): p. 238-245.
129. Mc Auliffe, S., et al., *A systematic review of the reliability of diagnostic ultrasound imaging in measuring tendon size: Is the error clinically acceptable?* Phys Ther Sport, 2017. **26**: p. 52-63.

130. Franz, J.R., et al., *Non-uniform in vivo deformations of the human Achilles tendon during walking*. *Gait Posture*, 2015. **41**(1): p. 192-7.
131. Joseph, C.W., et al., *Early changes in Achilles tendon behaviour in vivo following downhill backwards walking*. *J Sports Sci*, 2016. **34**(13): p. 1215-21.
132. Farris, D.J., et al., *The effects of orthotic heel lifts on Achilles tendon force and strain during running*. *J Appl Biomech*, 2012. **28**(5): p. 511-9.
133. Lichtwark, G.A., K. Bougoulas, and A.M. Wilson, *Muscle fascicle and series elastic element length changes along the length of the human gastrocnemius during walking and running*. *J Biomech*, 2007. **40**(1): p. 157-64.
134. Slane, L.C., et al., *The challenges of measuring in vivo knee collateral ligament strains using ultrasound*. *Journal of Biomechanics*, 2017. **61**: p. 258-262.
135. Kwah, L.K., et al., *Reliability and validity of ultrasound measurements of muscle fascicle length and pennation in humans: a systematic review*. *J Appl Physiol* (1985), 2013. **114**(6): p. 761-9.
136. Rantanen, N.W. and R.L. Ewing, *Principles of Ultrasound Application in Animals*. *Veterinary Radiology*, 1981. **22**(5): p. 196-203.
137. Sandrin, L., et al., *Shear elasticity probe for soft tissues with 1-D transient elastography*. *IEEE Trans Ultrason Ferroelectr Freq Control*, 2002. **49**(4): p. 436-46.
138. Fabiszewska, E., et al., *Evaluation of Imaging Parameters of Ultrasound Scanners: Baseline for Future Testing*. *Polish Journal of Radiology*, 2017. **82**: p. 773-782.
139. Kongsgaard, M., et al., *Mechanical properties of the human Achilles tendon, in vivo*. *Clin Biomech (Bristol, Avon)*, 2011. **26**(7): p. 772-7.
140. Farris, D.J., G. Trewartha, and M.P. McGuigan, *Could intra-tendinous hyperthermia during running explain chronic injury of the human Achilles tendon?* *J Biomech*, 2011. **44**(5): p. 822-6.
141. Lichtwark, G.A. and A.M. Wilson, *In vivo mechanical properties of the human Achilles tendon during one-legged hopping*. *J Exp Biol*, 2005. **208**(Pt 24): p. 4715-25.
142. Peltonen, J., et al., *Achilles tendon stiffness is unchanged one hour after a marathon*. *J Exp Biol*, 2012. **215**(Pt 20): p. 3665-71.
143. Nuri, L., et al., *Regional three-dimensional deformation of human Achilles tendon during conditioning*. *Scand J Med Sci Sports*, 2016.
144. Slane, L.C. and D.G. Thelen, *The use of 2D ultrasound elastography for measuring tendon motion and strain*. *Journal of Biomechanics*, 2014. **47**(3): p. 750-754.
145. Bogaerts, S., et al., *Evaluation of tissue displacement and regional strain in the Achilles tendon using quantitative high-frequency ultrasound*. *PLoS One*, 2017. **12**(7): p. e0181364.
146. Korstanje, J.W., et al., *Development and validation of ultrasound speckle tracking to quantify tendon displacement*. *J Biomech*, 2010. **43**(7): p. 1373-9.
147. Slane, L.C., et al., *Evidence of patellar tendon buckling during passive knee extension*. *Knee*, 2016. **23**(5): p. 801-6.
148. Schweitzer, M.E., D.G. Mitchell, and S.M. Ehrlich, *The Patellar Tendon - Thickening, Internal Signal Buckling, and Other Mr Variants*. *Skeletal Radiology*, 1993. **22**(6): p. 411-416.
149. Martin, J.A., et al., *Gauging force by tapping tendons*. *Nat Commun*, 2018. **9**(1): p. 1592.
150. Bouillard, K., A. Nordez, and F. Hug, *Estimation of Individual Muscle Force Using Elastography*. *Plos One*, 2011. **6**(12).
151. Hirata, K., et al., *Evidence for intermuscle difference in slack angle in human triceps surae*. *Journal of Biomechanics*, 2015. **48**(6): p. 1210-1213.
152. Farris, D.J., G. Trewartha, and M.P. McGuigan, *The effects of a 30-min run on the mechanics of the human Achilles tendon*. *Eur J Appl Physiol*, 2012. **112**(2): p. 653-60.
153. Bennett, M.B., et al., *Mechanical-Properties of Various Mammalian Tendons*. *Journal of Zoology*, 1986. **209**: p. 537-548.

154. Cronin, N.J., et al., *Achilles tendon length changes during walking in long-term diabetes patients*. *Clinical Biomechanics*, 2010. **25**(5): p. 476-482.
155. Cronin, N.J. and T. Finni, *Treadmill versus overground and barefoot versus shod comparisons of triceps surae fascicle behaviour in human walking and running*. *Gait & Posture*, 2013. **38**(3): p. 528-533.
156. Cronin, N.J., B. Hanley, and A. Bissas, *Mechanical and neural function of triceps surae in elite racewalking*. *Journal of Applied Physiology*, 2016. **121**(1): p. 101-105.
157. Leitner, C., et al., *Ultrasound as a Tool to Study Muscle-Tendon Functions during Locomotion: A Systematic Review of Applications*. *Sensors (Basel)*, 2019. **19**(19).
158. Ishikawa, M., et al., *Muscle-tendon interaction and elastic energy usage in human walking*. *Journal of Applied Physiology*, 2005. **99**(2): p. 603-608.
159. Lichtwark, G.A., K. Bougoulas, and A.M. Wilson, *Muscle fascicle and series elastic element length changes along the length of the human gastrocnemius during walking and running*. *Journal of Biomechanics*, 2007. **40**(1): p. 157-164.
160. Mian, O.S., et al., *Gastrocnemius muscle-tendon behaviour during walking in young and older adults*. *Acta Physiologica*, 2007. **189**(1): p. 57-65.
161. Ishikawa, M., J. Pakaslahti, and P.V. Komi, *Medial gastrocnemius muscle behavior during human running and walking*. *Gait & Posture*, 2007. **25**(3): p. 380-384.
162. Suzuki, T., et al., *Forefoot running requires shorter gastrocnemius fascicle length than rearfoot running*. *Journal of Sports Sciences*, 2019. **37**(17): p. 1972-1980.
163. Ishikawa, M. and P.V. Komi, *The role of the stretch reflex in the gastrocnemius muscle during human locomotion at various speeds*. *Journal of Applied Physiology*, 2007. **103**(3): p. 1030-1036.
164. Spanjaard, M., et al., *Influence of step-height and body mass on gastrocnemius muscle fascicle behavior during stair ascent*. *J Biomech*, 2008. **41**(5): p. 937-44.
165. Graves, N.C., et al., *Ultrasound assessment of dorsal Lisfranc ligament strain under clinically relevant loads*. *J Am Podiatr Med Assoc*, 2014. **104**(1): p. 11-8.
166. Marshall, J.J., et al., *Ultrasound assessment of bilateral symmetry in dorsal Lisfranc ligament*. *J Foot Ankle Surg*, 2013. **52**(3): p. 319-23.
167. Ryba, D., et al., *Evaluation of dorsal Lisfranc ligament deformation with load using ultrasound imaging*. *Foot (Edinb)*, 2016. **26**: p. 30-5.
168. Moraux, A., et al., *Anatomical study of the pisotriquetral joint ligaments using ultrasonography*. *Skeletal Radiol*, 2012. **41**(3): p. 321-8.
169. Thoirs, K.A. and J. Childs, *Are Ultrasound Measurements of Achilles Tendon Size Reliable? A Systematic Review of Rater Reliability*. *Ultrasound Med Biol*, 2018. **44**(12): p. 2476-2491.
170. Barfod, K.W., et al., *Validity and reliability of an ultrasound measurement of the free length of the Achilles tendon*. *Dan Med J*, 2018. **65**(3).
171. Ahmad, A., et al., *Reliability of musculoskeletal ultrasound imaging to measure supraspinatus tendon thickness in healthy subjects*. *J Phys Ther Sci*, 2017. **29**(8): p. 1394-1398.
172. Del Bano-Aledo, M.E., et al., *Ultrasound measures of tendon thickness: Intra-rater, Inter-rater and Inter-machine reliability*. *Muscles Ligaments Tendons J*, 2017. **7**(1): p. 192-199.
173. Gellhorn, A.C. and M.J. Carlson, *Inter-rater, intra-rater, and inter-machine reliability of quantitative ultrasound measurements of the patellar tendon*. *Ultrasound Med Biol*, 2013. **39**(5): p. 791-6.
174. Schulze, F., et al., *A wide number of trials is required to achieve acceptable reliability for measurement patellar tendon elongation in vivo*. *Gait Posture*, 2012. **35**(2): p. 334-8.
175. Intziagianni, K., et al., *Ultrasonography for the assessment of the structural properties of the Achilles tendon in asymptomatic individuals: An intra-rater reproducibility study*. *Isokinetics and Exercise Science*, 2015. **23**(4): p. 263-270.

176. Nadeau, M.J., et al., *Quantitative ultrasound imaging of Achilles tendon integrity in symptomatic and asymptomatic individuals: reliability and minimal detectable change*. Journal of Foot and Ankle Research, 2016. **9**.
177. Klimstra, M., et al., *The effect of ultrasound probe orientation on muscle architecture measurement*. J Electromyogr Kinesiol, 2007. **17**(4): p. 504-14.
178. Kremkau, F.W., *Seeing is believing? Sonographic artifacts*. Physics Today, 2007. **60**(3): p. 84-85.
179. Wood, N., J.G. Konin, and C. Nofsinger, *Diagnosis of an ulnar collateral ligament tear using musculoskeletal ultrasound in a collegiate baseball pitcher: a case report*. N Am J Sports Phys Ther, 2010. **5**(4): p. 227-33.
180. Skovgaard Larsen, L.P. and O.S. Rasmussen, *Diagnosis of acute rupture of the anterior cruciate ligament of the knee by sonography*. Eur J Ultrasound, 2000. **12**(2): p. 163-7.
181. Wang, J.H., et al., *The role of ultrasonography in the diagnosis of anterior cruciate ligament injury: A systematic review and meta-analysis*. European Journal of Sport Science, 2018. **18**(4): p. 579-586.
182. Lee, S.H. and S.J. Yun, *Efficiency of knee ultrasound for diagnosing anterior cruciate ligament and posterior cruciate ligament injuries: a systematic review and meta-analysis*. Skeletal Radiol, 2019.
183. Chen, P.T., et al., *Sonography of the Normal Anterior Cruciate Ligament: A Preliminary Report*. Journal of Medical Ultrasound, 2013. **21**(1): p. 16-20.
184. Obst, S.J., R. Newsham-West, and R.S. Barrett, *In vivo Measurement of Human Achilles Tendon Morphology Using Freehand 3-D Ultrasound*. Ultrasound in Medicine and Biology, 2014. **40**(1): p. 62-70.
185. Farris, D.J., et al., *Differential strain patterns of the human Achilles tendon determined in vivo with freehand three-dimensional ultrasound imaging*. J Exp Biol, 2013. **216**(Pt 4): p. 594-600.
186. Obst, S.J., et al., *Reliability of Achilles Tendon Moment Arm Measured In vivo Using Freehand Three-Dimensional Ultrasound*. J Appl Biomech, 2017. **33**(4): p. 300-304.
187. Lichtwark, G.A., A.G. Cresswell, and R.J. Newsham-West, *Effects of running on human Achilles tendon length-tension properties in the free and gastrocnemius components*. J Exp Biol, 2013. **216**(Pt 23): p. 4388-94.
188. Obst, S.J., R. Newsham-West, and R.S. Barrett, *Three-dimensional morphology and strain of the human Achilles free tendon immediately following eccentric heel drop exercise*. J Exp Biol, 2015. **218**(Pt 24): p. 3894-900.
189. Martin, J.A., et al., *Gauging force by tapping tendons*. Nature Communications, 2018. **9**.
190. Moo, E.K., et al., *In vivo muscle force and muscle power during near-maximal frog jumps*. PLoS One, 2017. **12**(3): p. e0173415.
191. Foldhazy, Z., et al., *Exercise-induced strain and strain rate in the distal radius*. J Bone Joint Surg Br, 2005. **87**(2): p. 261-6.
192. Torniaainen, J., et al., *Near Infrared Spectroscopic Evaluation of Ligament and Tendon Biomechanical Properties*. Ann Biomed Eng, 2019. **47**(1): p. 213-222.

Chapter 3: Soft Electronic Strain Sensor with Chipless Wireless Readout: Toward Real-Time Monitoring of Bladder Volume

Flurin Stauffer¹, Qiang Zhang², Klas Tybrandt^{1,3}, Byron Llerena Zambrano¹, Julian Hengsteler¹, André Stoll¹, Camill Trüeb¹, Michael Hagander¹, Jean-Marc Sujata¹, Felix Hoffmann¹, Joy Schuurmans Stekhoven¹, Josefine Quack¹, Hannes Zilly¹, Johannes Goedejohann¹, Marc P. Schneider^{4,5,6}, Thomas M. Kessler⁴, William R. Taylor², Roland Küng⁷, and János Vörös^{1*}

¹Laboratory of Biosensors and Bioelectronics, ETH Zurich, Gloriastrasse 35, 8092 Zurich, Switzerland

²Laboratory for Movement Biomechanics, ETH Zurich, Leopold-Ruzicka-Weg 4, 8093 Zurich, Switzerland

³Laboratory of Organic Electronics, Linköping University, 601 74 Norrköping, Sweden

⁴Neuro-Urology, Spinal Cord Injury Center & Research, University of Zurich, Balgrist University Hospital, Forchstrasse 340, 8008 Zurich, Switzerland

⁵Department of Health Sciences and Technology, Brain Research Institute, University of Zurich, ETH Zurich, Winterthurerstrasse 190, 8057 Zurich, Switzerland

⁶Department of Urology, University of Bern, Murtenstrasse 35, 3008 Bern, Switzerland

⁷Center for Communications Systems, School of Engineering, Zurich University of Applied Sciences, Technikumstrasse 9, 8400 Winterthur, Switzerland

Published as:

Stauffer, F., Q. Zhang, K. Tybrandt, B. L. Zambrano, J. Hengsteler, A. Stoll, C. Trüeb, M. Hagander, J. M. Sujata, F. Hoffmann, J. S. Stekhoven, J. Quack, H. Zilly, J. Goedejohann, M. P. Schneider, T. M. Kessler, W. R. Taylor, R. Kung and J. Voros (2018). "Soft Electronic Strain Sensor with Chipless Wireless Readout: Toward Real-Time Monitoring of Bladder Volume." *Advanced Materials Technologies* 3(6).

The thesis author's individual contributions:

In this study, the author mainly worked on the preparation of capacitor and LCR sensor samples. The author jointly performed the tensile testing on the sensor sample, as well as the final *ex-vivo* measurements of the bladder volume.

Reasons that the paper fits into the topic of this thesis:

This paper presented a stretchable sensor technology, which serves as the foundation of the development of the stretchable strain sensor for measuring musculoskeletal soft tissue strains. Therefore, this paper consists of key technological information that is critical to the interpretation on the rationality of further sensor optimization. In addition, during his PhD, parts of the thesis author's work was to collaborate with Dr. Flurin Stauffer to finalize the technology development and validation (within the scope of this paper), in order to handle the sensor fabrication approaches for executing his own PhD project.

Abstract

Sensing mechanical tissue deformation *in vivo* can provide detailed information on organ functionality and tissue states. To bridge the huge mechanical mismatch between conventional electronics and biological tissues, stretchable electronic systems have recently been developed for interfacing tissues in healthcare applications. A major challenge for wireless electronic implants is that they typically require microchips, which adds complexity and may compromise long-term stability. Here, a chipless wireless strain sensor technology based on a novel soft conductor with high cyclic stability is reported. The composite material consists of gold-coated titanium dioxide nanowires embedded in a soft silicone elastomer. The implantable strain sensor is based on a resonant circuit which consists of a stretchable plate capacitor and a coil for inductive readout of its resonance frequency. Successful continuous wireless readout during 50% strain cycles is demonstrated. The sensor element has a Young's modulus of 260 kPa, similar to that of the bladder in order to not impair physiological bladder expansion. A proof-of-principle measurement on an *ex-vivo* porcine bladder is presented, which shows the feasibility of the presented materials and devices for continuous, wireless strain monitoring of various tissues and organs *in vivo*.

Keywords: Chipless, Soft conductors, Strain sensors, Stretchable electronics, Wireless sensors

3.1. Introduction

Sensing tissue deformation can provide important insights into tissue states, functionality, response to injury, diseases, and healing progression. Stretchable electronics have been developed to seamlessly adapt to curved and rough surfaces in dynamic environments such as biological tissues. In addition, by reducing the mechanical mismatch between electrical devices and the surrounding soft tissues, such devices can effectively reduce tissue damage, enabling close device integration for non-invasive and invasive monitoring, as well as diagnostic and therapeutic applications in modern healthcare.^[1–3] For instance, continuous, long-term monitoring of deformation of the bladder could provide critical information to patients with neurogenic lower urinary tract dysfunction.^[4] Similar conditions can also be found in patients with spinal cord injury, who not only suffer from reduced motor ability, but often also lose part of their body's proprioceptive feedback system, including a loss of sensation of the bladder filling level. This represents a severe challenge to the patient's health-related quality of life,^[5] since excessive storage pressure in the bladder may lead to urinary reflux toward the kidneys, severe damage of the upper urinary tract, and progression toward kidney failure.^[3,5]

Nowadays, state-of-the-art treatment for preventing overpressure in the bladder requires that patients perform intermittent self-catheterization four to six times daily, regardless of how full their bladder is.^[4,6] Even though techniques for monitoring deformation of the bladder have previously been developed, these approaches still have several obstacles to overcome.^[7] Here, gold-standard non-invasive technologies use ultrasound or catheter-based instruments that are applicable for acute measurements, however continuous monitoring over days is not feasible.^[8] Implantable solutions have also been investigated, mainly based on resistance or capacitive changes in the sensing element,^[9–11] but such approaches are limited by issues involving biocompatibility, hermetic packaging, communication, operating power, drift, or incompatibility with medical imaging tools.^[7] Moreover, readout of deformation changes requires an implantable electronic circuit for measurement and communication to the electronics outside of the body, and therefore requires complex hermetic packaging strategies.

To circumvent active electronics, an elegant solution has been reported that uses passive wireless resonant sensors for measuring pressure, strain, temperature, and humidity among others.^[12,13] However, no existing passive sensor solution has yet been proposed that is suitable for the assessment of high deformations (>20% strain) without interfering with the bladder expansion. In recent years, tremendous progress has been made towards conductors that are highly stretchable while maintaining high conductivity^[14–17] as well as highly stretchable strain sensors.^[18–22] Most of these approaches use polydimethylsiloxane (PDMS) or other elastomers with a Young's modulus (E) of a few MPa,^[14] which is nevertheless still considerably higher than most biological tissues.^[23] A promising solution for producing ultrasoft conductors involves liquid metals embedded in very soft elastomers such as Ecoflex ($E = 30\text{--}70$ kPa).^[24,25] However, whether these approaches are feasible for implants remains unclear,

since their possible long-term degradation due to oxidation is plausibly problematic in wet body fluid environments. Therefore, an ultrasoft, implantable, and long-term stable stretchable conductor is still missing.

In this work, we present a soft stretchable conductor based on gold-coated titanium dioxide nanowire (Au-TiO₂ NW) layers embedded in an ultrasoft silicone elastomer that remains conductive at strains as high as 100% without substantial cyclic fatigue. We describe a strain sensing approach for an implantable, passive RLC circuit to measure full range tissue deformation, based on stretchable electronics with a wireless readout system that avoids any active circuit elements in the implant. Our strain sensing element is designed to have similar mechanical properties to the tissue in order to avoid interference through mechanical deformation during bladder filling. Our approach uses an operating resonance frequency from 1 to 30 MHz, where the tissue is basically invisible to the electromagnetic inductive coupling, making it feasible to communicate through higher tissue depths compared with most wireless systems that work within the high MHz to GHz region. Working toward the development of a closed-loop neuroprosthetic bladder control system,^[26] our vision is to bridge the gap between minimally invasive strain measurement systems while still allowing continuous monitoring of bladder expansion status over time.

3.2. Results and Discussions

The system consists of an implantable stretchable sensor and a portable readout system that can further communicate with a mobile phone (Figure 1a). The circuit diagram of the sensor system is illustrated in Figure 1b. The implantable sensor consists of an electrical RLC circuit with a variable capacitor that changes upon strain. The resulting changes in the RLC resonance frequency can be read wirelessly by inductive coupling via the coils of the sensor and the readout system. The portable readout system with its coil is shown in Figure 1c. The stretchable RLC circuit (Figure 1d) is composed of an electromagnetic coil, i.e., a coiled electrical wire connected to a stretchable capacitor that acts as the sensing element. The size of the stretchable sensing element can be tuned from millimetres to centimetres without changing the resonance frequency range by adjusting the dimensions of the plate capacitor and the coil windings. Therefore, the sensor size and the tissue surface coverage can be tailored accordingly. The stretchable plate capacitor comprises of two-stacked layers of Au-TiO₂ NW films embedded in an elastomer matrix (Figure 1e).

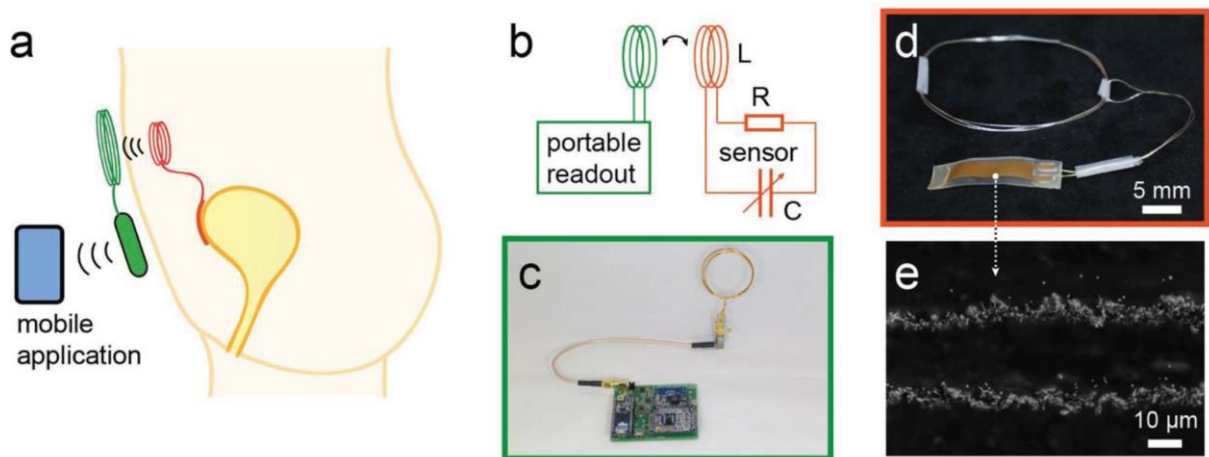


Figure 1. Concept for an implantable, passive strain sensor to measure large tissue deformations wirelessly. a) Schematics of proposed concept including the passive, implantable sensor, a portable readout system, and a mobile application. b) Circuit diagram of the sensor system. The sensor consists of an RLC circuit with a stretchable capacitor acting as the sensing element. The resonance frequency of the sensor is readout via inductive coupling. c) Photo of the readout system with its coil. d) Photo of the implantable RLC sensor with a stretchable capacitor based on a soft Au-TiO₂ NW– elastomer composite. e) Side view scanning electron microscope image of a cut through the stretchable plate capacitor exposing the conductive double layer embedded in the elastomer.

3.2.1. Electromechanical Aspects: Ultrasoft Stretchable Conductors

A key factor for a successful stretchable sensor is the maintenance of high conductivity even during high strains and cyclic reliability without fatigue. Creating an implantable, ultrasoft conductor that fulfils these requirements is not trivial. High performance stretchable NW conductors are often based on silver NWs (AgNWs) embedded in polydimethylsiloxane (PDMS), mostly Sylgard 184.^[27,28] Toward soft implants with long-term biocompatibility and stability, we developed novel Au-TiO₂ NWs to replace

the AgNWs. Biocompatibility of these Au-TiO₂ NWs embedded in an elastomer (Sylgard 184) was demonstrated by Tybrandt et al. with electrode arrays implanted on the brain surface in freely moving rats and successful brain activity recordings over three months.^[29] In addition to improved biocompatibility and stability, the Au-TiO₂ NWs are directly applicable to softer elastomers like Dragonskin (DS) as the fracture formation remains limited to microcracks (Figure 2a). In comparison, AgNW networks embedded in DS showed substantial crack formation in the AgNW film upon strain, eventually leading to electronic failure even at low strains (Figure S1, Supporting Information). Stretchable samples were fabricated with an Au-TiO₂ NW film embedded in DS that had 20 mm long and 0.5 mm wide tracks (Figure 2b), as described in the Experimental Section. The sample had an initial resistance of 21.7 Ω corresponding to a sheet resistance of 0.54 $\Omega \square^{-1}$ and a conductivity of 4630 S cm⁻¹ for an average layer thickness of around 4 μ m. The track remains conductive even during strains as high as 100% with a resistance of 1250 Ω (corresponding to 11 $\Omega \square^{-1}$). Cyclic reliability was examined over 500 successive strain cycles for 5%, 20%, 50%, and 100% strains of our novel soft conductor (Figure 2c). Interestingly, even after 500 cycles of stretching to 100% strain, the resistance recovers to 27.1 Ω (corresponding to 0.678 $\Omega \square^{-1}$), which was only a 24.7% increase over the initial value. This loss in conductivity is attributed to nonreversible loss in electrical NW–NW contacts in the initial cycles. The Au-TiO₂ NW shows the same performance if embedded in Sylgard 184 (Figure S2, Supporting Information).

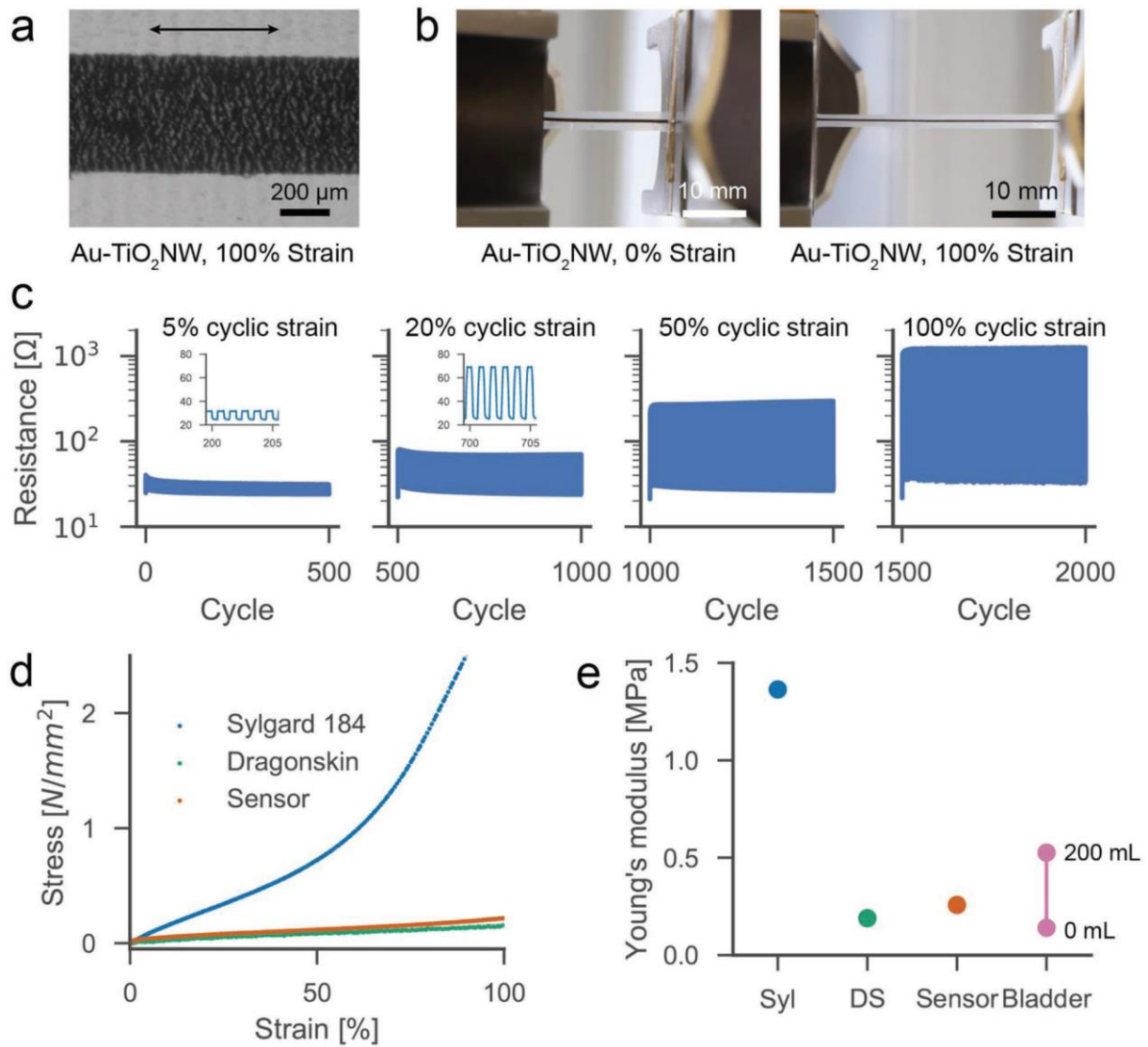


Figure 2. Electromechanical characterization of the soft and stretchable conductor. a) Bright field images showed formation of microcracks at 100% strain but maintained an electrically conductive path along the full track. b) Photo of an Au-TiO₂NW-DS track at 0% and 100% strain. c) Electrical resistance measured during cyclic strain of an Au-TiO₂NW-DS composite track with progressive increase in strain with 500 cycles each. The insets show 5 cycles. d) The stress-strain curve of the sensor, a double-layered Au-TiO₂NW-DS composite, is compared to pure Sylgard 184 and DS 10 without filler material. e) The Young's modulus calculated from the stress-strain curve at 40% strain compared to ex-vivo pig bladder values that varies with the filling volume.

Since the sensor element deforms with the bladder wall, the mechanical properties of the sensor are crucial. The sensor needs to be soft enough to not hinder bladder deformation. Therefore, the Young's modulus of the sensing element needs to be smaller than or similar to that of the bladder wall. Stretchable samples with double-layered Au-TiO₂ NW films were fabricated by subsequent Au-TiO₂ NW transfer from filter membranes and encapsulation in DS.^[28] The mechanical property of this double-layered sample was compared with DS without fillers and PDMS (Sylgard 184). The samples were stretched above 100% while measuring the applied stress as shown in Figure 2d. The corresponding Young's modulus at 40% strain was 260 kPa, 190 kPa, and 1.36 MPa for the sensor, pure DS, and

Sylgard 184, respectively. The double-layered filler increased the modulus of DS by only 37%. This is a very small effect compared with other filling materials such as metallic particles or carbon nanotubes that produce a more substantial increase.^[30–32] Importantly, the sensor is still five times softer than PDMS. Organs like the human bladder can highly deform and hold a filling volume of between 300 and 500 mL before the desire to urinate occurs, but can hold considerably more if necessary.^[33] The Young’s modulus of porcine bladder *in vivo* is dominated by the mucosa layer of the bladder wall and was measured to be around 64–183 kPa depending on the position.^[34] In addition, the Young’s modulus of the bladder wall also depends on its filling state varying from 140 to 526 kPa as measured *ex vivo* for a bladder filling state from 0 to 200 mL.^[34] Our sensor element lies in a similar Young’s modulus range (Figure 2e). Since our sensor is five to ten times thinner than the bladder wall, the mechanical influence on the expanding bladder should be minimal. Finally, using this soft Au-TiO₂ NW–DS composite, we fabricated planar plate capacitors that increase their capacitance upon strain (ϵ) according to geometrical changes, with

$$C = (1 + \epsilon)C_0 \quad (1)$$

as shown in Figure 3a.

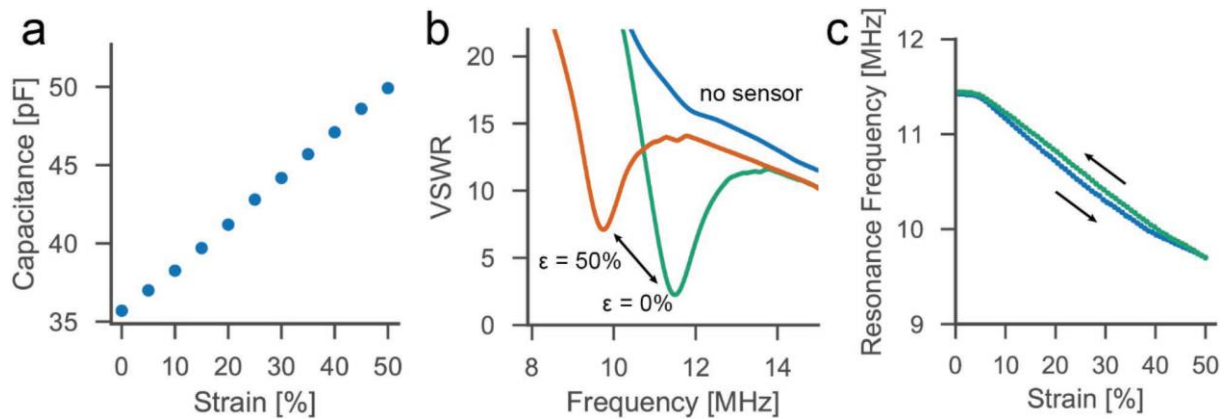


Figure 3. Characterization of the highly stretchable wireless strain sensor. a) The capacitance of the sensor changes linearly with strain. b) The measured VSWR over frequency without sensor and with an electromagnetically coupled RLC sensor at 0% and 50% strain. c) Applying strain on the sensor leads to an increase in capacitance and therefore to a decrease in resonance frequency. The forward and reverse response during the 1000th cycle stretched to 50% is shown.

3.2.2. Wireless Strain Sensing

The sensing principle is based on inductive coupling of the RLC sensor circuit with a readout coil outside of the body (Figure 1). The readout system uses a frequency sweep for detecting the resonance frequency of the sensor. Here, a portable Arduino-based network analyser was constructed to measure the voltage standing wave ratio (VSWR) of the RLC sensor system (Figure 1c). If the capacitor is stretched, it causes a relative change in resonance frequency of the RLC circuit. The undamped resonance frequency of the sensor is

$$f = \frac{1}{2\pi\sqrt{LC}} \quad (2)$$

where L is the inductance and C is the capacitance. For the underdamped resonance frequency, we can assume $f_d \approx f$ (see Supporting Information). Figure 3b shows the VSWR measurement of the readout system with and without a coupled sensor at 0% strain and at 50% strain. The peak in the VSWR measurement is caused by the resonance frequency of the sensor. Stretching the capacitor leads to an increase in capacitance, which results in decrease in resonance frequency with only minimal hysteresis during the stretch cycle (Figure 3c). The small hysteresis occurs likely due to a viscoelastic relaxation effect in the elastomer which can influence and delay the geometrical changes of the capacitor. The resonance frequency in dependency of the initial resonance frequency f_0 and the strain is given by

$$f = \frac{f_0}{\sqrt{1 + \epsilon}} \quad (3)$$

as derived in the Supporting Information and shown in Figure S3 in the Supporting Information. For strains between 0 and 0.5, the gauge factor ranges between 0.37 and 0.5 (Equation (S9), Supporting Information). Upon emersion of the sensor in water, the resonance frequency lowers by around 1 MHz due to a change of the coil inductance L (Figure S4a, Supporting Information). The stretchable sensing element was not affected by the immersion in water or body fluids. In addition to the presented sensor, our fabrication method and the high conductivity also allow for creating fully stretchable RLC sensors while avoiding additional cables and contacts (Figure S5, Supporting Information).

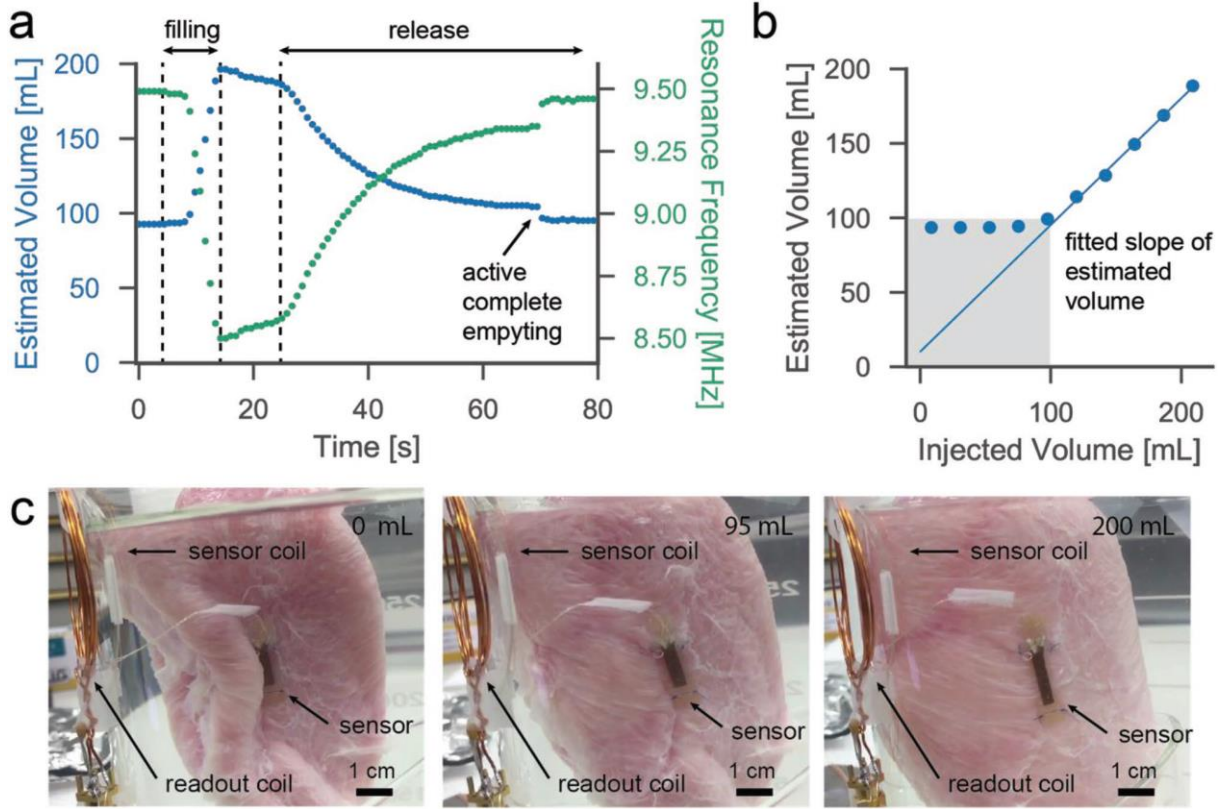


Figure 4. Demonstration of wireless strain sensing in water on a fresh *ex-vivo* pig bladder. a) water (200 mL) was pumped into the bladder, while the resonance frequency of the sensor is monitored continuously from outside the bath with the wireless readout. The sensor response was used to estimate the filling level of the bladder. Initially, the bladder was completely empty for 5 s. Filling the bladder leads to an initial unfolding before expanding. At full expansion, the estimated filling level drops slightly due to the internal pressure causing water flowing back into the tubing system and minor sensor hysteresis. Finally, passive bladder voiding leads to a decrease in bladder volume. The sensor is back to the original state after complete voiding. b) Estimated versus injected volume during the filling process and actual bladder expansion. The sensor measures the expansion but not the unfolding of the bladder (in grey). c) Images during the bladder extension with the sutured sensor and the wireless readout. The bladder is folded at 0 mL, unfolds completely at around 95 mL, and is highly extended at 200 mL.

3.2.3. *Ex-Vivo* Bladder Volume Sensing

In order to demonstrate the proof of concept of our strain sensing system, we have applied it to real tissue. We sutured the sensor onto a fresh *ex-vivo* porcine bladder (Figure 4). The bladder including the complete sensor was placed in water to simulate the body fluid environment. Water (200 mL) was pumped into the bladder through a tube inserted into the urethra and released passively via the same tube. The resonance frequency was monitored continuously from outside the bath with the wireless readout. One exemplary filling and release cycle is shown in Figure 4a. The measured resonance frequency was translated to a strain (ϵ) according to the rearranged Equation (3)

$$\epsilon = \frac{f_0^2}{f^2} - 1 \quad (4)$$

and the bladder filling was estimated by assuming a homogenous extension of an ellipsoid as

$$V_{estimated} = \frac{4}{3}\pi(r_0 + r_0\epsilon)^2(h_0 + h_0\epsilon) \quad (5)$$

with $r_0 = \frac{U_{h_0}}{2\pi}$ and $h_0 = \frac{U_{v_0}}{\pi} - r_0$. The horizontal and vertical bladder circumferences were measured at rest as $U_{h_0}=140$ mm and $U_{v_0}=210$ mm. Filling the bladder led to an initial unfolding to around 95 mL, followed by expansion. At full expansion, the filling level dropped slightly due to the internal pressure, causing water flowing back into the tubing system and a small hysteresis due to the fast filling speed (Figure S4b, Supporting Information). For normal bladder filling speeds, the sensor exhibited a highly stable response. Finally, passive bladder voiding led to a decrease in bladder volume. The sensor returned to its original state after complete active voiding. Figure 4b shows the estimated volume as the function of the injected volume during the filling process. In the initial phase, the bladder accommodated the liquid without strain by smoothening internal wrinkles that exist in the empty state. However, above a critical volume of about 95 mL, the bladder started stretching and a linear dependency was observed, indicating the minimal volume above which the sensor is able to provide a reliable feedback about the filling state of the bladder (Figure 4c).

3.3. Conclusions

We present a novel soft conductor with high cyclic stability and a strain sensor with a chipless wireless readout. This system allows wireless strain sensing at strains of up to 50% with a readout distance of up to several cm. In addition, the sensor element has a Young's modulus of 260 kPa, which allows direct interfacing to biological tissue without impairing its physiological extension and contraction. This has been demonstrated with a proof-of-principle measurement on an *ex-vivo* porcine bladder. The advantages of the novel Au-TiO₂ NW-DS composite are threefold: First, it is five times softer than the conventional stretchable conductors made of Sylgard 184. Second, no performance loss or irreversible damages were observed during 100% strain cycling. Third, all involved materials are biocompatible. Additional advantages of the presented sensor are its simple structure and low cost, but importantly also that strain sensing is purely passive, thus not requiring an internal power source, which positively affects the sensor life-expectancy and avoids the requirement for hermetically sealed electronics. As such, regulatory and safety issues become much simpler. Overall, the presented materials and devices could enable continuous, wireless strain monitoring of various tissues and organs *in vivo*.

3.4. Experimental Section

Au-TiO₂ NW Synthesis: Adapted from Tybrandt et al.,^[29] TiO₂ NWs (ACS Material, TiO₂NW-A, length \approx 10 μ m, 0.6 mg), hydroxylamine (Sigma Aldrich, 50%, 244 μ L), and polyvinylpyrrolidone (Sigma Aldrich, MW 50 k, 1.32 g) were mixed with DI water to a final volume of 40 mL. Gold(III) chloride solution (Sigma Aldrich, Au 17 wt%, 244 μ L) was diluted in DI water to a final volume of 40 mL. The gold solution was added with a syringe pump into the TiO₂ NW solution under stirring (4 mL at 5.6 mL min⁻¹, then 36 mL at 2.8 mL min⁻¹). Hydrochloric acid (Sigma Aldrich, 37%, 2 mL) was added 5 min after completion. The solution was heated up under stirring to 80 °C for 15 min. After cooling down, dispersion was put through a 40 μ m sieve to remove eventual large aggregates. The final concentration amounted to 0.625 mg mL⁻¹.

Stretchable Conductors: For patterning Au-TiO₂ NW tracks (20 mm length, 0.5 mm width), a wax-assisted vacuum filtration method was used.^[28] Wax patterns were printed on hydrophilic polyvinylidene fluoride (PVDF) membranes (0.22 μ m pore size, Millipore) with a Xerox ColorQube 8570N wax printer (pure black, photo quality). Au-TiO₂ NW (5 mL) was dispersed in 20 mL DI water and filtered through the presoaked membrane. The Au-TiO₂ NW deposited on the membrane that was subsequently dried on a hotplate at 45 °C for 5 min. The Au-TiO₂ NW was consecutively washed and dried on the membrane by filtering phosphate buffered saline (PBS) followed by DI water, resulting in a surface coverage of the Au-TiO₂ NW pattern of 1.56 mg/cm². DS (Dragon Skin 10 slow cure, Smooth-On) was spin coated on a silanized wafer with 4000 rpm for 30 s. After 2 min at room temperature, the Au-TiO₂ NW was transferred from the PVDF membrane onto the semicured DS by gently placing the membrane in contact with it. The wafer was placed on a hotplate at 75 °C for 6 min with a weight (1 kg) on top. Afterward, the PVDF membrane was peeled off, leaving the Au-TiO₂ NW on the DS. A diluted DS solution (DS:heptane 1:20) was spin coated (6000 rpm, 30 s) to reinforce the contact pads and cured (75 °C, 3 min). A 25 μ m polyethylene naphthalate (PEN) foil (Teonex Q51) was used to mask the contact pads, and a layer of PDMS was spin coated on top (4000 rpm, 30 s). The PEN foil was removed, and the samples were cured (80 °C, 16 h). The samples were clamped in a tensile testing machine (DO-FB0.5TS, Zwick/Roell) with copper tape and liquid metal (eutectic indium gallium, Sigma Aldrich) as contacts. A digital multimeter (Agilent 34401A) was used to measure the resistance at 10 Hz. The samples were stretched at a rate of 5 mm s⁻¹.

Stretchable Capacitor and RLC Circuit: The plate capacitor was fabricated by multilayer stacking. For the first layer, DS was spin coated (1500 rpm, 30 s) and Au-TiO₂ NW was transferred as described above. In all subsequent steps, 25 μ m PEN foil (Teonex Q51) was used to mask the contact pads and was removed each time after spin coating. A diluted DS solution (DS:heptane 1:2) was spin coated (8000 rpm, 30 s) to cover the first layer and was cured on a hotplate at 75 °C for 3 min. A third layer of diluted DS (DS:heptane 2:1) with a different ratio DS–heptane ratio was spin coated (8000 rpm,

30 s) to transfer the second layer of Au-TiO₂ NW. Finally, pure DS was spin coated (1500 rpm, 30 s) to cover the sample with the final layer. Then, the sample was cured on the hotplate at 75 °C overnight. To complete the RLC resonant circuit, a coil inductor was bonded to the capacitor using conductive epoxy (EPO-TEK H20E), and the contacts were encapsulated with a silicone sealant (734 Flowable Sealant, Dow Corning). A tensile testing machine (DO-FB0.5TS, Zwick/ Roell) was employed to stretch the sensor from 0% to 50% strain at 0.015 mm s⁻¹ during sensor readout and 5 mm s⁻¹ during fatigue cycling. The resonance frequency of the sensor was recorded continuously during the stretching test at a measurement rate of 1.25 Hz. The mechanical modulus test was conducted with a strain rate of 2 mm s⁻¹.

Readout System: The resonance frequency of the sensor was readout by measuring the VSWR, swept over a frequency range, of the inductively coupled sensor and readout coil with a portable Arduino-based network analyser. The distance between the coils was kept constant at ≈ 1 cm.

Ex-Vivo Porcine Bladder Test: The two ends of the sensor were sutured (Ethicon Sutures, 8807H) on a fresh porcine bladder along the vertical circumference. A tube was inserted through the sphincter into the bladder, which was placed in a PBS bath. PBS was injected and controlled by a pump, a flowmeter, and an Arduino. After filling, the bladder was emptied passively and finally actively to eject the remaining fluid through a valve.

3.5. References

- [1] H. Han, A. M. Reichmuth, A. F. Renz, F. Stauffer, M. Thielen, J. Vörös, *Int. J. Autom. Smart Technol.* 2017, 7, 37.
- [2] S. P. Lacour, G. Courtine, J. Guck, *Nat. Rev. Mater.* 2016, 1, 16063.
- [3] P. Cai, W. R. Leow, X. Wang, Y.-L. Wu, X. Chen, *Adv. Mater.* 2017, 29.
- [4] J. Groen, J. Pannek, D. Castro Diaz, G. Del Popolo, T. Gross, R. Hamid, G. Karsenty, T. M. Kessler, M. Schneider, L. 't Hoen, B. Blok, *Eur. Urol.* 2016, 69, 324.
- [5] L. A. Simpson, J. J. Eng, J. T. C. Hsieh, D. L. Wolfe, *J. Neurotrauma* 2012, 29, 1548.
- [6] J. N. Panicker, C. J. Fowler, T. M. Kessler, *Lancet Neurol.* 2015, 14, 720.
- [7] M. N. Dakurah, C. Koo, W. Choi, Y. H. Joung, *Int. Neurourol. J.* 2015, 19, 133.
- [8] A. Gammie, B. Clarkson, C. Constantinou, M. Damaser, M. Drinnan, G. Geleijnse, D. Griffiths, P. Rosier, W. Schäfer, R. Van Mastriegt, *Neurourol. Urodyn.* 2014, 33, 370.
- [9] S. Rajagopalan, M. Sawan, E. Ghafar-Zadeh, O. Savadogo, V. P. Chodavarapu, *Sensors* 2008, 8, 5081.
- [10] C. A. Gutierrez, E. Meng, *J. Micromech. Microeng.* 2010, 20, 095028.
- [11] H. Cao, U. Tata, V. Landge, A. L. Li, Y. B. Peng, J. C. Chiao, in *2013 IEEE Topical Conference on Biomedical Wireless Technologies, Networks, and Sensing Systems*, 2013, pp. 34–36.
- [12] Q. A. Huang, L. Dong, L. F. Wang, *J. Microelectromech. Syst.* 2016, 25, 822.
- [13] M. A. Fonseca, M. G. Allen, J. Kroh, J. White, *Technical Digest of the Solid-State Sensor, Actuator, and Microsystems Workshop*, Hilton Head, 2006, pp. 38–42.
- [14] X. Yu, B. K. Mahajan, W. Shou, H. Pan, *Micromachines* 2016, 8, 7.
- [15] Y. Liu, K. He, G. Chen, W. R. Leow, X. Chen, *Chem. Rev.* 2017, 117, 12893.
- [16] T. Q. Trung, N.-E. Lee, *Adv. Mater.* 2017, 29.
- [17] D. McCoul, W. Hu, M. Gao, V. Mehta, Q. Pei, *Adv. Electron. Mater.* 2016, 2.
- [18] V. Martinez, F. Stauffer, M. O. Adagunodo, C. Forro, J. Vörös, A. Larmagnac, *ACS Appl. Mater. Interfaces* 2015, 7, 13467.
- [19] M. Amjadi, K. U. Kyung, I. Park, M. Sitti, *Adv. Funct. Mater.* 2016, 26, 1678.
- [20] J.-S. Noh, *Polymers* 2016, 8, 123.
- [21] Z. Liu, D. Qi, G. Hu, H. Wang, Y. Jiang, G. Chen, Y. Luo, X. J. Loh, B. Liedberg, X. Chen, *Adv. Mater.* 2018, 30.
- [22] Y. Jiang, Z. Liu, N. Matsuhisa, D. Qi, W. R. Leow, H. Yang, J. Yu, G. Chen, Y. Liu, C. Wan, Z. Liu, X. Chen, *Adv. Mater.* 2018.
- [23] K. Scholten, E. Meng, *Lab Chip* 2015, 15, 4256.
- [24] M. D. Dickey, *Adv. Mater.* 2017.
- [25] A. Hirsch, H. O. Michaud, A. P. Gerratt, S. de Mulatier, S. P. Lacour, *Adv. Mater.* 2016, 28, 4507.
- [26] D. J. Chew, L. Zhu, E. Delivopoulos, I. R. Mineev, K. M. Musick, C. a. Mosse, M. Craggs, N. Donaldson, S. P. Lacour, S. B. McMahon, J. W. Fawcett, *Sci. Transl. Med.* 2013, 5, 210ra155.
- [27] F. Xu, Y. Zhu, *Adv. Mater.* 2012, 24, 5117.
- [28] K. Tybrandt, J. Vörös, *Small* 2016, 12, 180.
- [29] K. Tybrandt, D. Khodagholy, B. Dielacher, F. Stauffer, A. F. Renz, G. Buzsáki, J. Vörös, *Adv. Mater.* 2018.
- [30] M. K. Shin, J. Oh, M. Lima, M. E. Kozlov, S. J. Kim, R. H. Baughman, *Adv. Mater.* 2010, 22, 2663.
- [31] T. A. Kim, H. S. Kim, S. S. Lee, M. Park, *Carbon N. Y.* 2012, 50, 444.
- [32] A. Larmagnac, S. Eggenberger, H. Janossy, J. Vörös, *Sci. Rep.* 2014, 4, 7254.

[33] W. F. Boron, *Medical Physiology*, Elsevier, 2016.

[34] C. Li, G. Guan, F. Zhang, S. Song, R. K. Wang, Z. Huang, G. Nabi, *Biomed. Opt. Express* 2014, 5, 4313.

Chapter 4: A Stretchable Strain Sensor System for Wireless Measurement of Musculoskeletal Soft Tissue Strains

Qiang Zhang¹, Fransiska M. Bossuyt², Naomi C. Adam¹, Byron Llerena Zambrano³, Flurin Stauffer³, Janos Vörös³, Roland Küng⁴, Sarah Abramovic¹, Vullnet Useini¹, Walter Herzog², Tim Leonard², Michael W. Scott⁵, William R. Taylor^{1*}, Colin R. Smith¹

¹Institute for Biomechanics, ETH Zürich, Switzerland

²Human Performance Lab, University of Calgary, Canada

³Laboratory of Biosensors and Bioelectronics, ETH Zürich, Switzerland

⁴Center for Communications Systems, School of Engineering, Zürich University of Applied Sciences

⁵Faculty of Veterinary Medicine, University of Calgary, Canada

In preparation to be submitted to *Advanced Materials Technologies*.

Abstract

Measurement of *in-vivo* strain patterns of musculoskeletal soft tissues (MST) during functional activities can reveal their biomechanical function, support identification and understanding their pathologies, and quantify tissue adaptation during healing. These critical scientific and clinical insights have motivated the development and application of various strain sensors to quantify MST strains in either intraoperative or dynamic *in-vivo* scenarios. In this study, a passive biocompatible strain sensor system was developed based on stretchable electronics and radio frequency identification technologies. In this system, a flexible inductor-capacitor-resistor sensor was fabricated and was excited by a custom-designed readout box through electronic resonance at a specific frequency. The resonant frequency (RF) of the sensor changes when the capacitor is stretched, which is recorded by the readout box at a high sampling rate (1 kHz). Suturing the stretchable capacitor onto the surface of the MST allows it to be stretched in line with musculoskeletal deformations, hence providing an indirect method to assess the MST strain patterns. The signal remained linear between 0 and 25% strain and was electronically stable in a simulated *in-vivo* environment for one week and over 100'000 cycles of fatigue loadings. The strain sensor had outstanding resolution (0.1% strain, $\approx 9 \mu\text{m}$) during wireless strain measurement in all conditions. *Ex-vivo* tensile tendon testing demonstrated that the sensor could provide accurate strain measurement in a sheep plantaris tendon. *In-vivo* sensor implantation and strain measurement indicated that the sensor was able to record the repetitive strain patterns in the medial gastrocnemius tendon of a sheep during trotting. This study indicates the applicability of the sensor system for studying the biomechanical function of MST *in vivo*.

Keywords: Biosensors, Stretchable electronics, Soft tissue strains, Tissue loadings, Musculoskeletal biomechanics

4.1. Introduction

Musculoskeletal soft tissues (MSTs), such as ligaments and tendons, play principal roles in absorbing external impacts [1], stabilizing joints [2], and providing joint proprioception [3]. Injuries to MSTs can limit musculoskeletal function and initiate tendinopathy and osteoarthritis in neighbouring tissues, and thus permanently impact quality of life [4-6]. Successful treatment of MST injuries relies on a comprehensive understanding of the functional demands of MSTs during dynamic activities and the healing and pathologic adaptive response of a tissue to loading. Quantification of *in-vivo* tendon strains have revealed the complex interactions within muscle-tendon units that transmit energy from muscle contraction, amplify power output, and absorb shocks during impact [7, 8]. Measurements of *in-vivo* ligament strains during various activities have supported the optimization of rehabilitation protocols to stimulate anterior cruciate ligament healing and avoid damage [9, 10], and aided in the evaluation of the effects of total knee arthroplasty techniques and component designs on soft tissue loadings and pathological adaptations [11, 12]. The quantification *in-vivo* MST strains are therefore critical for both facilitating scientific discoveries on tissue function and driving innovative clinical treatments. Implantable strain sensors can be physically attached to the ligament and tendon to convert deformation of the tissue into sensor electrical signals [13], and thus enable *in-vivo* strains to be measured in humans with high accuracy and sampling rates [13-15]. Current tendon strain sensor designs aim towards a revolutionary technology that provides sufficient robustness, minimal tissue disruption, wireless data transmission, and long-term biocompatibility, in order to withstand the demands of *in-vivo* MST strain measurements during dynamic activities including repeated and rapid tissue deformations (i.e., strain rates up to 50%/s in Achilles' tendons [16]), and minimize risk to subjects.

Various implantable sensors have been used to measure MST strains *in vivo*, but previous measurements in human have almost exclusively been limited to intraoperative environments and widespread application of strain sensors in patients has not been achieved due to limitations in sensor designs. As an example, magnetic field sensors, such as Hall effect strain transducers and differential variable reluctance transducers, have been implanted onto the ACL of human subjects to measure ACL strains throughout a variety of movements such as squatting and bicycling [10, 17]. However, there are several disadvantages that limit these sensor designs for *in-vivo* MST strain measurements. First, the rigid construction of these sensors led to sensor impingement with neighbouring musculoskeletal tissues, which limits the tissues and postures that can be measured [15]. Second, the fixation methods adopted by these sensors are sub-optimal for dynamic measurements of MST strains. Magnetic field sensors can be fixed through pressing two barbs of the sensor into the tissue [18, 19], but the security of the fixation during dynamic measurements may be weak. Finally, it is important to note that these sensors require a cable to transmit the measurement signal [18, 20, 21], and thus an transcutaneous incision limiting the applicability to both human and animal experiments. Furthermore, bending of the cable can induce

artefacts in the sensor signal [22]. Thus, many clinically important MST strain measurements that could advance orthopaedic treatments would become possible through a novel sensor technology that enables long-term dynamic *in-vivo* measurements.

Recent advances in stretchable electronics have facilitated the development of membrane-like stretchable strain sensors with great potential for clinical application through their unique soft constitutions that can easily conform to the surface morphologies of tissues and thus minimize sensor impingement. These sensors have shown outstanding conductivity, stretchability, and durability [23-25], and have been used to track human body movements [26-30], measure human bladder volume, and monitor heart rate [31-33]. These sensors are typically fabricated by embedding conductive materials in stretchable elastomers, and can be generally classified into resistive-type sensors consisting of a single conductive layer [28, 30, 34] or capacitive-type sensors with two conductive layers [29, 33, 35]. In a capacitive-type sensor, the capacitance increases upon stretching due to thinning of the dielectric layer and shape variation of the overlapping area [36, 37]. The capacitive-type sensor has low hysteresis, less overshoot, and higher linearity in its electromechanical response compared to the resistive-type sensor [36, 38, 39]. Despite the disruptive technology in implantable strain sensors, to our knowledge, very few stretchable strain sensors have been employed to quantify MST strains [40, 41]. Zens and co-workers used a capacitive-type sensor to measure anterolateral ligament strains on a knee specimen [41]. Boutry and co-workers developed a biodegradable sensor that enables the monitoring of long-term MST strains [42]. However, the sensors were glued on the tissues during measurement, which may lead to tissue damage and biocompatibility issues. There is also a lack of a full demonstration of these elastomer-based strain sensors on the ability to endure long-term and high-rate fatigue loadings. Importantly, the sensor techniques of both research groups failed to incorporate wireless data transmission across the skin, which can be realized through wireless sensors that use on-board batteries [43, 44], Near Field Communication technology [32], or antenna coils [33, 36, 45].

In this study, we introduce an advanced stretchable sensor system with calibration methodology and provide a comprehensive demonstration of the strain measurement capacity in both *ex-vivo* and simulated *in-vivo* conditions. In our sensor, the stretchable capacitor has been used for wireless signal transmission by simply adding a coil to the capacitor to create a chipless inductor-capacitor-resistor (LCR) sensor that can be wirelessly powered and monitored via an external readout [33, 46]. Furthermore, we characterized the *in-vivo* function and biocompatibility of the sensor over an extended period of time. The system consists of a chipless and flexible stretchable sensor that is designed to be directly sutured onto MSTs in the body, a novel wearable readout that can wirelessly power and measure the sensor signal from the outside of the body, and an ios app that controls the system and displays sensor data in real-time. The system can simultaneously measure multiple sensors attached to different tissues, meaning that it can quantify the coordinated function of multiple passive tissues in a joint. The sensor has outstanding resolution for wireless strain measurement (0.1% strain, $\approx 9 \mu\text{m}$), and remains

reliable over 100'000 cycles of fatigue loadings. We performed *ex-vivo* sensor measurements on a sheep plantaris tendon to illustrate the potential of the sensor system for dynamically quantifying the strain of soft tissues. *In-vivo* sensor implantation in a sheep and strain measurement on the medial gastrocnemius tendon demonstrate the applicability of the sensor system for characterizing *in-vivo* function of soft tissues during locomotion. Finally, the sensor was demonstrated to be biocompatible after implantation in a sheep for two months.

4.2. Results and Discussion

4.2.1. Sensor design and properties

The strain sensor system consists of an implantable strain sensor and a portable readout box (Figure 1b and 1d). The sensor has a stretchable capacitor containing two layers of conductive gold titanium dioxide nanowires (Au-TiO₂ NW) separated by a layer of dielectric silicone rubber, resembling a membrane-like “sandwich” structure that is embedded in biocompatible polydimethylsiloxane (PDMS) (Figure 1d, 1e, and 1f). The capacitor is bonded to a coil inductor to form a LCR circuit, which is then casted in PDMS to construct the whole sensor. Based on induction coupling of the antennas [33, 47], the readout box can wirelessly excite the strain sensor from a distance up to 10 cm so that currents are initialized in the sensor and oscillate at a certain resonant frequency (RF). The RF of the sensor is dependent to the capacitance of the capacitor, and the capacitance varies with the length change of the capacitor [33]. Therefore, once the capacitor is fixed onto a MST, the strain in the MST can be quantified by using the readout box to wirelessly measure the RF of the sensor at a sampling rate of 1000 Hz. Without the need of a cable across the skin (Figure 1a), the high-rate wireless sensing function of the sensor system allow it to track the strain in MSTs during dynamic body movements because the skin incision for sensor implantation can well heal and potential interruptions from the cable immigration on the signal quality can be fully mitigated.

As the sensing component of the sensor, the stretchable capacitor demonstrated excellent electronic performance during tensile tests. The capacitance increased with high linearity ($R^2 > 0.99$) under axial strains from 5 to 20 % (Figure S1; Supplementary S1). The capacitor also had outstanding resolution, detecting strains down to 0.1 % ($\approx 9\mu\text{m}$). Moreover, the linearity and resolution of the capacitor remained unchanged after 100'000 cyclic loadings (Figure S1), suggesting that the capacitor maintained its structural and functional integrity without irreversible damage from material fatigue. These results indicate that the stretchable capacitor will unlikely exhibit performance loss while suffering highly repetitive loadings during long-period *in-vivo* dynamic measurements. To ensure accurate measurement of strains in the MST, we decided to stitch the sensor on the tissue using surgical sutures because it can provide a secure fixation without significantly affecting the native function of the MST. To prevent the damage on the soft component, two rigid suturing pads were fabricated and fixed on the capacitor. A custom-designed pre-strain device (Figure 1c) can hold the sensor at a custom-defined pre-strain level during suturing, allowing measurements of both elongation and shortening of the MST during movements.

Simultaneous measurement of multiple sensors is enabled by internally synchronizing different readout boxes with time packets sent from a “master” readout box to nearby “slave” readout boxes over Bluetooth (Figure S2). This function allows quantification of the concurrent strains in multiple MSTs

or different bundles of a MST, enabling the investigation of the coordination of multiple MSTs during dynamic movements. Moreover, the sensor system can be synchronized to other measurement devices (e.g., motion capture system and inertial measurement units) with a custom-designed sync box that can send and record digital and analog sync pulses (Figure S2). The sensor system is controlled by an iPad-based app through Bluetooth connection (Figure S2). The received data can be transmitted to the iPad for a Fast Fourier Transformation (FFT, 512 points) to display the real-time RF of each sensor or stored on a SD card for offline data analysis (Figure S2; Supplementary S2).

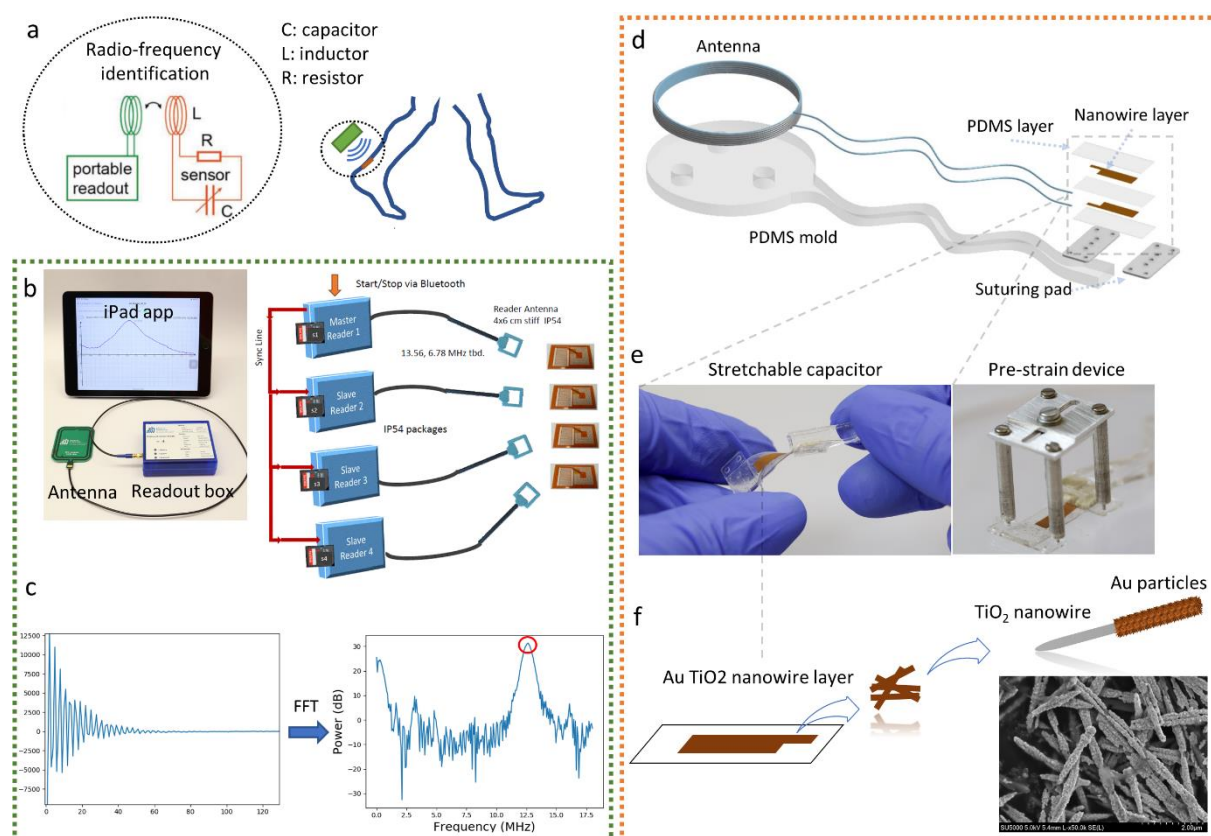


Figure 1. Wireless sensor technology for *in-vivo* measurement of musculoskeletal soft tissue strain. a) Scheme of *in-vivo* wireless strain measurement based on radio-frequency identification technology. b) Left: Sensor readout system including a readout box with antenna and an iPad app for controlling and displaying real-time sensor signal; Right: Synchronization of multiple readout boxes and start/stop control via Bluetooth. c) The raw data is processed with a FFT (512 points) to obtain the frequency resonant. d) Scheme of the stretchable strain sensor. e) Left: Stretchable capacitor; Right: Pre-strain device for pre-stretching the sensor during implantation so that the sensor can measure both tissue elongation and shortening. f) conductive layer patterned with Au-TiO₂ NW.

4.2.2. Wireless sensing performance

The wireless sensing performance of the sensor system was demonstrated to be excellent both in the air and in a simulated *in-vivo* condition. While the strain sensor was stretched to 25 %, its RF and Q-factor were measured (Fig. 2a). Because the macroscopic failures of MSTs occur at around strains of 8-15 % [48-51], 25 % of strain range ensured sufficient characterization of the sensor behaviour for the strain measurement of MSTs. With increasing strain applied to the sensor, the RF decreased due to the increasing of capacitance (Fig. 2b). Meanwhile, the Q-factor decreased, which was mainly due to the increased series resistance of the nanowire layers in the capacitor [52, 53]. When repeated cycles were

performed in the tensile machine, the RF signal was highly repetitive (Fig. 2c), suggesting that the sensor had little viscous mechanical behaviour.

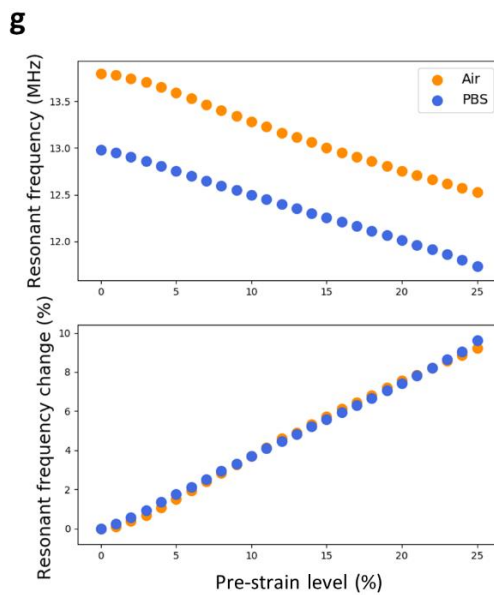
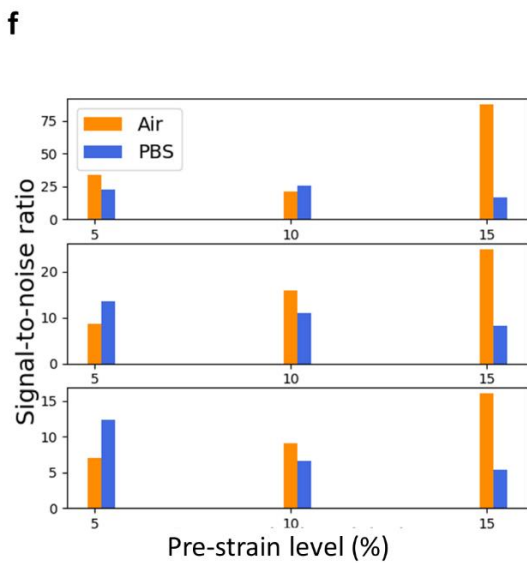
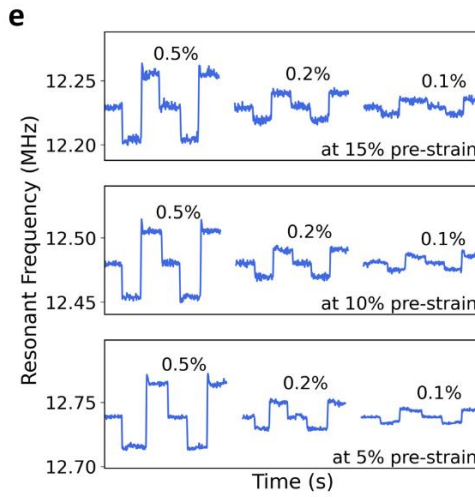
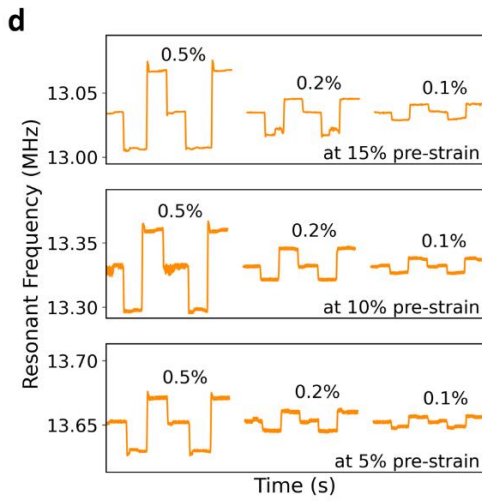
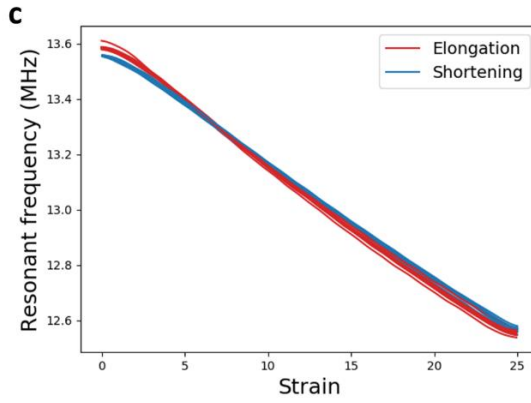
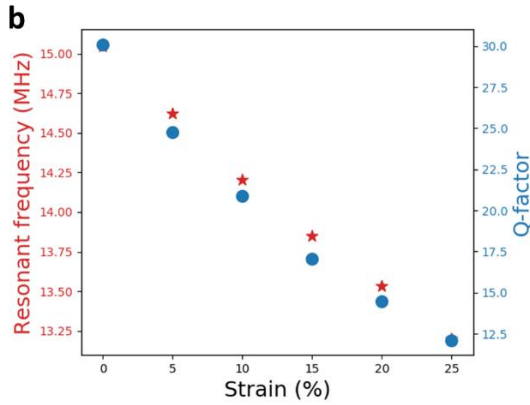
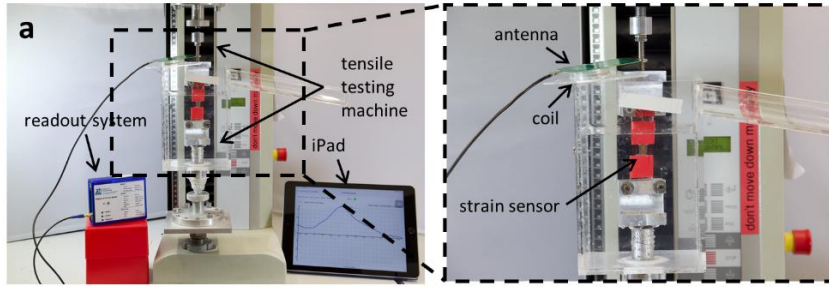


Figure 2. Wireless measurement performance of the strain sensor. a) Experimental setup for wireless measurements with zoom in: tensile testing machine with strain sensor, readout box and iPad. b) Changes of sensor resonant frequency and Q -factor against strains from 0 to 25%. c) Low hysteresis effect of the sensor under cyclic loadings. d) Two out of ten cycles of $\pm 0.5%$, $\pm 0.2%$, and $\pm 0.1%$ strain steps at different pre-strain levels in air condition. e) Two out of ten cycles of $\pm 0.5%$, $\pm 0.2%$, and $\pm 0.1%$ strain steps at different pre-strain levels in PBS condition. f) Corresponding signal to noise ratio SNR for both air and PBS conditions. g) The absolute (upper) and relative (down) resonant frequency changes with strains from 0% to 25% in air and PBS conditions

Good resolution in wireless sensing is considered to be an important prerequisite of biomechanical applications to the sensor system [14, 15, 54]. In this study, it was demonstrated that the sensor system has an excellent resolution in wireless strain sensing, both in air and in phosphate buffered saline (PBS). For the test in air, 0.1 % strain ($\approx 9 \mu\text{m}$) led to an observable change in the RF of the sensor (Fig. 2d), indicating that even a small strain in the sensor perturbed the RF signal, and the variation was able to be detected by the readout box. The test in PBS aimed to simulate the *in-vivo* environment and demonstrated a similar resolution of the sensor system as the test in air (Fig. 2e). Strain sensors that adapted wired data transmissions were reported to have good signal resolution [40, 41, 54]. For wireless data transmission, good signal resolution can be achieved by using active sensors with internal power sources to send reinforced signal [43]. In this study, the strain sensor was made chipless and implemented passive data transmission, in order to simplify its structure for *in-vivo* implantation and extend life-expectancy. Nevertheless, the sensor system achieved a similar good resolution, indicating its advances compared to previous technologies.

As the sensor will be surgically fixed at an unknown length during implantation, the effect of sensor pre-strain levels on the resolution of the sensor system was studied by comparing the signal to noise ratio (SNR). A small SNR may affect the ability of the sensor system in characterizing small strain variations. Overall, no clear relationship was found between the pre-strain level and the SNR of the sensor system. In air, the sensor had a larger SNR at 15 % pre-strain level compared to 10 % and 5 %. In PBS, however, the sensor signal was slightly noisier at higher pre-strain levels, where the SNR was smaller at 15 % pre-strain compared to 10 % and 5 % pre-strains (Fig. 2f). However, because of the low correlation between the pre-strain level and sensor SNR, the sensor may be freely implanted at any pre-strain level from 5 to 15 % strains. Finally, regardless of the testing conditions, small overshoots were observed while 0.5 % strains were applied (Fig. 2d&2e). The overshoot behaviour can be explained by stress relaxation of polymers and friction between the solid nanowires and polymer molecules [23, 39, 55, 56]. In this study, the signal overshoot was not observed at smaller strain steps (0.1 % and 0.2 %), suggesting that the magnitude of overshoot may be dependent to the level of strain step applied to the sensor. The relationship between overshoot and strain was also observed in another study, where Rahimi and co-workers found that their stretchable resistor showed larger overshoot at strains over 50 % compared to lower strains [57].

The sensor RF signal was measured during stepwise loadings, both in air and in PBS. For the test in air, the RF of the sensor gradually decreased from 13.80 to 12.53 MHz with strain increasing from 0 to 25 % (Fig. 2g). When the sensor was submerged in PBS, the RF of the sensor at 0% strain

decreased to 12.98 MHz, and the RF of the sensor decreased to 11.73 MHz at 25 % strain. Moreover, the relative change of the sensor RF was similar in both conditions, achieving a similar average gauge factor of 0.38 (Fig. 2g). This finding is important for *in-vivo* strain measurements. Before implantation, the sensor needs to be calibrated to axial strain. However, the calibrated sensor will be inaccurate in strain quantification if the gauge factor of the sensor changed in the living body. According to our results, the gauge factor of our strain sensor remained unchanged when the test was shifted from air to PBS, indicating that for future *in-vivo* measurement, the calibration performed outside can be used to convert the *in-vivo* RF signals to the strain results. This further demonstrated the applicability of our sensor system for *in-vivo* strain measurements.

4.2.3. Ex-vivo testing

The wireless sensing properties of the sensor system was tested in a simulated *in-vivo* environment (PBS, 37 °C) for 1 week, in order to evaluate its change in a living body. As shown in Fig. 3a, the RF of the sensor decreased ~1 MHz one day after being immersed in PBS. Meanwhile, the Q-factor of the sensor significantly decreased on the first day from 35.9 to 18.7. These changes might be mainly due to the increased capacitance of the capacitor caused by PBS absorption, which was also reported in previous studies [58]. PBS absorption by the PDMS increased the parasitic capacitance between nanowire electrode and electrolyte through the PDMS [59]. Importantly, the RF and Q-factor of the sensor reached a plateau one day after the sensor was immersed, suggesting that the signal of the sensor could be stable during a longer period of time in the living body. In addition, the temperature in the living body slightly changes [60] during body movement, and therefore we evaluated the effect on the wireless sensing properties of the sensor system. As shown in Fig. 3b, the RF of the sensor increased from 13.863 to 14.025 MHz from 22 to 45 °C in a linear relationship. Within the possible temperature range of 38-40 °C in the mammal body, the RF of the sensor was only changed by 0.011MHz. Such a temperature-induced variation only accounts for a small error of 0.2% to the strain measurement, which can be greatly mitigated by *in-vivo* pre-conditioning (i.e., warm-up walking) before measurement.

The applicability of the LCR sensor for *in-vivo* strain measurements of MSTs was tested with *ex-vivo* tensile testing using cyclic loading of a cadaveric sheep plantaris tendon in a tensile testing machine (Fig. 3c). As shown in Fig. 3d, the sensor system successfully recorded continuous repetitive strain variations during cyclic loading. Following calibration of RF to the length changes measured with sonomicrometry crystals located underneath the sensor, the RF variations accounted for an average 4.2% strain in the tendon throughout the 51 cycles of loadings (Figure 3d). When comparing these results to the tensile testing machine, the sensor system measured a slightly larger strain in the tendon. It should be noted that the tensile testing machine measures the overall length changes of the tendon, while the sensor measures a region that covers part of the tendon near the lower clamping site. It was reported that the strain in the upper and lower clamping sites were commonly larger than the overall strain in the

tendon [61]. Therefore, the results might reflect the native mechanical property of the tendon. Overall, the *ex-vitro* tensile test demonstrated that the sensor system could accurately record the strains in the tendon during cyclic loadings, indicating great potentials of the sensor system to quantify strains in MSTs *in vivo*.

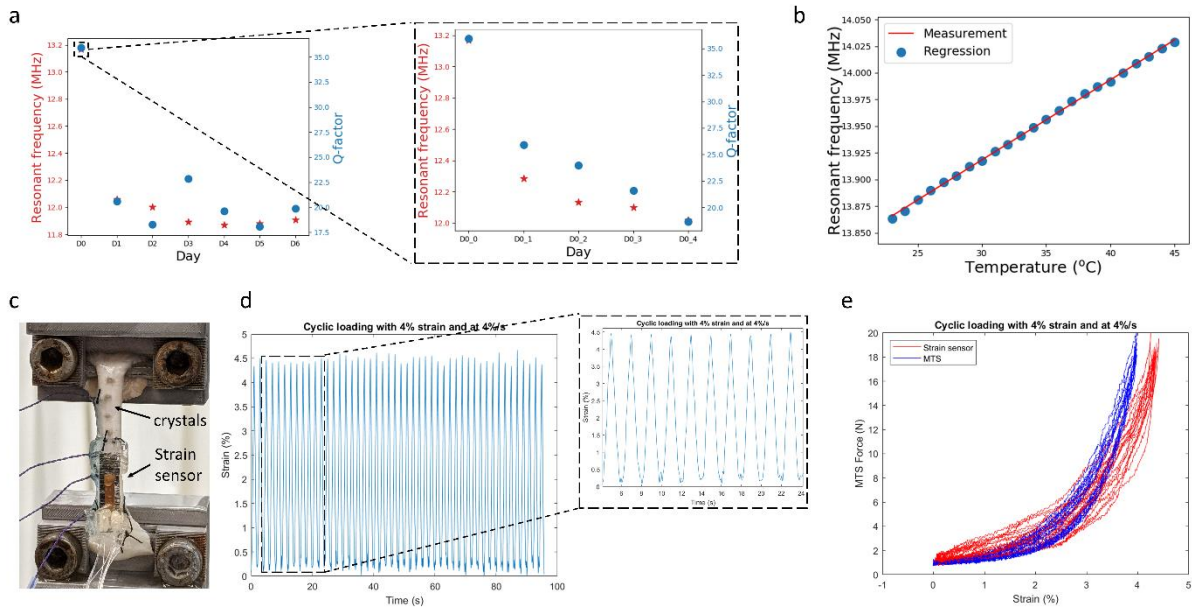


Figure 3. *Ex-vitro* validation and measurements of LCR sensor. a) Left: changes of sensor resonant frequency and *Q*-factor in a simulated *in-vivo* condition; right: change of sensor signal in the first 5 hours. b) Linear increasing of the sensor resonant frequency with temperature increasing from 23 to 45 degree. c) *Ex-vitro* strain measurement of sheep plantaris tendon. d) repetitive change of sensor resonant frequency during 51 cycles of loadings. e) tendon strains assessed by the sensor compared to the results of tensile testing machine.

4.2.4. *In-vivo* sensor implantation in sheep and dynamic measurement of medial gastrocnemius tendon biomechanics

A first proof-of-concept *in-vivo* tendon strain measurements during dynamic movements was conducted by implanting a calibrated strain sensor on the medial gastrocnemius tendon of a sheep. In addition, a custom-made “E”-shaped buckle-type force transducer [62] was implanted on the same tendon to measure the muscle forces of the medial gastrocnemius impacted onto the tendon. Two hours following implantation, the sheep was weight bearing on the instrumented leg, and no significant signs of limping was observed during the following days. Three days after the surgery, the sheep was guided to perform a trotting test on the treadmill, during which continuous strain and force measurements were completed (Fig. 4). A maximum strain of 3.8 % was observed during the stance phase of the trotting cycle at 1.34 m/s. Although no previous study has measured *in-vivo* strains in the medial gastrocnemius tendon of sheep during walking, maximum tendon strains were estimated to be 2.6 % in lateral digital extensor tendon of sheep when trotting [63]; 1.8 % in deep digital flexor tendon of horse hindlimb when trotting at 1.8-4.8 m/s [64], 8.49 % in superficial digital flexor tendon and 5.39 % in deep digital flexor tendon of horse forelimb when trotting at 3.9 m/s [65], and 4.15 % in superficial digital flexor tendon and 1.7%

in deep digital flexor tendon of horse forelimb when trotting [66]. Thus, the strain values measured in this study are well within the range observed in previous studies.

The ability of our sensor system to perform *in-vivo* measurements of MST strains shows great potential to address important biomechanical questions. First, the sensor system provides *in-vivo* strain results, which can be used to validate the results of modelling simulations and optimize the musculoskeletal models. Indirect strain measurement using image-based methods result in largely varied strains in MSTs. Thus, measurement using our sensor system can be a gold-standard to verify the accuracy of the indirect measurement methods. Finally, the sensor allows researchers to monitor strains in the MSTs during dynamic movements, which can provide informative results regarding the functionalities and pathological mechanisms of MSTs.

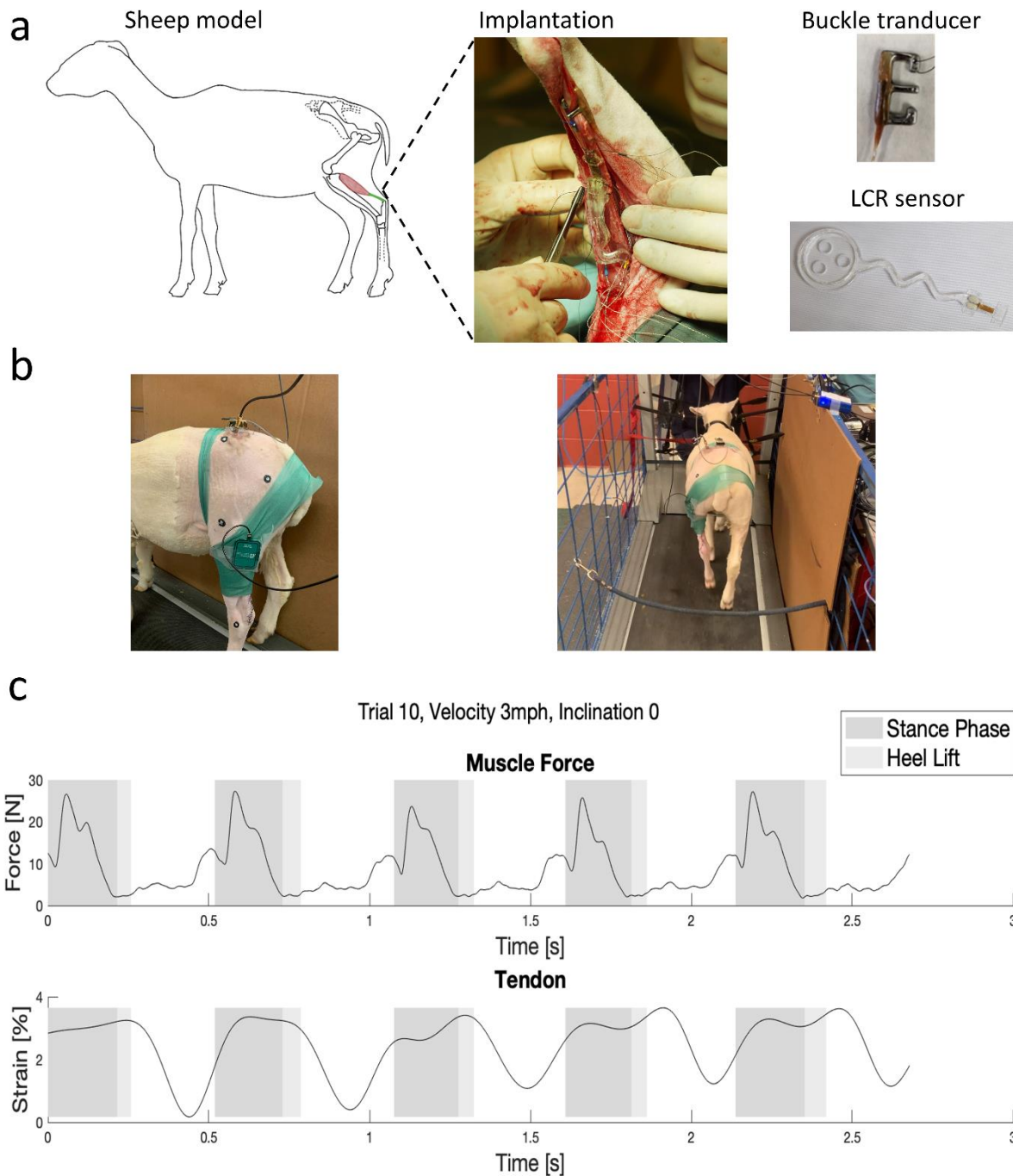


Figure 4. In-vivo sensor implantation and strain measurement. a) implantation site and devices. b) Experiment schedule. c) The force and strain of sheep Achilles' tendon during trotting.

Several limitations of the sensor system need to be addressed to improve its applicability for *in-vivo* research and clinical applications. First, the overall size of the sensor, especially the inductive coil, should be further miniaturized. Although the current design did not affect sheep movement, a smaller sensor will facilitate tissue healing and avoid serious impingements with surrounding tissues in the body. In addition, the LCR sensor was out of function after being extracted from the sheep body due to the wires cutting through the PDMS coating. Therefore, further sensors need to be more hermetically sealed by PDMS during fabrication, in order to remain functional in the living body for a much longer period.

4.3. Conclusions

We developed and demonstrated a novel strain sensor and a wireless readout system with the ability to measure *in-vivo* soft tissue strains. The readout system wirelessly excites the sensor and records its signal at a distance up to 10 cm, enabling passive strain sensing of the chipless sensor without the need of an internal power supply. The sensor has an outstanding resolution that allows it to measure down to 9 μm axial strains in wireless strain sensing. In addition, the measurement reliability of the sensor is not affected after fatigue loadings are applied, suggesting that the sensor is reliable for long-term utilization. The sensor had outstanding applicability for strain sensing during *ex-vivo* tendon tensile tests. *In-vivo* sheep implantation and measurement were successful, suggesting that 1) the sensor can successfully measure tendon strain in living subjects; 2) Dynamic movement of the body does not affect the sensor integrity. Finally, the sensor was demonstrated to be biocompatible. Overall, the presented sensor and readout system could enable wireless strain measurement of tendons and ligaments *in vivo*.

4.4. Methods and Materials

4.4.1. Stretchable capacitor fabrication

The Au-TiO₂ NW in the capacitor was synthesized using a method adapted from Tybrandt et al. [67]. Au-TiO₂ NW tracks were patterned using a wax-assisted vacuum filtration method [33]. A wax printer (Xerox ColorQube 8570N, pure black, photo quality) was used to print wax patterns on hydrophilic polyvinylidene fluoride (PVDF) membranes (0.22 μm pore size, Millipore). 2ml Au-TiO₂ NW solution was filtered through the PVDF membrane, and then was dried on a hotplate at 45 °C for 10 mins. Afterwards, the deposited Au-TiO₂ NWs were rinsed in PBS. The surface coverage of the Au-TiO₂ NW pattern was 0.624 mg/cm². Then, PDMS (Sylgard 184, curing agent/ base weight ratio of 0.15/1) was spin-coated on a salinized wafer at 600 rpm for 30 s and dried on a hotplate at 75 °C for 7 mins. The PVDF membrane was placed on the PDMS with full contact. The wafer was then placed on a hotplate at 75 °C for 11 mins with a weight of 750g on top. Next, the PVDF membrane was peeled off, depositing the Au-TiO₂ NW on the PDMS. A 25 μm polyethylene naphthalate foil (Teonex Q51) was used to mask the contacts in the following steps of spin-coating. A diluted solution of Dragon Skin (DS) silicone rubber (Dragon Skin 10 SLOW, part A/part B weight ratio of 1/1) in heptane (DS/heptane weight ratio of 1/2) was spin-coated (6000 rpm, 30 s) on the Au-TiO₂ NW and cured on a hotplate at 75 °C for 60 mins. Afterwards, a second layer of diluted DS-heptane solution (DS/heptane weight ratio of 2/1) was spin-coated (6000 rpm, 30 s), and a second layer of Au-TiO₂ NW was transferred on top and then cured on a hotplate at 75 °C for 60 mins. Finally, PDMS was spin-coated (600 rpm, 30 s) to insulate the Au-TiO₂ NW, and the sample was cured on the hotplate at 75 °C overnight.

4.4.2. LCR sensor fabrication and readout system development

The coil inductor was fabricated by looping a wire (litz wire 7 × 0.04mm, Cu/Ag50, TW-0, Elektrisola) around a polymethyl methacrylate (PMMA) ring of 33mm in diameter. Then the inductor was bonded to the contact pads of the stretchable capacitor with PDMS-Ag composite (Ag powder: Sigma-Aldrich, length = 2-3.5 μm; Ag/PDMS volume ratio of 0.3/1 [68]). Due to the design of the readout box, the LCR sensor was fabricated towards a target RF of 14MHz for optimal wireless signal quality. In order to determine the number of turns in the coil, the inductance (L) of the coil inductor was calculated based on the target RF (f) and capacitance (C) of the capacitor according to:

$$f = \frac{1}{2\pi\sqrt{LC}}$$

The number of turns (N) was thus calculated according to:

$$L = \frac{\mu_r\mu_0 N^2 \pi r^2}{l}$$

Where μ_r is the relative permeability of the core (2.69 for PDMS); μ_0 is the permeability of free space ($4\pi \times 10^{-7}$ (H/m)); r is the coil radius; and l is the coil length.

Two PMMA pads (pad A: 12×13×2 mm; pad B: 12×8×2 mm) with four holes in the corners were fabricated using a laser cutter (Trotec Laser, Speedy 300) and bonded to each end of the capacitor with epoxy (UHU Plus Schnellfest Epoxikleber). A PMMA mold was fabricated using the laser cutter for casting the sensor exterior in PDMS. The coil inductor and connecting wires were placed in the mold, then the PDMS was poured and cured in an oven at 80 °C for 3 hours. Finally, a PMMA pad was fabricated using the laser cutter and bonded to the coil inductor with PDMS.

The wireless readout system was composed of a Class-E amplifier and a printed circuit board (PCB) antenna. For measurement, the readout system first charges the strain sensor for 20 μ s with a signal (stimulation frequency of 13.56 MHz; power of 22dBm) generated by the Class-E amplifier through the antenna. Then, the antenna was switched from transmit to receive function and during the next 10 μ s the electronic field of the LCR sensor was sampled. It then took the system 970 μ s to filter, amplify, and transform the signal from analog to digital. Therefore, one wireless measurement of the sensor RF requires 1 ms, resulting in 1024 Hz of sampling frequency.

4.4.3. Characterization of Stretchable Capacitor

The electromechanical properties of the stretchable capacitor were evaluated using a tensile testing machine (DO-FB0.5TS, Zwick/ Roell) and a LCR meter (Hioki, IM3536) as follows:

- 1) *Capacitor signal under stretching:* A stretchable capacitor was mounted on the tensile testing machine, and its original length (L_0) was determined by measuring the stretchable region after applying a minimal stretching force of 0.05 N. The L_0 was used to calculate the strain and strain rate (50 %/s for all tests) during subsequent tensile testing. The capacitor was positioned at 5 % pre-strain in a custom-designed tank and presoaked in PBS for 12 hours, and then was pre-conditioned from 5 to 20 % strains for 50 cycles. To test its sensitivity, the capacitor was stretched from 5 to 20 % with 0.5 % strain steps, with 30 s pause at each strain step. To test its resolution, the capacitor was stretched ± 0.1 % strains for 10 cycles at incrementing pre-strain levels from 5 to 20 % in 1 % strain steps.
- 2) *The effect of fatigue on capacitor signal:* After characterizing its sensitivity and resolution, 100'000 cycles of 5 to 20 % strains were applied to the capacitor, and then sensitivity and resolution tests were repeated.
- 3) *Effect of pressure on sensor signal:* A LCR sensor was placed in a petri dish filled with PBS 12 hours before the test. A compressive force (0-10 N, 0.5 N/s) was applied on the stretchable capacitor with a custom-designed plastic plunger mounted on the top clamp of the tensile testing machine to mimic neighbouring tissue impingement. The test was performed while the sensor was fixed at three different pre-strain levels: 0 %, 5 %, and 10 %.

4.4.4. Characterization of wireless LCR sensor

The wireless sensing capacity of LCR sensor was characterized based on the following experiments:

- 1) *Sensor electrical properties under stretching*: A LCR sensor was mounted on a custom-designed manual tensile testing device and stretched from 0 to 25 % strains. A miniVNA Tiny network analyzer (mRS RADIO SOLUTIONS) was used to quantify the electrical properties of the LCR sensor. The miniVNA coil was placed 1cm over the sensor's coil and a frequency sweep was carried out from 10 to 20 MHz. The RF of the sensor was measured as well as F_{high} (frequency where the absolute value of R_s is equal to Z_s) and F_{low} (frequency where the absolute value of R_s is equal to the opposite of Z_s). The Q factor of the LCR sensor was calculated as $Q = RF / (F_{high} - F_{low})$.
- 2) *Stability of sensor signal in a simulated in-vivo environment*: A LCR sensor was submerged in PBS at 37 °C in a custom-designed incubator and held at a fixed length for 7 days. Before submerging, the RF and Q factor of the sensor were measured as the baseline measurements. The sensor was then submerged in PBS and measured another 4 times on the first day, and then measured once per day. To test the effect of temperature across a range of *in-vivo* possibilities, a LCR sensor was submerged in PBS at room temperature for 12 hours prior to the experiment. Then, the PBS was heated from 22 to 45 °C on a hotplate over 30 minutes, using an electronic probe thermometer (DOSTMANN electronic) to track the temperature. Meanwhile, the RF of the sensor was continuously recorded.
- 3) *Sensor sensitivity and resolution*: A LCR sensor was mounted on the tensile testing machine. After 50 cycles of preconditioning from 0 to 20 % strains, the sensitivity (0-25 % strains, 1 % per step, 30 s pause) and resolution (levels: ±0.1 %, ±0.2 %, and ±0.5 %, pre-strains: 5 %, 10 %, and 15%, number of cycles: 10) tests were applied in two different conditions: 1) in air; 2) in PBS. The RF of the sensor was measured using the custom-designed readout system throughout the experiment.

4.4.5. Ex-vivo sensor measurements of ligament and tendon strains

A fresh frozen sheep plantaris tendon was mounted on a tensile testing machine (858 Mini Bionix II, MTS, Eden Prairie, MN, USA) by wrapping the ends of the tendon around cylindrical metal abrasive clamps (Figure 3c). The tendon was preloaded to 6.3 N ($0.272 \text{ MPa} \times 37.69 \text{ mm}^2$ (cross-sectional area = mass (4,17 g) / (density (1120 kg/m^3 [69]) \times length_{tendon} ($58.74 \times 10^{-2} \text{ m}$))) which was used as the reference position of zero strain. A LCR sensor was sutured with a visible capacitor pre-strain onto the tendon while the tendon itself was in a slack position (i.e., -2 mm strain). After 20-minutes rest, the tendon was pre-conditioned with 0 to 1 % strains at 0.05 %/s for 101 cycles, and with 0 to 2% strains at 2%/s for 51 cycles followed by the formal test (51 cycles of 0 to 4 % strains at 4 %/s). Each cyclic loading condition was followed by 5 minutes of rest in the slack position. During testing, the tendon

was kept hydrated by spraying a solution of 0.9% sodium chloride in water every 2 minutes. The RF of the LCR sensor was calibrated to the strain values produced with sonomicrometry crystals aligned with the LCR sensor using a linear regression ($y = 28.33x - 0.33$; with $y =$ strain in % and $x =$ RF of the LCR sensor).

4.4.6. In-vivo sensor implantation and measurement

A LCR sensor was calibrated using the same method as the sensor sensitivity measurement described above. The sensor was then gas sterilized using Ethylene oxide. Prior to implantation, a sheep (Île-de-France, 37.8 kg) was trained to walk and trot on a treadmill at different speeds and inclination angles. The sheep was motivated with pellets provided in between trotting periods. Food was removed 12 h prior to surgery. On the day of surgery, the sheep was sedated with Dexdomitor (0.5mg/ml at 0.05mg/kg) and Alfaxan (10mg/ml at 2 mg/kg), followed by intubation and preparation of the hind limb (shaving and cleaning) while maintaining an appropriate level of anesthesia which could be as low as 0.5 % isoflurane maintenance or between 2-2.5 % isoflurane as needed. Breathing and heart rate were monitored throughout the procedures and lubricum was applied on the eyes. Sensor implantation was performed in a standard sterile veterinary surgical environment. A skin incision was made on the left hind limb of the sheep to expose the gastrocnemius-tendon region. The tendon of the medial gastrocnemius was isolated, and the stretchable capacitor of the LCR sensor was sutured on the tendon with a visible pre-strain. The coil antenna of the LCR sensor was sutured on subcutaneous tissues. A custom-designed stainless-steel buckle transducer [70] was surgically implanted onto the same tendon distally from the stretchable capacitor to measure the muscle force on the tendon. Following routing of the wires of the buckle transducer underneath and across the skin and soldering the wires to a backpack connector, the skin incision was closed. A subcutaneous injection of Buprenorphine (0.02 mg/kg) and Metacam (0.05 mg/kg) was administered (as well as every 12 h thereafter) to reduce post-surgery symptoms. The sheep was willingly walking in her pen 2h following completion of the surgery. Overall, the sheep was given 68 h to recover until there were no signs of limping and the sheep was fully weight bearing while walking in her pen before obtaining experimental data. Following recovery, the sheep was willingly trotting on the treadmill at 3 mph without major signs of limping, during which tendon strain and muscle force data (999.878 Hz) were recorded. Furthermore, video recordings at 208.25 Hz of a highspeed camera (Pike F032B, Allied Vision, Stadroda, Germany) were used to determine the swing and stance phases of the gait cycles. Data of all sensors was synchronized with the use of a light pulse visible in the video and a change in voltage output sent simultaneously to the strain sensor system and buckle transducer system.

4.5. References

1. Devita, P. and W.A. Skelly, Effect of landing stiffness on joint kinetics and energetics in the lower extremity. *Med Sci Sports Exerc*, 1992. **24**(1): p. 108-15.
2. Amis, A.A. and G.P. Dawkins, Functional anatomy of the anterior cruciate ligament. Fibre bundle actions related to ligament replacements and injuries. *J Bone Joint Surg Br*, 1991. **73**(2): p. 260-7.
3. Frank, C.B., Ligament structure, physiology and function. *J Musculoskelet Neuronal Interact*, 2004. **4**(2): p. 199-201.
4. Gardinier, E.S., et al., Altered loading in the injured knee after ACL rupture. *J Orthop Res*, 2013. **31**(3): p. 458-64.
5. Kessler, M.A., et al., Function, osteoarthritis and activity after ACL-rupture: 11 years follow-up results of conservative versus reconstructive treatment. *Knee Surg Sports Traumatol Arthrosc*, 2008. **16**(5): p. 442-8.
6. Ahmad, C.S., et al., Evaluation and management of hamstring injuries. *Am J Sports Med*, 2013. **41**(12): p. 2933-47.
7. Cronin, N.J. and G. Lichtwark, The use of ultrasound to study muscle-tendon function in human posture and locomotion. *Gait Posture*, 2013. **37**(3): p. 305-12.
8. Mian, O.S., et al., Gastrocnemius muscle-tendon behaviour during walking in young and older adults. *Acta Physiol (Oxf)*, 2007. **189**(1): p. 57-65.
9. Beynnon, B.D., et al., Anterior cruciate ligament strain behavior during rehabilitation exercises in vivo. *Am J Sports Med*, 1995. **23**(1): p. 24-34.
10. Beynnon, B.D., et al., The strain behavior of the anterior cruciate ligament during squatting and active flexion-extension. A comparison of an open and a closed kinetic chain exercise. *Am J Sports Med*, 1997. **25**(6): p. 823-9.
11. Hosseini Nasab, S.H., et al., Length-Change Patterns of the Collateral Ligaments During Functional Activities After Total Knee Arthroplasty. *Ann Biomed Eng*, 2020. **48**(4): p. 1396-1406.
12. Tsai, T.Y., et al., In-vivo elongation of anterior and posterior cruciate ligament in bi-cruciate retaining total knee arthroplasty. *J Orthop Res*, 2018. **36**(12): p. 3239-3246.
13. Ravary, B., et al., Strain and force transducers used in human and veterinary tendon and ligament biomechanical studies. *Clin Biomech (Bristol, Avon)*, 2004. **19**(5): p. 433-47.

14. Roriz, P., et al., From conventional sensors to fibre optic sensors for strain and force measurements in biomechanics applications: a review. *J Biomech*, 2014. **47**(6): p. 1251-61.
15. Fleming, B.C. and B.D. Beynon, In vivo measurement of ligament/tendon strains and forces: a review. *Ann Biomed Eng*, 2004. **32**(3): p. 318-28.
16. Wren, T.A., et al., Mechanical properties of the human achilles tendon. *Clin Biomech (Bristol, Avon)*, 2001. **16**(3): p. 245-51.
17. Heijne, A., et al., Strain on the anterior cruciate ligament during closed kinetic chain exercises. *Med Sci Sports Exerc*, 2004. **36**(6): p. 935-41.
18. Fleming, B.C., et al., The strain behavior of the anterior cruciate ligament during bicycling. An in vivo study. *Am J Sports Med*, 1998. **26**(1): p. 109-18.
19. Nagamoto, H., et al., Transosseous-equivalent repair with and without medial row suture tying: a cadaveric study of infraspinatus tendon strain measurement. *JSES Open Access*, 2017. **1**(2): p. 104-108.
20. Fukashiro, S., et al., Comparison between the directly measured achilles tendon force and the tendon force calculated from the ankle joint moment during vertical jumps. *Clin Biomech (Bristol, Avon)*, 1993. **8**(1): p. 25-30.
21. Edsfeldt, S., et al., In vivo flexor tendon forces generated during different rehabilitation exercises. *J Hand Surg Eur Vol*, 2015. **40**(7): p. 705-10.
22. Erdemir, A., et al., Fiberoptic measurement of tendon forces is influenced by skin movement artifact. *J Biomech*, 2003. **36**(3): p. 449-55.
23. Cai, L., et al., Super-stretchable, transparent carbon nanotube-based capacitive strain sensors for human motion detection. *Sci Rep*, 2013. **3**: p. 3048.
24. Hu, W.L., et al., Elastomeric transparent capacitive sensors based on an interpenetrating composite of silver nanowires and polyurethane. *Applied Physics Letters*, 2013. **102**(8).
25. Cohen, D.J., et al., A Highly Elastic, Capacitive Strain Gauge Based on Percolating Nanotube Networks. *Nano Letters*, 2012. **12**(4): p. 1821-1825.
26. Valentine, A.D., et al., Hybrid 3D Printing of Soft Electronics. *Adv Mater*, 2017. **29**(40).
27. Pang, C., C. Lee, and K.Y. Suh, Recent advances in flexible sensors for wearable and implantable devices. *Journal of Applied Polymer Science*, 2013. **130**(3): p. 1429-1441.

28. Kim, D.A., S.-K.; Yoon, J., Highly Stretchable Strain Sensors Comprising Double Network Hydrogels Fabricated by Microfluidic Devices. *Advanced Materials Technologies*, 2019. **4**(1800739): p. 1-7.
29. Hou, C.X., W.; Wu, R.; Wang, Y.; Xu, Q.; Liu, X. Y.; Guo, W., A Biodegradable and Stretchable Protein-Based Sensor as Artificial Electronic Skin for Human Motion Detection. *Small*, 2019. **15**(1805084): p. 1-8.
30. Cai, Y.Q., J.; Li, W.; Tyagi, A.; Liu, Z.; Hossain, D.; Chen, H.; Kim, J.-K.; Liu, H.; Zhuan, M.; You, J.; Xu, F.; Lu, X.; Sun, D.; Luo, Z., A stretchable, conformable, and biocompatible graphene strain sensor based on a structured hydrogel for clinical application. *Journal of Materials Chemistry A*, 2019. **7**: p. 27099-27109.
31. Dakurah, M.N., et al., Implantable Bladder Sensors: A Methodological Review. *International Neurourology Journal*, 2015. **19**(3): p. 133-141.
32. Sun, R.C., Sara Correia; Chen, Yan; Xiang, Chaoqun; Xu, Lulu; Zhan, Bing; Chen, Mudan; Farrow, Ian; Scarpa, Fabrizio; Rossiter, Jonathan, Stretchable Piezoelectric Sensing Systems for Self-Powered and Wireless Health Monitoring. *Advanced Materials Technologies*, 2019. **4**(1900100).
33. Stauffer, F., et al., Soft Electronic Strain Sensor with Chipless Wireless Readout: Toward Real-Time Monitoring of Bladder Volume. *Advanced Materials Technologies*, 2018. **3**(6).
34. Sang, S.B., et al., Highly sensitive wearable strain sensor based on silver nanowires and nanoparticles. *Nanotechnology*, 2018. **29**(25).
35. Cui, Z., et al., Design and operation of silver nanowire based flexible and stretchable touch sensors. *Journal of Materials Research*, 2015. **30**(1): p. 79-85.
36. Chen, H.-Y.C., A. T., A Stretchable Inductor With Integrated Strain Sensing and Wireless Signal Transfer. *IEEE Sensors Journal*, 2020. **20**(13): p. 7384-7391.
37. Seyedin, S.Z., P.; Naebe, M.; Yin, S.; Chen, J.; Wang, X.; Razal, J. M., Textile strain sensors: a review of the fabrication technologies, performance evaluation and applications. *Materials Horizons*, 2019. **6**: p. 219-249.
38. Souri, H.B., H.; Jusufi, A.; Radacsi, N.; Stokes, A. A.; Park, I.; Sitti, M.; Amjadi, M., Wearable and Stretchable Strain Sensors: Materials, Sensing Mechanisms, and Applications. *Advanced Intelligent Systems*, 2020. **2**(2000039).
39. Amjadi, M., et al., Stretchable, Skin-Mountable, and Wearable Strain Sensors and Their Potential Applications: A Review. *Advanced Functional Materials*, 2016. **26**(11): p. 1678-1698.

40. Boutry, C.M., et al., A stretchable and biodegradable strain and pressure sensor for orthopaedic application. *Nature Electronics*, 2018. **1**(5): p. 314-321.
41. Zens, M., et al., A New Approach to Determine Ligament Strain Using Polydimethylsiloxane Strain Gauges: Exemplary Measurements of the Anterolateral Ligament. *Journal of Biomechanical Engineering-Transactions of the Asme*, 2014. **136**(12).
42. Boutry, C.M., et al., A stretchable and biodegradable strain and pressure sensor for orthopaedic application. *Nature Electronics*, 2018. **1**(5): p. 314-321.
43. Klosterhoff, B.S., et al., Wireless Implantable Sensor for Noninvasive, Longitudinal Quantification of Axial Strain Across Rodent Long Bone Defects. *J Biomech Eng*, 2017. **139**(11).
44. Weydts, T.B., L.; Soebadi, M. A.; De Ridder, D.; Puers, R., A novel method to investigate bladder wall behavior by acceleration and pressure sensing. *Sensors and Actuators A.*, 2018. **280**: p. 376-382.
45. Lee, K.J.C., N.; Kim, S., Batteryless, wireless strain sensor using resonant frequency modulation. *Sensors*, 2018. **18**(3955).
46. Lee, J., et al., Stretchable and suturable fibre sensors for wireless monitoring of connective tissue strain. *Nature Electronics*, 2021. **4**(4): p. 291-301.
47. Liu, C.Y. and Y.G. Dong, Resonant Coupling of a Passive Inductance-Capacitance-Resistor Loop in Coil-Based Sensing Systems. *Ieee Sensors Journal*, 2012. **12**(12): p. 3417-3423.
48. Wang, T., et al., Programmable mechanical stimulation influences tendon homeostasis in a bioreactor system. *Biotechnol Bioeng*, 2013. **110**(5): p. 1495-507.
49. Morrison, S.M., T.J. Dick, and J.M. Wakeling, Structural and mechanical properties of the human Achilles tendon: Sex and strength effects. *J Biomech*, 2015. **48**(12): p. 3530-3.
50. Wang, T., et al., In vitro loading models for tendon mechanobiology. *J Orthop Res*, 2018. **36**(2): p. 566-575.
51. Johnson, G.A., et al., Tensile and viscoelastic properties of human patellar tendon. *J Orthop Res*, 1994. **12**(6): p. 796-803.
52. Hamoir, G., L. Piraux, and I. Huynen, Q-factor improvement of integrated inductors using high aspect ratio ferromagnetic nanowires. *Microwave and Optical Technology Letters*, 2012. **54**(7): p. 1633-1637.
53. Siman-Tov, E., et al., Increasing the Range of Wireless Power Transmission to Stretchable Electronics. *Ieee Transactions on Microwave Theory and Techniques*, 2018. **66**(11): p. 5021-5030.

54. Arkwright, J.W., et al., In-vivo demonstration of a high resolution optical fiber manometry catheter for diagnosis of gastrointestinal motility disorders. *Opt Express*, 2009. **17**(6): p. 4500-8.
55. Yamada, T., et al., A stretchable carbon nanotube strain sensor for human-motion detection. *Nat Nanotechnol*, 2011. **6**(5): p. 296-301.
56. Hu, Y.G., et al., A low-cost, printable, and stretchable strain sensor based on highly conductive elastic composites with tunable sensitivity for human motion monitoring. *Nano Research*, 2018. **11**(4): p. 1938-1955.
57. Rahimi, R., et al., Highly Stretchable and Sensitive Unidirectional Strain Sensor via Laser Carbonization. *Acs Applied Materials & Interfaces*, 2015. **7**(8): p. 4463-4470.
58. Lee, S.M., et al., Flexible and Implantable Capacitive Microelectrode for Bio-potential Acquisition. *Biochip Journal*, 2017. **11**(2): p. 153-163.
59. Delivopoulos, E., et al., Concurrent recordings of bladder afferents from multiple nerves using a microfabricated PDMS microchannel electrode array. *Lab on a Chip*, 2012. **12**(14): p. 2540-2551.
60. Srikandakumar, A., E.H. Johnson, and O. Mahgoub, Effect of heat stress on respiratory rate, rectal temperature and blood chemistry in Omani and Australian Merino sheep. *Small Ruminant Research*, 2003. **49**(2): p. 193-198.
61. Wood, M.V., et al., 3D Printed Clamps to Study the Mechanical Properties of Tendons at Low Strains. *Physica Status Solidi B-Basic Solid State Physics*, 2019. **256**(1).
62. Kaya, M., T.R. Leonard, and W. Herzog, Control of ground reaction forces by hindlimb muscles during cat locomotion. *J Biomech*, 2006. **39**(15): p. 2752-66.
63. Kear, M. and R.N. Smith, A method for recording tendon strain in sheep during locomotion. *Acta Orthop Scand*, 1975. **46**(6): p. 896-905.
64. Biewener, A.A., Muscle-tendon stresses and elastic energy storage during locomotion in the horse. *Comp Biochem Physiol B Biochem Mol Biol*, 1998. **120**(1): p. 73-87.
65. Lawson, S.E., et al., Effect of toe and heel elevation on calculated tendon strains in the horse and the influence of the proximal interphalangeal joint. *J Anat*, 2007. **210**(5): p. 583-91.
66. Riemersma, D.J., et al., Tendon strain in the forelimbs as a function of gait and ground characteristics and in vitro limb loading in ponies. *Equine Veterinary Journal*, 1996. **28**(2): p. 133-138.
67. Tybrandt, K., et al., High-Density Stretchable Electrode Grids for Chronic Neural Recording. *Adv Mater*, 2018. **30**(15): p. e1706520.

68. Dual, S.A.Z., B. L.; Sündermann, S.; Cesarovic, N.; Kron, M.; Magkoutas, K.; Hengsteler, J.; Falk, V.; Starck, C.; Meboldt, M.; Vörös, J.; Daners, M. S., Continuous Heart Volume Monitoring by Fully Implantable Soft Strain Sensor. *Advanced Healthcare Materials*, 2020. **9**(2000855): p. 1-11.
69. Ker, R.F., Dynamic tensile properties of the plantaris tendon of sheep (*Ovis aries*). *J Exp Biol*, 1981. **93**: p. 283-302.
70. Walmsley, B., J.A. Hodgson, and R.E. Burke, Forces produced by medial gastrocnemius and soleus muscles during locomotion in freely moving cats. *J Neurophysiol*, 1978. **41**(5): p. 1203-16.




Chapter 5: Stretchable Sensor Fabrication Protocol

The fabrication protocol consists of six main steps:

- Dispersion of TiO₂ nanowires
- Synthesis of Au-TiO₂ nanowires
- Membrane preparation and nanowire filtration
- Fabrication of stretchable capacitor
- Fabrication of LCR circuit
- Fabrication of suture pads and PDMS casting

5.1. Dispersion of TiO₂ nanowire

5.1.1 Materials and facilities

Materials	Details
Chemicals	<ul style="list-style-type: none">• TiO₂ nanowires (TiO₂ nanowire-A, length ≈10 μm, ACSMaterial)• Polyethylene glycol (PEG, average M~2000, Sigma-Aldrich)• Deionized water (diH₂O)
Polyvinylidene fluoride (PVDF) membrane	47mm, 0.22 μm pore size, Millipore 
Scale (Mettler Toledo)	
Vortex mixer	

5.1.2. Procedures


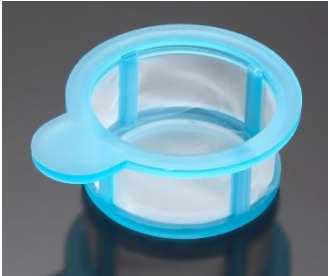


1. 0.0889 mL of PEG is diluted in 10 mL of diH₂O to make 1% PEG-H₂O solution
2. 1g of TiO₂ nanowire wetcake is added into the PEG-H₂O solution and vortexed for 5 mins
3. After 1 min of settlement, take off the top 5-10 mL of supernatant to get rid of chunks
4. Fill up the solution to 40 mL with diH₂O
5. Weigh one PVDF membrane
6. Filter 10 mL TiO₂ nanowire on the membrane and weigh it again to calculate the nanowire concentration in the solution. This is for parameter calculation for the nanowire synthesis

5.1.3. Tips

1. It is suggested to visually check the nanowire dispersion at the end of step 4. A well dispersed nanowire solution should look like “flowing cloud” without obvious nanowire aggregates. If not, the solution should be vortexed again

5.2. Synthesis of Au-TiO₂ nanowire

5.2.1. Materials and facilities

Materials	Details
Chemicals	<ul style="list-style-type: none">• TiO₂ nanowire solution• Polyvinylpyrrolidon (PVP, average Mw ~55'000, Sigma-Aldrich)• Hydroxylamine (HxO, ACS reagent, 98.0%, Sigma-Aldrich)• Gold(III) chloride solution (30 wt % in dilute HCl, Sigma-Aldrich)• Hydrochloric acid (HCl, Sigma-Aldrich)• diH₂O
Centrifuge tube (Falcon)	
Strainers (40 μm of pore size)	
Syringes (20 mL, 20mm in diameter)	
Pipette (tips)	

Pumping machine	
Supersonic machine	

5.2.2. Procedures

1. Prepare PVP solution (0.33 gr/mL). When dissolving PVP, vortex it for 30 s and then dissolve it with supersonic machine (set temperature at 0 °C) for 30 s, repeat these two steps until the PVP is fully dissolved
2. Sieve 1 mL of TiO₂ nanowire solution through a strainer in a centrifuge tube, and then quickly add 35 mL of diH₂O. Try to use a pipette to “wash” the strainer during adding diH₂O
3. Pour the TiO₂ nanowire solution into a beaker with a magnetic stirrer. Leave the beaker on the hotplate (with stirring function) and make sure the stirrer stirring on the middle bottom of the beaker
4. Add 128 µl of HxO and 4 mL of PVP into the TiO₂ nanowire solution
5. Mix the other 40 mL of diH₂O with 128 µl of Gold(III) chloride solution
6. Fill the Gold(III) chloride solution in 2 syringes. Connect the syringe with a pipeline and the pipette tip tightly. Then get rid of the gas bubble in them. Put the pipette tip in the TiO₂ solution and fix the setup
7. Set up pumping machine: *direction*: pumping; *volume*: 20 mL; *diameter*: 20 mm; *speed*: 2.8 mL/min.
8. Inject the Gold(III) chloride solution at 2.8 mL/min until 4mL. Then switch to 1.4 mL/min until complete both syringes.
9. Increase the temperature of the hotplate to 80 °C and add 2 mL of HCl. Stir the solution for 45 mins


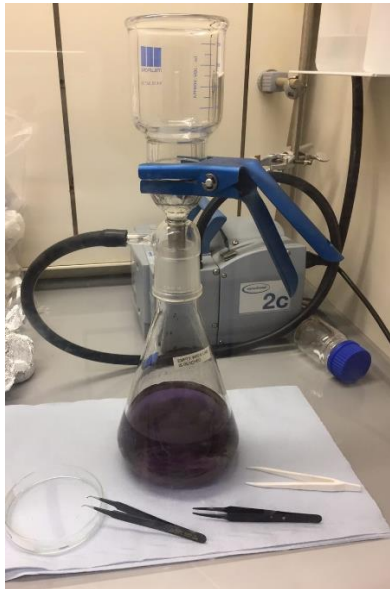

10. Sieve the final solution again with a strainer

5.2.3. Tips

1. Always use fresh PVP solution (less than one week). Otherwise, the quality of Au-TiO₂ nanowire solution may be dramatically affected
2. In step 6, leave the pipette tip at the middle layer of the TiO₂ solution but not close to the surface. Otherwise, it may create gas bubbles in the bottom solution during pumping, which affects the quality of Au-TiO₂ nanowire solution
3. Fully eliminate gas in the syringe, pipeline, and pipette tip before pumping
4. If bubbles are generated, use a pipette tip to break them before moving forward
5. Quality of Au-TiO₂ nanowire should be checked using a microscope (i.e., scanning electron microscope). Good quality means that TiO₂ nanowires are fully covered with Au particles

5.3. Membrane preparation and nanowire filtration

5.3.1. Materials and facilities

Materials	Details
Chemicals	Au-TiO ₂ nanowire solution Phosphate-buffered saline (PBS, PH~7.4 (1×), Gibco)
PVDF membrane	
Filtration device	
Adobe illustrator	/
Wax printer	

5.3.2. Procedures

Wax printing

1. Design the capacitor patterns using the Adobe Illustrator app. The colour should be set “pure black”. Save the picture as a PDF file
2. Print the picture on a A4 paper
3. Superimpose another A4 paper on top of the printed file. People should be able to see the outlines of the black circles under the top paper sheet. Align the membranes with the outlines underneath. Tape the membrane on the paper.
4. Put back the paper into the tray of the printer. Print the picture on the membranes (Print Quality ~ “Photo”)

Nanowire filtration




1. Before filtration, remove the dust on the membrane using a nitrogen gun
2. Vortex the Au-TiO₂ nanowire solution for 1 min. Filter 2 mL of Au-TiO₂ nanowire solution through the membrane (presoaked by diH₂O). The nanowires are then deposited on the membrane. The membrane is then dried on a hotplate at 45 °C for 5 min
3. Wash the deposited nanowires with 2 mL of PBS
4. Check the serial resistance of the nanowire track, which should be less than 2 Ohm. All membranes should be sealed in the petri dishes before leaving the nanowire hood



5.3.3. Tips

1. Wear gloves while performing wax printing
2. Better to vortex the Au-TiO₂ nanowire solution every time before filtration

5.4. Fabrication of stretchable capacitor

5.4.1. Materials and facilities

Materials	Details
Chemicals	<ul style="list-style-type: none"> • Polydimethylsiloxane (PDMS, Sylgard 184) • Anhydrous heptane (AH, 99%, Sigma-aldrich) • Silicone rubber (Dragon Skin (DS), slow cure 10, Smooth-On) • Silver powder (Ag, length = 2-3.5 μm, Sigma-Aldrich) • Universal mold release (Smooth-On)
Spin-coating machine	
Hotplate	
Conditioning mixer	

Cream container	
Glass wafer	
PEN foil	25 μm , Teonex Q51

5.4.2. Procedures

PDMS preparation

1. Pour curing agent in PDMS solution with a mass ratio of 1:10 in a cream container
2. Mix the obtained solution in the conditioning mixer (mixing: 3 min, 2000 rpm; deforming: 1 min, 2200 rpm)
3. Degas the PDMS solution using a vacuum chamber for 8 mins

DS-heptane solution preparation

1. Synthesize DS solution by mixing part A and B together with a mass ratio of 1:1. Mix the obtained solution in the conditioning mixer (mixing: 1 min, 2000 rpm; deforming: 30 s, 2200 rpm).
2. Use the anhydrous heptane to dilute the DS solution into two separate solutions. Solution 1[#] has a mass ratio of DS:AH~1:2, and solution 2[#] is 2:1. Shake them firmly right after mixing until the texture is homogenous, and thus the DS is fully dissolved into both solutions.
3. Degas the solutions using the vacuum chamber for 30 s. Store the solutions in the freezer at -20 °C

Ag-PDMS composite synthesis

1. Mix PDMS and Ag powder with a VOLUME ratio of Ag:PDMS~0.3:1. The densities of Ag and PDMS are 10.49 and 0.965 gr/cm³, respectively
2. Mix the composite in the conditioning mixer (mixing: 3 min, 2000 rpm; deforming: 1 min, 2200 rpm). Store the composite in the freezer at -20 °C

Stretchable capacitor transfer

1. Spin-coat universal mold release on a wafer at 600 rpm for 30 s




2. Spin-coat PDMS on the wafer at 600 rpm for 30 s, then cure the PDMS on a hotplate at 75 °C for 7 mins.
3. Transfer the Au-TiO₂ nanowire from the PVDF membrane onto the PDMS by gently placing the membrane in contact with it. Cure the PDMS on a hotplate at 75 °C for 12 mins with a weight (750 g) on top
4. Peel the membrane, and the Au-TiO₂ nanowires are left on the PDMS
5. In all subsequent steps, PEN foil is used to mask the contact pads and is removed each time after spin-coating. DS solution (Solution 1[#]) is spin-coated (8000 rpm, 30 s) to cover the first Au-TiO₂ nanowire layer and is cured on the hotplate at 75 °C for at least 60 mins.
6. Repeat step 5 by spin-coating the 2nd layer of DS solution (Solution 2[#]) at 8000 rpm for 30s and cure it for at least 60 mins
7. Spin-coat the 3rd layer of DS solution (Solution 2[#]) at 6000 rpm for 30s. Transfer the second Au-TiO₂ nanowire layer, and then cure the DS on the hotplate at 75 °C for 6 mins. Peel the membrane and the Au-TiO₂ nanowires are left on the DS
8. Spin-coat PDMS (600 rpm, 30 s) on the wafer to seal the nanowire
9. Cover the nanowire contact pads with Ag composite, and cure the Ag composite at 75 °C for 2 hours

5.4.3. Tips

1. Because heptane evaporates fast, the degassing time should be limited to 30 s
2. Leave the DS solution at room temperature for 5 mins before using it
3. The DS solutions gradually cure even in low temperature in the freezer. Therefore, only use DS solutions made in the past 24 hours
4. While preparing the Ag-PDMS composite, break down aggregates of Ag powder before adding the PDMS
5. Ag-PDMS composite gets creamy with time going. It remains good quality 2-12 weeks after being made.
6. Always stir the Ag-PDMS composite before using it
7. While spin-coating PDMS, fix the wafer in the centre of the spin-coating machine
8. While peeling the membrane, make sure that the PDMS does not detach from the wafer

5.5. Fabrication of LCR circuit

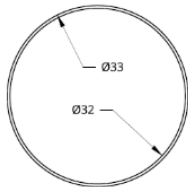
5.5.1. Materials and facilities

Materials	Details																
Oven	 <p>A Memmert oven with a digital display showing 081°C and various control knobs. The oven is stainless steel and has a warning label that reads "ALL SAMPLES CONTAINING NANOWIRES EXPOSED MUST BE IN A CLOSED CONTAINER".</p>																
Laser cutter	<p>Speedy 300, Trotec</p>  <p>A red Trotec Speedy 300 laser cutter. The machine has a glass top and a red front panel with the Trotec logo and the text "Speedy 300™" and "trotec laser, marking, cutting, engraving".</p>																
LCR meter	<p>IM 3536, Hioki</p>  <p>A Hioki IM 3536 LCR meter. The screen displays the following measurements: <table border="1" data-bbox="699 1608 895 1697"> <tr> <td>Z</td> <td>836.13mΩ</td> <td>MODE</td> <td>SET</td> </tr> <tr> <td>L</td> <td>0.12003μH</td> <td>NOI</td> <td>NOI</td> </tr> <tr> <td>C</td> <td>2.09</td> <td>FILE</td> <td>FILE</td> </tr> <tr> <td>R</td> <td>352.03mΩ</td> <td>SPS</td> <td>SPS</td> </tr> </table> </p>	Z	836.13mΩ	MODE	SET	L	0.12003μH	NOI	NOI	C	2.09	FILE	FILE	R	352.03mΩ	SPS	SPS
Z	836.13mΩ	MODE	SET														
L	0.12003μH	NOI	NOI														
C	2.09	FILE	FILE														
R	352.03mΩ	SPS	SPS														
CorelDRAW	Version X7																

5.5.2. Procedures

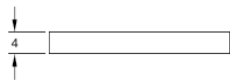
Fabricate the inductive coil

1. The 2D pictures are drawn using the CorelDRAW app. An example picture is attached at the end of the fabrication protocol
2. Prepare PMMA rings (as the picture below) using the laser cutter. The rings are 5 mm in width, 33 mm in outside diameter, 1 mm in thickness.



Name: Coil ring

Material: PMMA
 *Thickness: 3mm, 4mm
 Number: 10 pieces for each thickness



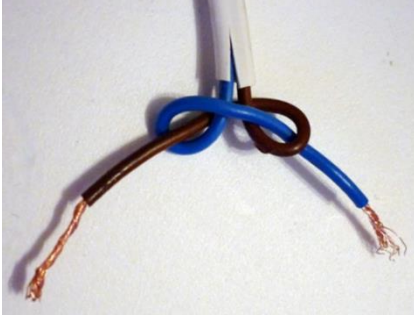
3. Measure the capacitance of the stretchable capacitor using the LCR meter
4. Check the number of turns in the coil that matches the capacitance of the stretchable capacitor. The empirical parameters can be found in the table below. According to the number of turns needed, a wire is prepared with a length (mm) = coil turns*33* π +300

Capacitance of capacitor (pF)	Number of turns
19	9
20	9
22	8
24	8
26	8
28	7
31	7

5. Wrap the wire around the ring. Then tape the wire on the ring for fixation



6. Braid the two free wires of the coil by twisting them. Tape the wire at the 8.5 cm mark so that it does not move. Make an underwriter knot using tweezers as below



7. Secure the knot using Parafilm (3×20 mm)
8. Burn the ends of both wires and leave about 3-5 mm of burnt wires. Check the resistance of the coil, which should be less than 5 Ohm

Complete the LCR circuit


1. Put Ag composite on the two contacts of the capacitor.
2. Put the two burnt ends of the coil in the Ag composite. Cure the Ag composite for 2 h in the oven (80 °C)
3. Check the resonant frequency of the LCR circuit using the custom-designed readout system

5.5.3. Tips

1. The number of turns in the coil influences the inductance of the coil inductor, and ultimately determines the resonant frequency of the LCR circuit
2. While bonding the coil to the capacitor, make sure that the exposed cables are very well covered with Ag composite

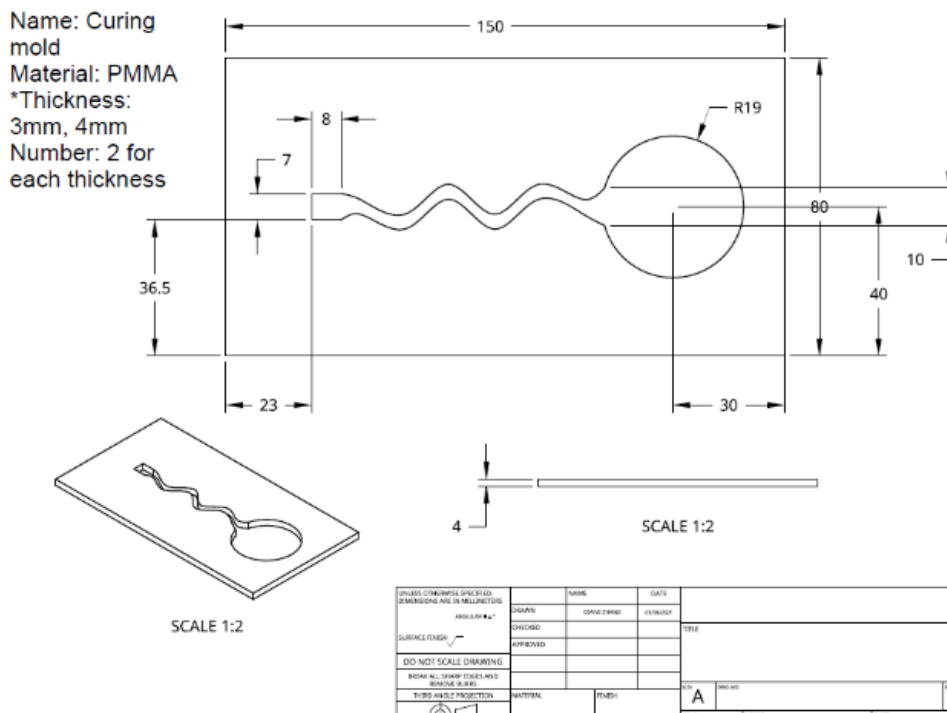
5.6. Fabrication of suture pads and PDMS embedding

5.6.1. Materials and facilities

Materials	Details
Epoxy	(UHU Plus Schnellfest Epoxikleber)
Laser cutter	Speedy 300, Trotec 

5.6.2. Procedures

1. Fabricate the suture pads and PDMS molds (mold 1[#] and 2[#], attached at the end of the fabrication protocol) using the laser cutter.



2. Glue one suture pad to the bottom of the stretchable capacitor (the wire-bonding side) using the epoxy. Furthermore, Cover the wire-capacitor contacts with epoxy

3. Tape the mold 1[#] to a PMMA plate and seal the intervals with PDMS (cure in an oven at 80°C for 30 mins)
4. Put the contact part of the sensor on the bottom square area of the mold. The fixation pad should face the bottom of the mold. Leave the capacitor tilted so that the PDMS does not leak onto it during curing



5. Put the wires inside the “wave” area and put the coil in the top circle area of the mold. Inject PDMS in the mold with a syringe. Fully cure the PDMS in an oven at 80°C for 1 h. Gently remove the sample from the mold
6. Repeat step 5 in the mold 2[#]
7. Glue the other suturing pad to the far end of the stretchable capacitor with epoxy. Glue the coil suturing pad to the bottom of the antenna with PDMS (cure in an oven at 80°C for 30 mins)
8. Cover the epoxy with PDMS

5.6.3. Tips

1. In step 5, only inject half of the PDMS first, and cure it in the oven. Then inject more PDMS to finish the embedding procedure

Chapter 6: Discussion & conclusions

Knowledge of *in-vivo* musculoskeletal soft tissue (MST) strain patterns during dynamic movements can reveal their functional and pathological mechanisms. For this purpose, both non-invasive [1-3] and invasive [4, 5] technologies have been developed and implemented for the *in-vivo* measurement of MST strain. However, critical limitations exist in current state-of-the-art technologies. Ultrasound imaging is limited by the depth that ultrasound waves can reach in the living body and the significant out-of-plane error [6] that leads to variation in the structures being investigated. Similarly, dynamic fluoroscopy is limited by the assumptions and simplifications of including modelled MST structures, as well as the small field of view of the fluoroscope. Implantable sensors, on the other hand, have recently enabled the direct measurement of ligament and tendon strains *in vivo*. However, the cable for signal transmission limits the measurement of dynamic movement and carries potential safety hazards. With the purpose to overcome the limitations of traditional strain sensors, this PhD project developed a novel wireless stretchable strain sensor based on stretchable electronics and radio frequency identification technologies. This new sensor was developed through optimizing a previous strain sensor prototype consisted of a stretchable capacitor bonded to a fragile coil. The new sensor was demonstrated to have excellent resolution and sufficient strain range, while also remaining electrically stable under environmental changes and fatigue loading. Finally, the *in-vivo* applicability of the sensor was demonstrated through implantation and measurement in a sheep model.

6.1. The optimized fabrication protocol stabilized the quality of the strain sensor

The fabrication protocol of the strain sensor was developed through building on the previous work of Dr. Flurin Stauffer (Chapter 3). The optimized protocol enabled the fabrication of robust strain sensors in order to fulfil the prerequisites of *in-vivo* implantation and dynamic measurement. In addition, through standardizing the procedures of nanowire transfer and wire coil fabrication, the optimized protocol ensured that all newly fabricated sensors could have a similar quality.

An important change in the fabrication protocol was the utilization of polydimethylsiloxane (PDMS) as the stretchable elastomer. The primary reason for using PDMS was that PDMS is biocompatible and has been previously applied for casting implantable sensing devices [7, 8]. For the capacitor in this technology, replacing Dragon Skin (DS) rubber with PDMS slightly increased the stiffness of the capacitor, due to PDMS' higher Young's modulus. However, PDMS has a much lower Young's modulus than muscles and tendons [9, 10] so that the stretchable capacitor still had a sufficiently high compliance to ensure minimal disruption to the natural elongations of MSTs. For the wire coil, PDMS was mainly applied to cast the coil in a protective shell. Such PDMS casting has two main functions: 1) to protect the coil from damage under compressive loads; 2) to mitigate the effect of ions in body fluid on the conductivity of the wire.

The inductive coil was originally fabricated by simply braiding wires without any clear structure, resulting in an unpredictable inductance of the coil. Such coils resulted in a large variation in the resonant frequency (RF) of the LCR sensor from the optimal value of 13.5 MHz (Appendix, section 3), which potentially also affects the sensing range of the sensor. Therefore, the fabrication of the wire coil was optimized in the new protocol. A “single-layer” coil was fabricated by wrapping the wire tightly and orderly around a PMMA ring with a fixed diameter. The inductance of the coil could then be controlled by changing the number of coil cycles. Thus, depending on the capacitance of the capacitor and the target RF of the LCR sensor, the number of coil cycles that resulted in the target inductance could be calculated and implemented.

The optimal nanowire synthesis and transfer protocols were extremely important to the quality of the stretchable capacitor and were determined based on multiple trials and measurements. For the nanowire synthesis, the parameters, especially the amount of gold particles used, were adjusted from the original recipe, in order to match the specific titanium dioxide (TiO_2) nanowire concentration in each batch of “mother” solution. A suitable and controlled ratio of gold particles and TiO_2 nanowires ensures the nanowires are well coated by the gold, resulting in a good conductivity of the final gold-coated titanium dioxide (Au-TiO_2) nanowire solution. Here, it is recommended that a large batch of TiO_2 mother solution is prepared, before the optimal amount of gold particles needed for nanowire synthesis is determined. In this manner, the quality of newly synthesized Au-TiO_2 nanowire solution can be stabilized for a relatively long period of time. In addition, once the new recipe is established, the amount of Au-TiO_2 nanowire solution filtered through each membrane can be recalculated according to the new nanowire concentration in the solution. For nanowire transfer, the effort was mainly spent on determining the new spin-coating speed that determines the thickness of the PMDS layer. In addition, once new spin-coating speed is determined, the curing time of the PDMS layer should be adjusted to ensure that nanowires can be successfully transferred.

6.2. The function of the sensor fulfilled the prerequisites of MST strain measurement

The stretchability and sampling frequency of our strain sensor system ensured the strain patterns in MSTs could be well measured during dynamic movements. Firstly, the maximum strain range of the LCR strain sensor was over 25%, which is much larger than the maximum strain levels that most MSTs can endure before structural failure (Chapter 1, table 1). Secondly, the measurement frequency of our sensor system was 1024 Hz, ensuring that strain patterns in MSTs could be captured sufficiently during dynamic movements. Finally, the different testing conditions, including phosphate-buffered saline (to simulate *in-vivo* conditions) and air, rarely affected the relative change of the sensor RF signal under stretching. Therefore, the calibration of the sensor RF against strain in the air condition can be used to interpret the data from subsequent *in-vivo* measurements.

Au-TiO₂ nanowires were used as the conductive material to fabricate the stretchable capacitor in this project. One reason was that such nanowires have been demonstrated to be biocompatible in a previous study [11]. More importantly, we found that LCR sensors made of Au-TiO₂ nanowires had a Q-factor that was higher than silver nanowires, which have been widely used previously. A LCR sensor with a high Q-factor is commonly favoured because it ensures the sensor will have a lower energy loss with oscillating current, which improves the quality of sensor signalling and ensures the readout system is able to measure the sensor signals well above the minimum distance (2 cm) in *in-vivo* environments. The Q-factor of plate-type capacitors made of nanowire networks embedded in soft elastomers could decrease under stretching because the resistance of the nanowire network increases. Studies have reported that stretchable conductors made of silver nanowires likely had cracks in the nanowire networks at higher strain levels, resulting in significant increases in their resistance, hence affecting the Q-factor [12]. Previous work on the synthesis technology of the Au-TiO₂ nanowire has shown that Au-TiO₂ nanowires had better conductivity than the silver nanowire counterparts [13]. Consistent with these previous findings, we also observed that Au-TiO₂ nanowire networks embedded in PDMS had a lower increase in resistance under stretching compared to silver nanowire networks, especially when the 10-nm Au-TiO₂ nanowires were implemented (Appendix, section 2, Fig. 1). Thus, 10-nm Au-TiO₂ nanowires were considered superior in maintaining a high Q-factor for the sensor and were utilized for fabricating the strain sensors in this project.

Recent studies have reported that the smallest strain that their sensors could detect was 0.3-0.4 % strain in *ex-vivo* measurements [5, 14]. Our sensors, however, had a better resolution which made it possible to measure strains down to 0.1 % ($\approx 9 \mu\text{m}$) in wireless measurements. In addition, the stretchable capacitor of our sensor had excellent robustness to counteract fatigue loading. This characteristic was a considerable improvement over most previous studies, which tested their sensors

during up to 5'000 cycles of loading in dry environments [11, 15-20]. In our study, 100'000 cycles of fatigue loading were applied to the capacitor under simulated *in-vivo* conditions. The capacitance of the sensor at the starting 5% pre-strain increased by 0.9% after the fatigue test, which might be because of the slight slackening of the sensor due to the viscoelastic characteristic of the elastomer. More importantly, the sensitivity (gauge factor) and resolution of the sensor remained unchanged after the fatigue testing (Appendix, section 2, Fig. 2). As a result, it could be expected that stable characteristics of our strain sensor could be achieved under cyclic loading during dynamic body movements during *in-vivo* investigations.

6.3. *In-vitro/in-vivo* sensor implantations and measurements

Before any *in-vivo* implantation, the LCR strain sensor was firstly implanted on a cadaveric sheep plantaris tendon *ex vivo* and tested in a tensile testing machine (Fig. 3c). Here, the sensor was sutured onto the tendon as suggested by the veterinary surgeon. To avoid the sensor body from being damaged by sutures during cyclic stretching, “suturing pads” were designed and implemented on the strain sensor. Thus, the suture should be fixed onto the suturing pads of the sensor rather than the soft elastomer. Our measurement showed that with such a design, the strain sensor successfully recorded continuous repetitive strain variations in the tendon during cyclic loading. The strain values from the sensor (4.2 %) were slightly larger than the results from the tensile testing machine (4.0 %), which was due to the difference in the region measured. These results demonstrated the applicability of the sensor system in measuring MST axial strains, indicating some of the potential of the sensor system to quantify strains in MSTs *in vivo*.

In collaboration with the Human Performance Lab (HPL) at the University of Calgary, a proof-of-concept *in-vivo* sensor implantation and measurement were performed in this project. The calibrated strain sensor was implanted onto the medial gastrocnemius tendon of a sheep. Three days postoperatively, the tendon strain was measured using the strain sensor during trotting on a treadmill at 1.34 m/s. While previous studies have tested other soft sensors in small mammals [5] or under passive/static movement conditions [21, 22], these measurements at HPL were probably the first implementation of stretchable strain sensors to measure *in-vivo* MST strain patterns of large mammals during dynamic movements. In this experiment, a maximum strain of 3.8 % was observed during the trotting cycles. This value is consistent with the strains measured previously in the tendons of sheep and horses during trotting, where strain ranges between 1.8-5.4 % were reported [23-26]. Overall, the *in-vivo* experiment indicated that the strain sensor system holds great potential for being applied in the study of dynamic strain patterns in the MST of living bodies.

6.4. Limitations of the strain sensor system and outlook

Despite the huge advancements made to the functionality of the stretchable sensor system for wireless measurement of MST strain, several challenges remain before clinical translation of the technology can be achieved. Although pilot measurements were indeed achieved using this system *in vivo*, a number of measurement failures were experienced in the course of this PhD. Here, the largest problems with the sensor seemed to be associated with the robustness of the sensor components. Mainly, the wires often disconnected from the PDMS shell, but the wires themselves were also seen to cut through the PDMS coating, hence changing the measurement characteristics of the system, or even rendering the system unable to measure any signals. As a result, further development is clearly required in order to improve robustness of the implantable components and their connectivity. As part of this development, the sensor fixation method should be further optimized to ensure secure sensor fixation on the MSTs. At the end of our *in-vivo* experiment, although the strain sensor remained functional after being extracted from the sheep body, it was found that one of the suture pads had already detached from the sensor. This failure could explain why no strain variation could be measured by the strain sensor after the first several trotting trials. Instead of using suturing pads, further studies could try to embed a suture into the body of the strain sensor with PDMS. Therefore, no suturing pad will be needed. However, the robustness of the suture-sensor contact should be fully validated before further *in-vivo* implantations.

In addition to the basic improvements, the overall size of the strain sensor, especially the thickness of the inductive coil (5 mm), could be fully optimized. Although there is no evidence showing that sheep movements were affected by the size of the strain sensor, the current system may be limited by the thickness of its inductive coil in the measurement of deeper MSTs. One possible idea to reduce the thickness of the inductive coil is to change its design from a single-layer coil to a multi-layer coil structure, but the method of braiding the wires should be developed and tested accordingly. Moreover, a more robust coating for the wires should be targeted, since the current PDMS protective coating proved to be fragile in *in vivo* environments.

In our sensor, the capacitor and inductive coil are bonded by silver composite, which is a relatively inferior method of making LCR sensors compared to designs such as using a single conductive fibre. The coil-capacitor contacts may increase the series resistance of the LCR circuit, and thus result in a lower Q-factor of the LCR strain sensor. In addition, this contact is fragile under compressive loading. To protect the contacts, PDMS casting has to be applied, but this affects the thickness of the sensor. A possible solution is to develop and fabricate inductive coils made of nanowire tracks, but the series resistance of the LCR sensor will be much higher compared to the sensor with wire coil, and it may have a relatively lower Q factor and a smaller sensing range.

6.5. Conclusion

This PhD project developed a wireless stretchable strain sensor for *in-vivo* MST strain measurements. A review of all technologies for *in-vivo* MST strain measurements was performed to analyse the features and limitations of these technologies, especially of the traditional strain sensors. Then, effort was spent on optimizing several stretchable electronics technologies to develop and fabricate a novel stretchable strain sensor, as well as collaboratively develop a wireless readout system. Finally, the stretchable strain sensor system was thoroughly validated for its performance in wireless strain sensing, and its *in-vivo* applicability was demonstrated through *in-vivo* implantation and measurements in a sheep model.

The review of literature indicated that various sensors have been previously applied for *in-vivo* strain measurement in the human body. However, until now, such sensors have presented a rigid construction that could lead to sensor impingement with neighbouring musculoskeletal tissues. These sensors also had cables to transmit the signal to outside systems. Such wired designs limit their applicability for *in-vivo* dynamic measurements. Thus, current strain sensors should be revolutionized towards minimally disruptive, wireless data transmission, and long-term biocompatibility to withstand the demands of *in-vivo* MST strain measurements during dynamic activities.

The experimental work involved in this thesis has optimized the fabrication protocol of stretchable strain sensors. The optimized protocol allowed successful sensor fabrication, as well as a sufficient sensor quality. The strain sensor developed in this project can be sutured onto the surface of most MSTs, allowing it to be stretched with musculoskeletal axial deformations. Using the readout system, the RF signal of the sensor could be measured wirelessly, which provides an indirect way to assess the MST strain patterns. The strain sensor presents good strain range and resolution, as well as remains electronically robust in the simulated *in-vivo* environment and under fatigue loading conditions. Ex-vivo tendon testing demonstrated the capacity of the sensor for the measurement of MST strains. The final *in-vivo* sensor implantation and measurement in the sheep model indicated that the sensor is able to measure the repetitive strain variations in living bodies.

Further work is still required in the design of the strain sensor system in order to improve its physical robustness, optimise its size, and advance its fixation method. In addition, further testing *in vivo* is required for extended periods of time to fully demonstrate its functionality and biocompatibility. If such development is successfully achieved, the presented stretchable sensor system could become a functional tool for critical biomechanical applications, towards e.g., revealing the strain patterns of different MSTs under dynamic functional and/or pathological conditions, and hence providing key knowledge on the mechanisms of failure, repair, and rehabilitation.

6.6. Reference

1. Krouskop, T.A., D.R. Dougherty, and F.S. Vinson, A pulsed Doppler ultrasonic system for making noninvasive measurements of the mechanical properties of soft tissue. *J Rehabil Res Dev*, 1987. 24(2): p. 1-8.
2. Graves, N.C., et al., Ultrasound assessment of dorsal lisfranc ligament strain under clinically relevant loads. *J Am Podiatr Med Assoc*, 2014. 104(1): p. 11-8.
3. Taylor, K.A., et al., *In vivo* measurement of ACL length and relative strain during walking. *J Biomech*, 2013. 46(3): p. 478-83.
4. Heijne, A., et al., Strain on the anterior cruciate ligament during closed kinetic chain exercises. *Med Sci Sports Exerc*, 2004. 36(6): p. 935-41.
5. Boutry, C.M., et al., A stretchable and biodegradable strain and pressure sensor for orthopaedic application. *Nature Electronics*, 2018. 1(5): p. 314-321.
6. Hatta, T., et al., *In Vivo* Measurement of Rotator Cuff Tendon Strain With Ultrasound Elastography An Investigation Using a Porcine Model. *Journal of Ultrasound in Medicine*, 2014. 33(9): p. 1641-1646.
7. Lee, D.S., et al., Biocompatibility of a PDMS-coated micro-device: Bladder volume monitoring sensor. *Chinese Journal of Polymer Science*, 2012. 30(2): p. 242-249.
8. Kim, S.H., et al., Flexible, Stretchable and Implantable PDMS Encapsulated Cable for Implantable Medical Device. *Biomedical Engineering Letters*, 2011. 1(3): p. 199-203.
9. Johnson, G.A., et al., Tensile and viscoelastic properties of human patellar tendon. *J Orthop Res*, 1994. 12(6): p. 796-803.
10. Wang, Z.X., A.A. Volinsky, and N.D. Gallant, Nanoindentation Study of Polydimethylsiloxane Elastic Modulus Using Berkovich and Flat Punch Tips. *Journal of Applied Polymer Science*, 2015. 132(5).
11. Tybrandt, K., et al., High-Density Stretchable Electrode Grids for Chronic Neural Recording. *Adv Mater*, 2018.
12. Stauffer, F., et al., Soft Electronic Strain Sensor with Chipless Wireless Readout: Toward Real-Time Monitoring of Bladder Volume. *Advanced Materials Technologies*, 2018. 3(6).
13. Tybrandt, K. and J. Voros, Fast and Efficient Fabrication of Intrinsically Stretchable Multilayer Circuit Boards by Wax Pattern Assisted Filtration. *Small*, 2016. 12(2): p. 180-4.
14. Wang, Z.W., et al., Ultrastretchable Strain Sensors and Arrays with High Sensitivity and Linearity Based on Super Tough Conductive Hydrogels. *Chemistry of Materials*, 2018. 30(21): p. 8062-8069.
15. Kim, D., S.K. Ahn, and J. Yoon, Highly Stretchable Strain Sensors Comprising Double Network Hydrogels Fabricated by Microfluidic Devices. *Advanced Materials Technologies*, 2019. 4(7).
16. Wang, Z., Y. Cong, and J. Fu, Stretchable and tough conductive hydrogels for flexible pressure and strain sensors. *J Mater Chem B*, 2020. 8(16): p. 3437-3459.
17. Sun, R.J., et al., Stretchable Piezoelectric Sensing Systems for Self-Powered and Wireless Health Monitoring. *Advanced Materials Technologies*, 2019. 4(5).

18. Jiang, H.J., et al., A Wireless Implantable Strain Sensing Scheme Using Ultrasound Imaging of Highly Stretchable Zinc Oxide/Poly Dimethylacrylamide Nanocomposite Hydrogel. *Acs Applied Bio Materials*, 2020. 3(7): p. 4012-4024.
19. Pei, X.J., et al., Stretchable, self-healing and tissue-adhesive zwitterionic hydrogels as strain sensors for wireless monitoring of organ motions. *Materials Horizons*, 2020. 7(7): p. 1872-1882.
20. Yan, D.X., et al., Ultracompliant Carbon Nanotube Direct Bladder Device. *Advanced Healthcare Materials*, 2019. 8(20).
21. Lee, J., et al., Stretchable and suturable fibre sensors for wireless monitoring of connective tissue strain. *Nature Electronics*, 2021. 4(4): p. 291-301.
22. Dual, S.A.Z., B. L.; Sündermann, S.; Cesarovic, N.; Kron, M.; Magkoutas, K.; Hengsteler, J.; Falk, V.; Starck, C.; Meboldt, M.; Vörös, J.; Daners, M. S., Continuous Heart Volume Monitoring by Fully Implantable Soft Strain Sensor. *Advanced Healthcare Materials*, 2020. 9(2000855): p. 1-11.
23. Kear, M. and R.N. Smith, A method for recording tendon strain in sheep during locomotion. *Acta Orthop Scand*, 1975. 46(6): p. 896-905.
24. Biewener, A.A., Muscle-tendon stresses and elastic energy storage during locomotion in the horse. *Comp Biochem Physiol B Biochem Mol Biol*, 1998. 120(1): p. 73-87.
25. Lawson, S.E., et al., Effect of toe and heel elevation on calculated tendon strains in the horse and the influence of the proximal interphalangeal joint. *J Anat*, 2007. 210(5): p. 583-91.
26. Riemersma, D.J., et al., Tendon strain in the forelimbs as a function of gait and ground characteristics and *in vitro* limb loading in ponies. *Equine Veterinary Journal*, 1996. 28(2): p. 133-138.

Appendix

1. Supplementary of chapter 3

LCR Resonance Frequency

In a real system (Figure 1b), damping in the system lowers the actual frequency. The underdamped resonance frequency results in

$$f_d = f\sqrt{1 - \zeta^2} \quad (6)$$

With a damping factor of $\zeta = \frac{R}{2}\sqrt{C/L} = \frac{1}{2Q}$ and a quality factor of $Q = \frac{2\pi fL}{R} = \frac{1}{R}\sqrt{L/C}$. Insight into the formula is given when rearranged to

$$f_d = f\sqrt{1 - \frac{1}{4Q^2}} \quad (7)$$

For sensors with a reasonable high Q factor, we can assume $f_d \approx f$ as in the case of our system even at 50% strain of the capacitor.

In addition, the resonance frequency f_0 can be expressed in dependence of strain ϵ by combining Equation 1 and 2.

$$f = \frac{1}{2\pi\sqrt{L(1 + \epsilon)C_0}} \quad (8)$$

Rearranging Equation 8 results in

$$f^2 = \frac{1}{4\pi^2 L(1 + \epsilon)C_0} \rightarrow (1 + \epsilon) = \frac{1}{4\pi^2 f^2 LC_0}$$

With $f_0 = \frac{1}{2\pi\sqrt{LC_0}}$ this leads to

$$(1 + \epsilon) = \frac{f_0^2}{f^2} \rightarrow \sqrt{1 + \epsilon} = \frac{f_0}{f} \rightarrow f = \frac{f_0}{\sqrt{1 + \epsilon}}$$

The gauge factor can be defined as

$$GF = \frac{\Delta f / f_0}{\epsilon} = \frac{f_0 - f}{f_0 \epsilon} = \frac{f_0 - \frac{f_0}{\sqrt{1 + \epsilon}}}{f_0 \epsilon} = \frac{1 - \frac{1}{\sqrt{1 + \epsilon}}}{\epsilon} \quad (9)$$

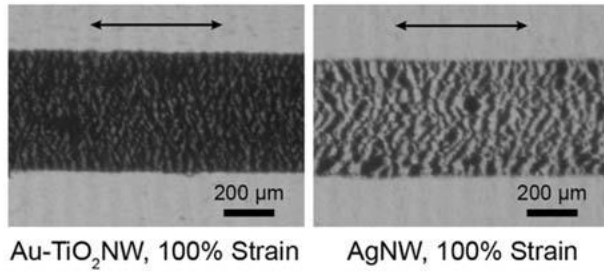


Figure S1. Bright field images showing the fracture formation at 100% strain for Au-TiO₂ NW-Dragonskin and AgNW-Dragonskin tracks.

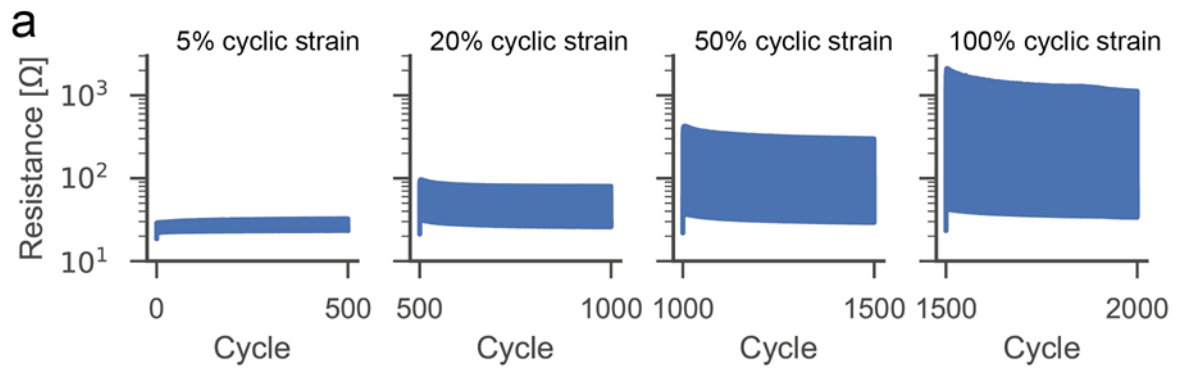


Figure S2. Electrical resistance measured during cyclic strain of an Au-TiO₂ NW-PDMS composite track with progressive increase in strain with 500 cycles each.

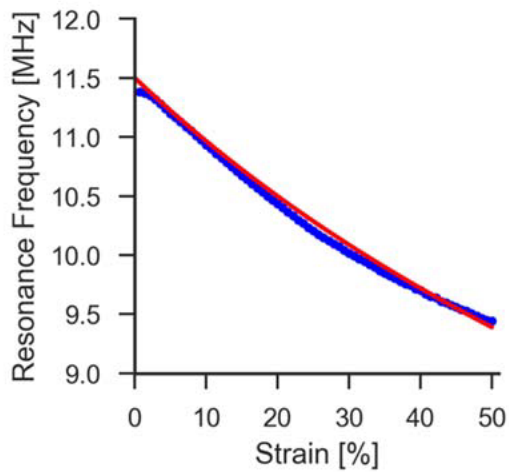


Figure S3. Resonance frequency over strain according to $f = f_0 / \sqrt{1 + \epsilon}$ (red) and measured with an actual sensor (blue).

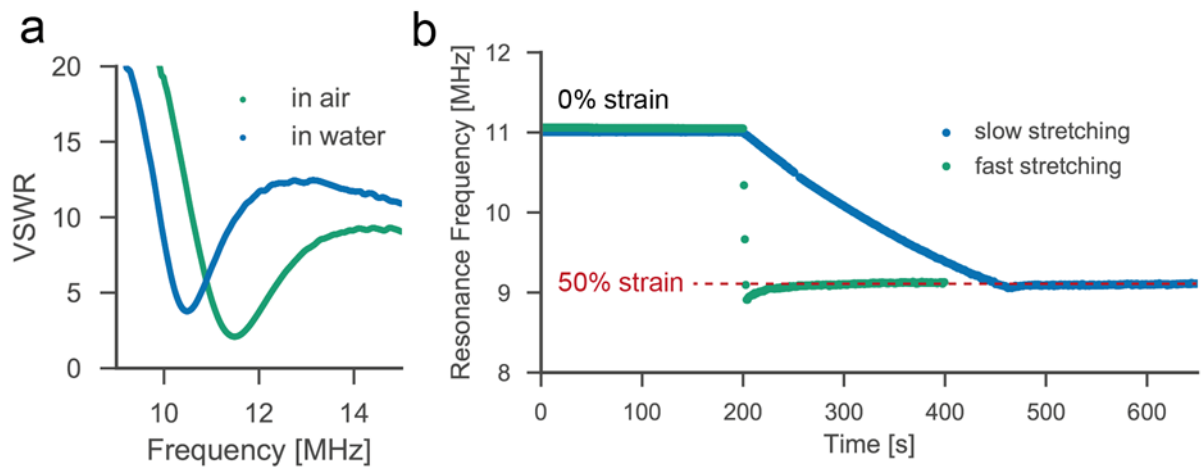


Figure S4. Additional characterization of the highly stretchable wireless strain sensor. a) Influence of the surrounding media on the resonance frequency of the sensor. Immersion of the sensor in water leads to a shift towards a lower frequency. b) Sensor stability over time at 0% strain and 50% strain for a sample stretched with 1 mm s^{-1} (fast stretching) and 0.01 mm s^{-1} (slow stretching).

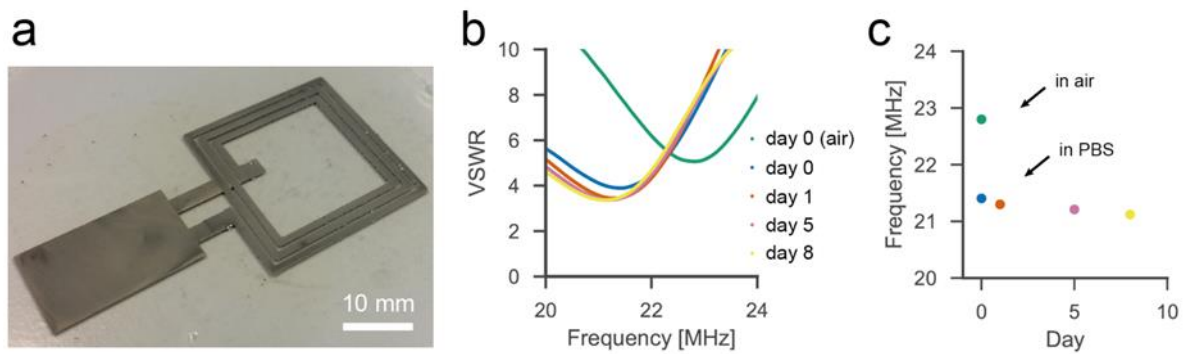


Figure S5. a) An LCR sensor made purely out of stretchable conductor with AgNW. b) The measured VSWR of this sensor over frequency in air and fully immersed in PBS (day 0-8). c) The measured resonance frequency in air and fully immersed in PBS during 8 day.

2. Supplementary of chapter 4

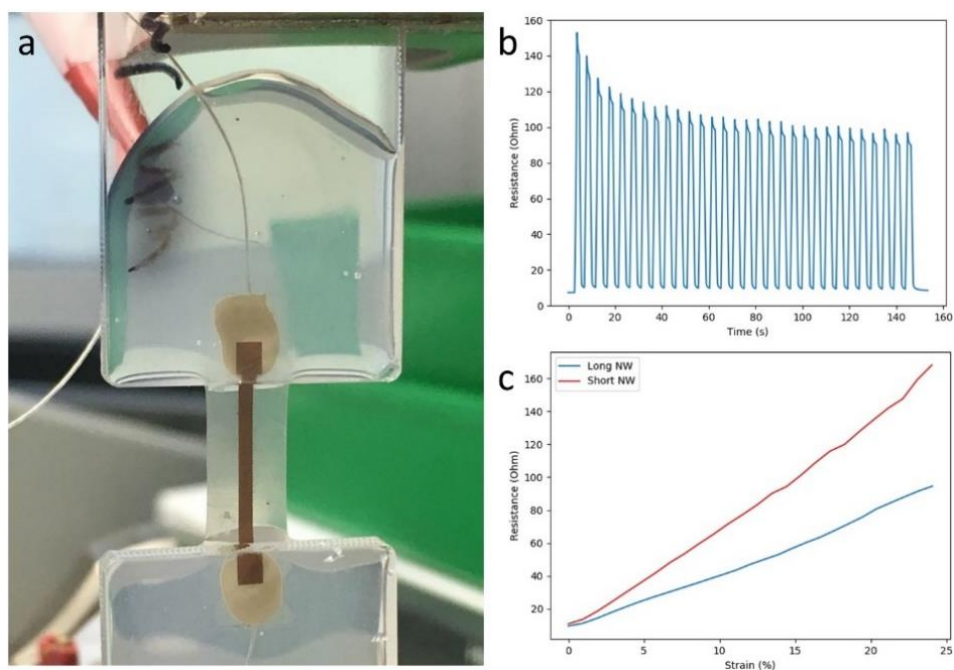


Figure S1. Conductivity of track with 10 nm and 5 nm Au-TiO₂ nanowires. a) Stretching test of nanowire track using a tensile testing machine. b) Resistance changes of 10 nm Au-TiO₂ nanowire track under 30 cycles of loadings. c) Smaller resistance increases of 10 nm Au-TiO₂ nanowire track compared to 5 nm Au-TiO₂ nanowire tracks.

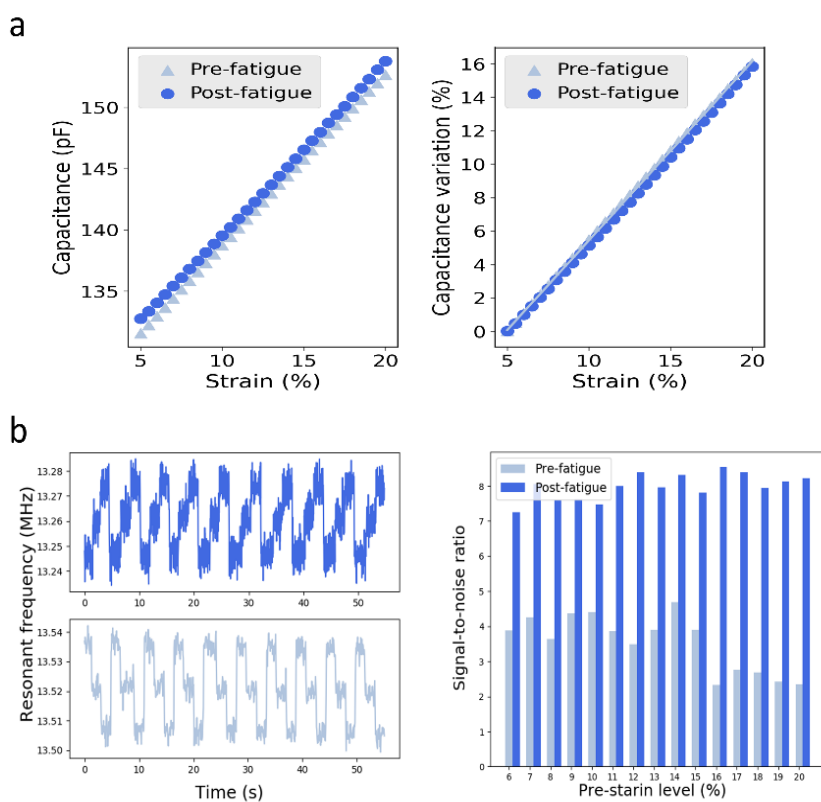
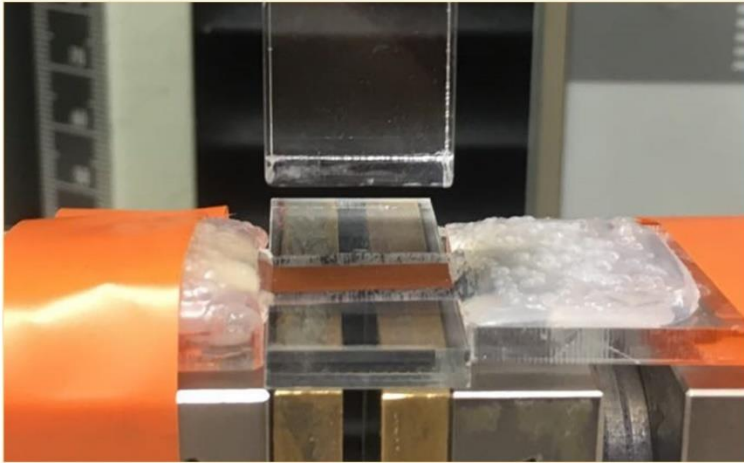


Figure S2. Characterization of stretchable capacitor. a) Absolute (left) and relative (right) capacitance changes of the stretchable capacitor against strains before and after fatigue test. b) Left: Capacitance changes of the stretchable capacitor. Right: Signal-to-noise ratio vs Pre-strain level (%).

in ± 0.1 % resolution measurements before and after fatigue test. Right: Signal to noise ratio in ± 0.1 % resolution measurements before and after fatigue test.



Pre-strains (%)	C (pF) at 0N pressure	C (pF) at 10N pressure	Relative change (%)
0	123.694	124.078	0.31
5	129.381	130.267	0.68
10	133.691	133.984	0.22

Figure S3. Capacitances (C) of the capacitor against pressures under different pre-strain levels.

3. LCR strain sensor reader

Adapted from the user manual of the LCR sensor reader written by Roman Gubler.

3.1. Measurement principle of the reader

The decayed signal of the stimulated LCR strain sensor is captured by the antenna of the reader. The signal gets amplified and digitized with a sampling frequency of 36 MHz. Then the stimulus 356 samples are acquired with an acquisition time of about 9.89 μ s. The measure interval of 1ms is provided by a dedicated timing module. The acquired datasets can be logged to a SD card in real time. The datasets can also be transmitted over USB to a PC or via Bluetooth to an IOS device with a frequency of 10 Hz for monitoring purposes. The datasets can be displayed in either time or frequency domain on the IOS device. The frequency domain of the signal is calculated on the reader itself using a customized window and FFT method. Furthermore, a simple averaging filter is applied on the reader. The range in frequency domain view is reduced to the most important range of 10 to 17 MHz.

3.2. Hardware

3.2.1. Hardware Overview



Figure 1. Hardware overview

1	Power switch
2	Master / Slave selector switch (takes effect only after reboot!)
3	Micro USB port for charging and data link
4	Micro SD slot
5	SMC RF-Connector for the antenna
6	Status LEDs

7	Protective Cap
8	Device ID

3.2.2. LED States

The following table shows what the different LEDs and their colours indicate.

LED	Colour	Meaning
Battery	Green	Charging
	Blinking (fast)	Battery Fault
	Blinking (slow)	Over or Under Temperature (charging interrupted)
System	Blinking	No Synchronisation to Master
	Green	Ready (Slave)
	Orange	Ready (Master)
	Blue	Measuring
	Magenta	Logging
	Red	System Fault
Bluetooth	Green	Ready
	Blue	Connected
	Red	Bluetooth Fault

3.3. Synchronisation

The reader (Fig. 1) can be configured as *Slave* or *Master* mode for synchronization purposes: 1) *Master* mode: to measure and log data. The reader sends a synchronisation packet over Bluetooth to nearby readers in *slave* mode; 2) *Slave* mode: to measure data. A reader in *slave* mode must be synchronized with a reader in *master* mode to log data. A measurement setup must include one reader in *master* mode and optional 0-13 readers in *slave* mode. When the “*master*” reader is turned on, an internal epoch counter starts counting with an interval of 1s. The epoch value is regularly broadcasted to the “*slave*” readers to synchronize the “*slave*” reader’s epoch counter. Once the logging is started, the epoch value is stored in the file name. It provides the measure on how many seconds the datasets in the files of the different readers differ in time. During operation the “*slave*” readers may lose the synchronisation with the “*master*” reader. If they do not receive a synchronisation packet from the “*master*” reader within 8 seconds, the logging process will be stopped.

3.4. Bluetooth/IOS Device

An IOS App is provided for controlling the readers and measurements. On the start page, the app lists all readers connected (Fig. 2, left). Each reader is displayed with an ID, a letter “M” or “S” indicating whether it is configured as *master* or *slave*, and a state. When a reader is selected, the connection will be established (Fig. 2, right).

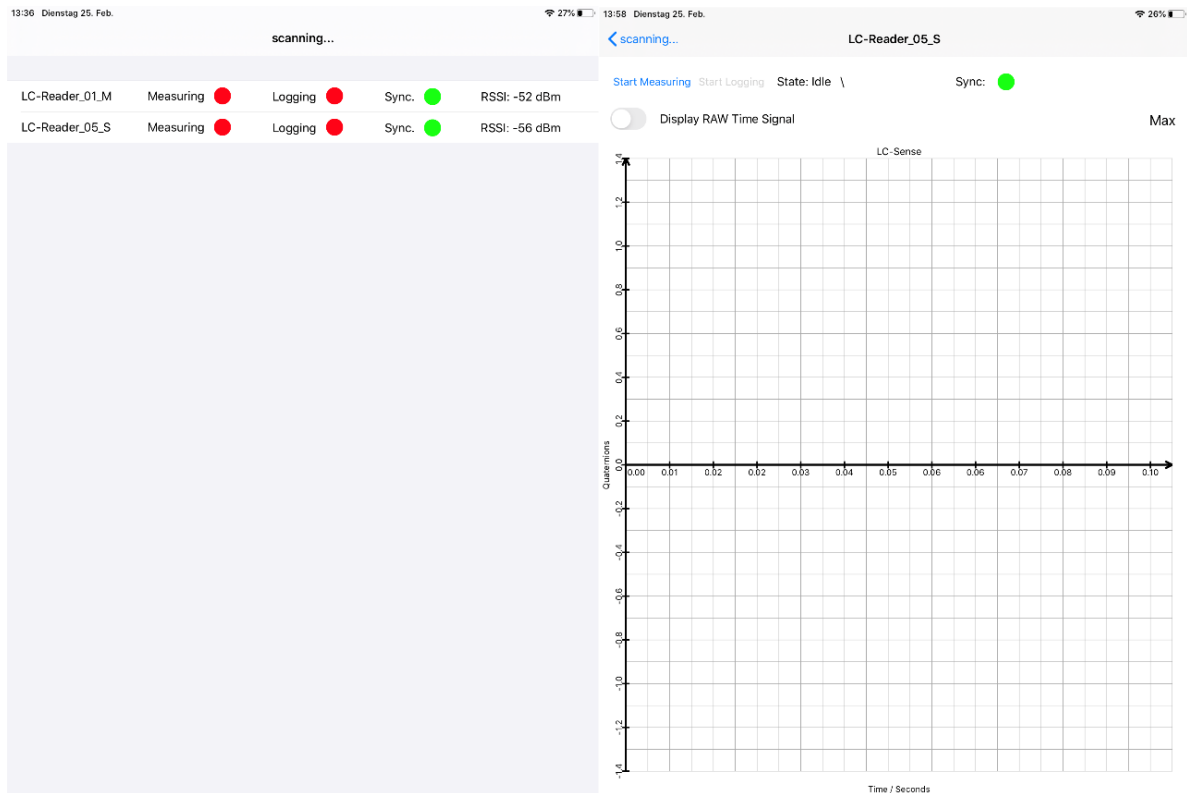


Figure 2. Start page (left) and connected page (right) of the IOS device.

- Clicking on the “Start measuring” button, the system begins to measure (Fig. 3).
- Double tapping on the screen, an auto scale function gets activated.
- Multi-touch gesture, the plot is rescaled.
- Press on the “Start logging” button, the data start to be logged to the SD-Card.

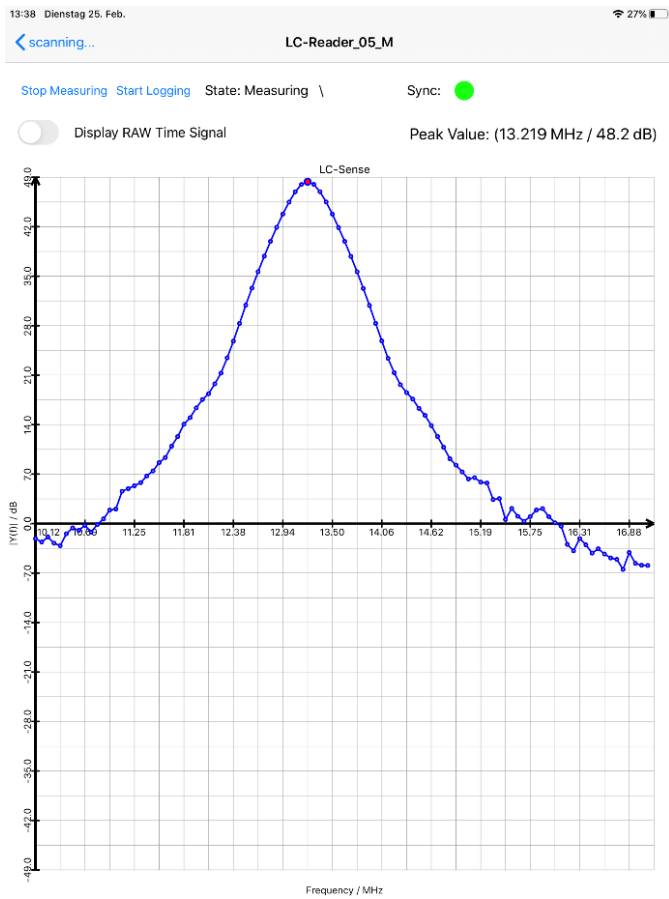


Figure 3. Measurement page of the IOS device.

4. Sync Box

Adapted from the factsheet of the sync box written by Roman Gubler.

4.1. Hardware overview



Figure 1. Hardware overview (front)

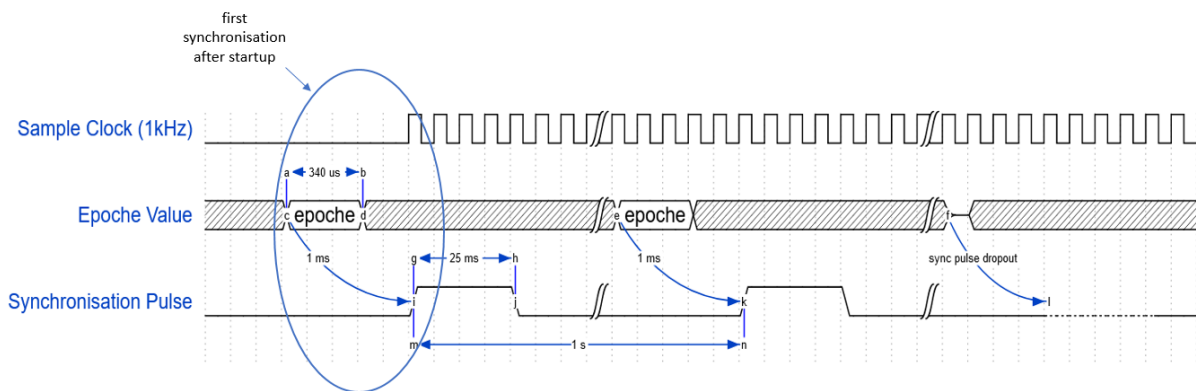
1	Power switch
2	Master / Slave selector switch (takes effect only after reboot!)
3	Micro USB port for charging and Epoche Data Output (ASCII Format, '\n' terminated)
4	Micro SD slot
5	Not Installed
6	Status LEDs
7	Protective Cap
8	Device ID



Figure 2. Hardware overview (back)

Socket	Type	Description
GND	-	Signal Ground
1PPS	OUT	Synchronisation Pulse: Present if the device receives a synchronisation packet over Bluetooth from a nearby master (usually 1 Puls-Per-Second but may dropout due to packet loss). Always present on master unit.
CLK	OUT	Sample Clock (1kHz): Always present after first synchronisation
A-IN	IN	Analog Input: The signal applied to this port is sampled with 1kHz and stored on the SD card.

Output Timing:



4.2. LED States

The following table shows what the different LEDs and their indications.

LED	Colour	Meaning
Battery	Green	Charging
	Blinking (fast)	Battery Fault
	Blinking (slow)	Over or Under Temperature (charging interrupted)
System	Blinking	No Synchronisation to Master
	Green	Ready (Slave)
	Orange	Ready (Master)
	Blue	Measuring
	Magenta	Logging
	Red	System Fault

Bluetooth	Green	Ready
	Blue	Connected
	Red	Bluetooth Fault

4.3. IOS APP

In the scanning view in Fig. 3, the Sync Boxes are listed under the name LC-Sync-{ID}-{Master/Slave}. If the Sync Box is in "measuring" or "logging" mode, the signal on the analogue input (A-IN) is displayed. The signal can be logged on the SD-card using the "Start Logging" Button.

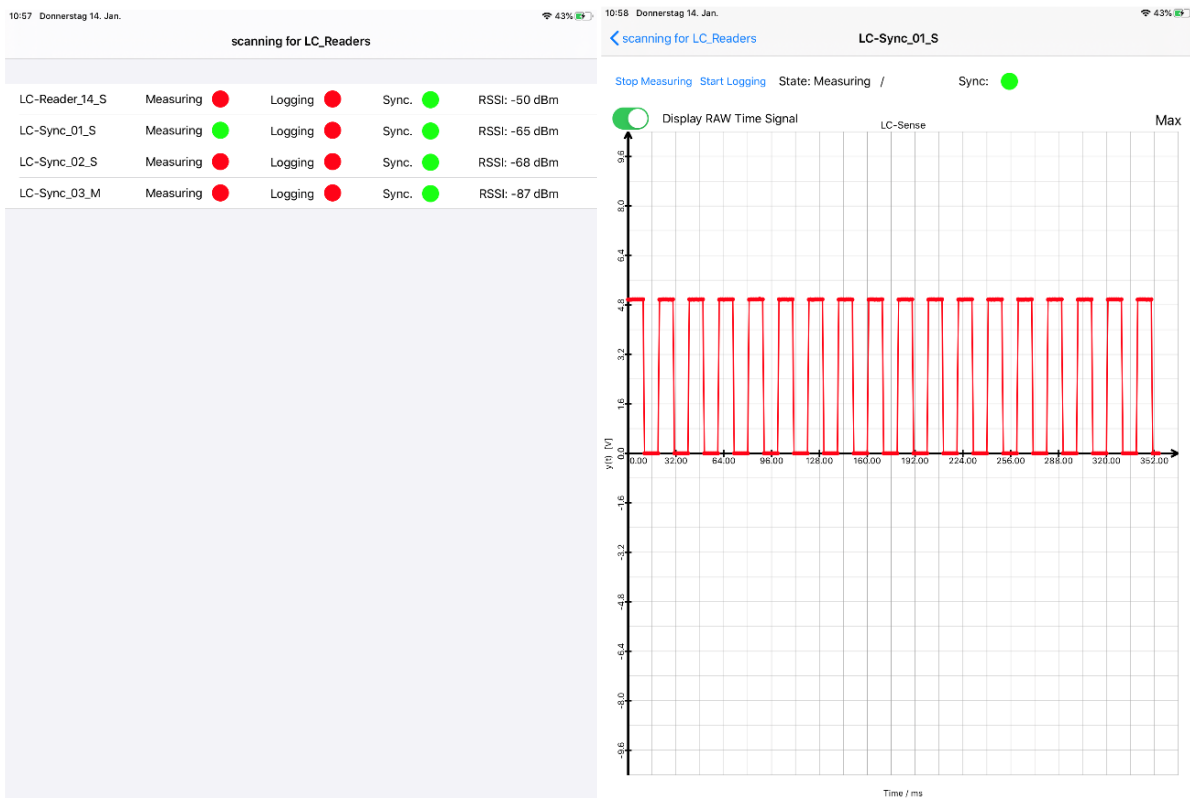


Figure 3. Start page of the IOS device (left); 5 V, 50 Hz square waves in the measurement page of a sync box (right).

Curriculum Vitae

Personal information

Name: Qiang Zhang

Date of Birth: July 1, 1988

Nationality: Chinese

OrcID: 0000-0002-2385-4442

Affiliation: Institute for Biomechanics, ETH Zürich.
Leopold-Ruzicka-Weg 4, 8093 Zürich, Switzerland

Contact: Email: qiang.zhang@hest.ethz.ch



Education

Nov. 2016 - February 2022: PhD candidate (Supervisor: Prof. Dr. William R. Taylor; Co-supervisor: Dr. Colin R. Smith), biomedical engineering, ETH Zürich, Switzerland

Sept. 2011 - June 2014: Masters, sports biomechanics, Shanghai University of Sport, China

Sept. 2007 - June 2011: Bachelors, biotechnology, Northeast Forestry University, China

Employment history including current position

Nov. 2016 – February 2022: Research assistant (PhD candidate), Laboratory for Movement Biomechanics, ETH Zürich, Switzerland

July 2014 - June 2016: Research assistant (100% FTE), Department of Orthopaedics, Xinhua Hospital Affiliated to Shanghai Jiao Tong University School of Medicine, China

Supervision of junior researchers

Nov. 2020 - Feb. 2021: Master's internship, Sarah Abramovic

Mar. 2019 - July 2019: Bachelor's internship, Vullnet Useini

Mar. 2018 - Nov. 2018: Master's thesis, Christian Huber

Active memberships in scientific societies, fellowships in renowned academies

Member, International Biomechanics Society

Member, Swiss Society of Biomedical Engineering

Member, European Society of Biomechanics

Member, Chinese Society of Sports Science

Prizes, awards, fellowships

July 2020 International travel award, International Society of Biomechanics.
Total funding CHF 2500

Apr. 2020 AO Research Opportunity Award, Switzerland. Total funding CHF
2000

Sept. 2016 National Scholarship of China, China. Total funding CHF 91'200

Feb. 2013 International Academic Exchange Scholarship of Shanghai University
of Sport, China. Total funding CHF 5500

Sept. 2012 Annual Scholarship of Shanghai University of Sport, China. Total
funding CHF 1000

Personal skills

Languages: Chinese (native), English (fluent)

Programing & statistics: Python, R, SPSS, GPower

Academic competences: Endnote, Origin

Other competences: VICON motion capture system, Visual 3D, EMG system, dynamometry

Knowledges: human biomechanics, musculoskeletal anatomy, statistical principles

Publication list

Q. Zhang, F. Bossuyt, N. Adam, et al., A Stretchable Strain Sensor System for Wireless Measurement of Musculoskeletal Soft Tissue Strains. *Adv. Mater. Technol.*, 2022. (In preparation)

X. Wu*, **Q. Zhang***, J. Qiao, N. Chen, X. Wu, A Calligraphy-based Rehabilitation Exercise for Improving the Upper-limb Function of Stroke Patients: Protocol for A Randomized Controlled Study. *BMJ Open*, 2021. (under review; *co-first author)

M. Ruan, **Q. Zhang**, X. Zhang, J. Hu, X. Wu, Differences in strength and landing biomechanics between female jumpers and swimmers. *Isokinet Exerc Sci*, 2021. Preprint: 1-11.

Q. Zhang, M. Ruan, N.B. Singh, L. Huang, X. Zhang, X. Wu, Progression of Fatigue Modifies Primary Contributors to Ground Reaction Forces during Drop Landing. *J Hum Kinet*, 2021. 76: 161-173.

Q. Zhang, N. C. Adam, S. H. Hosseini Nasab, W. R. Taylor and C. R. Smith. Techniques for *In Vivo* Measurement of Ligament and Tendon Strain: A Review. *Ann Biomed Eng*, 49: 7-28, 2021.

H. Christian*, **Q. Zhang***, W.R. Taylor, A.A. Amis, C. Smith, S.H.H Nasab, Properties and Function of the Medial Patellofemoral Ligament: A Systematic Review. *Am J Sport Med*, 2020. 48(3): 754-766. (*co-first author)

Stauffer, F., **Q. Zhang**, K. Tybrandt, et al., Soft Electronic Strain Sensor with Chipless Wireless Readout: Toward Real-Time Monitoring of Bladder Volume. *Adv Mater Technol*, 2018. 3(6).

MF. Ruan, **Q. Zhang**, X. Wu, Acute Effects of Static Stretching of Hamstring on Performance and Anterior Cruciate Ligament Injury Risk During Stop-Jump and Cutting Tasks in Female Athletes. *J Strength Cond Res*, 2017. 31(5): 1241-1250.

Q. Zhang, L.L. Shi, K.C. Ravella, K. Jason, SB. Wang, CL. Liu, GA. Li, JH. Wang, Distinct Proximal Humeral Geometry in Chinese Population and Clinical Relevance. *J Bone Joint Surg Am*, 2016. 98(24): 2071-2081.

Contributions to conferences

Q. Zhang, N. Adam, B. Llerena, K. Nuss, R. Küng, W.R. Taylor, C.R. Smith, Cadaveric Demonstration of a Novel Stretchable Sensor to Wirelessly Measure Musculoskeletal Soft Tissue Strains during Passive Limb Motion. The 28th Congress of the International Society of Biomechanics (ISB), Stockholm, 25.07-29.07.2021.

N. Adam, **Q. Zhang**, B. Llerena, R. Küng, W.R. Taylor, C.R. Smith, The Performance of a Novel Implantable Strain Sensor Under Replicated *In Vivo* Conditions. The 28th Congress of the International Society of Biomechanics (ISB), Stockholm, 25.07-29.07.2021.

F.M. Bossuyt, S. Han, **Q. Zhang**, C.R. Smith, W.R. Taylor, W. Herzog, The Use of A Wireless Passive Electronic Strain Sensor to Measure Hysteresis of Sheep Hindlimb Tendons: A First Step towards Directly Comparing *In Vitro* and *In Vivo* Tendon Properties. The 28th Congress of the International Society of Biomechanics (ISB), Stockholm, 25.07-29.07.2021.

Q. Zhang, B. Llerena, N. Adam, C.R. Smith, J. Vörös, R. Küng, W.R. Taylor, Evaluation of a Wireless Stretchable Sensor for Assessment of *in vivo* Musculoskeletal Soft Tissue Strains. The 27th Congress of the International Society of Biomechanics (ISB), Calgary, 31.07-04.08.2019.

Q. Zhang, F. Stauffer, B. Llerena, J. Vörös, W.R. Taylor, Validation of a Wireless Strain Sensor for Functional Assessment in Musculoskeletal Soft Tissues. 8th World Congress on Biomechanics (WSB), Dubin, 8-12.07.2018.

LM. Zou, X. Wu, **Q. Zhang**, Effect of Anticipation on Risk Factors for ACL Injury during Cutting Task. 21st European Congress of Physical & Rehabilitation Medicine (ECPRM), Vilnius, 1-6.05.2018.

Q. Zhang, F. Stauffer, W.R. Taylor, K. Tybrandt, R. Küng, J. Vörös, A Wireless Sensor for Measurement of Soft Tissue Strains *In Vivo*. Annual Meeting of the Swiss Society for Biomedical Engineering (SSBE), Winterthur, 30.08.2017.

References

Dr. William R. Taylor, Professor, group head

Laboratory of Movement Biomechanics, ETH Zürich, Switzerland

+41 44 633 05 95

bt@ethz.ch

Dr. Colin R. Smith, Group leader - Clinical Biomechanics

Laboratory of Movement Biomechanics, ETH Zürich, Switzerland

+41 44 633 61 95

colin.smith@hest.ethz.ch